Synthesis, Characterization and Application of Water-soluble Gold and Silver Nanoclusters

Submitted in partial fulfillment of the requirements for
the degree of
Doctor of Philosophy
in
Department of Chemistry
Mellon College of Science
by

Santosh Kumar

Carnegie Mellon University
Pittsburgh, PA

June, 2013.

Acknowledgements

I attribute my successful completion of a wonderful journey as a Graduate student to a number of people. The quantum of support offered by each individual whom I have come across is unfathomable.

I owe a lot to my academic advisor Prof. Rongchao Jin. He was more than willing to accept a scientific orphan, nurture my talent and give me unconditional freedom to work in an area of my choice. His excellent display of patience, motivation, knowledge, guidance and exuberance has played a pivotal role in my accomplishments. To sum it, Dr. Jin is an epitome of 'mentorship'.

I extend my sincere thanks to Dr. Linda Peteanu and Dr. Danith Ly. Their support and contribution towards my graduate studies, in their capacity as members of my dissertation committee, is highly appreciated.

I would like to acknowledge the inquisitiveness of Dr. Sanchari Chowdhury, Sourav Dey and Woong Young from the Peteanu group. I am also grateful to my collaborators, Dr. Das and Dr. Thedore Goodson from University of Michigan. The confluence of me and my collaborators has opened new vistas for the application of atomically precise nanoclusters.

Dr. Rea Freeland. I am at loss of words to describe the support she has provided me during my stay at Carnegie Mellon. I have to extend my special thanks to Valerie Bridge, Brenda Chambers, Timothy Sager, Patsey Haddock and Sara Wainer.

I am strongly enthused to emphasize the contributions of my lab members. Dr. Huifeng Qian and Dr. Gao Li, one of the finest chemists, have helped trained me on the instruments. My colleagues, Anna, Dr. Zheng, Anindita Das (Dia), Chenjie Zheng, Qiong and Yuxiang have enabled my quick acclimatization in the lab and providing an atmosphere conducive for my graduate studies.

My collaborations with the visiting scientists, Dr. Hidaya Kawasaki and Dr. Chanlin Yu deserve special mention and appreciation.

I am highly grateful to the innumerable people, who have contributed to my scientific journey. The great zeal displayed by Dr. Ajeet Kumar to help me gain a rudimentary understanding of nanoparticle synthesis deserves the highest commendation.

I have always cherished the company of my friends Manish, Sourav, Vishwanath, Aditya, Partha, Dr. Gaurav Rekhi, Saumya Saurabh, Bhushan Kode, Hussain Kagalwala, Matharishwan

Naganbabu and an endless list of people who have always heard and entertained me during times of distress.

I would like to thank my family members for their constant support and motivation throughout my academic journey. Finally and most importantly, I would like to thank Vidhi Mishra. Her excellent display of concern, support and affection has always motivated me and rendered me spell-bound.

Thank you all for having been with me in wonderful journey, which would culminate in my graduation for Carnegie Mellon.

Abstract

The term ‘nanotechnology’ has emerged as a buzzword since the last few decades. It has found widespread applications across disciplines, from medicine to energy. The synthesis of gold and silver nanoclusters has found much excitement, due to their novel material properties. Seminal work by various groups, including ours, has shown that the size of these clusters can be controlled with atomic precision. This control gives access to tuning the optical and electronic properties.

The majority of nanoclusters reported thus far are not water soluble, which limit their applications in biology that requires water-solubility. Going from organic to aqueous phase is by no means a simple task, as it is associated with many challenges. Their stability in the presence of oxygen, difficulty in characterization, and separation of pure nanoclusters are some of the major bottlenecks associated with the synthesis of water-soluble gold nanoclusters. Water-soluble gold nanoclusters hold great potential in biological labeling, bio-catalysis and nano-bioconjugates.

To overcome this problem, a new ligand with structural rigidity is needed. After considering various possibilities, we chose Captopril as a candidate ligand. In my thesis research, the synthesis of Au_{25} nanocluster capped with captopril has been reported. Captopril-protected Au_{25} nanocluster showed significantly higher thermal stability and enhanced chiroptical properties than the Glutathione-capped cluster, which confirms our initial rationale, that the ligand is critical in protecting the nanocluster. The optical absorption properties of these Au_{25} nanoclusters are studied and compared to the plasmonic nanoparticles.

The high thermal stability and solubility of Au_{25} cluster capped with Captopril motivated us to explore this ligand for the synthesis of other gold clusters. Captopril is a chiral molecule with two chiral centers. The chiral ligand can induce chirality to the overall cluster, even if the core is achiral. Therefore, to obtain Au_{38} clusters as an enantiomer, the ligand employed should be chiral. The enantioselective synthesis of Au_{38} capped with different chiral ligands has been reported and their chiroptical properties have been compared.

The synthesis of a series of water-soluble Au nanoclusters has motivated us to study the effect of capping ligands and the core-size on their steady-state and time-resolved fluorescence properties, since the photoluminescence properties are particularly important for bioimaging and biomedical

applications of nanoclusters. To gain fundamental insights into the origin of luminescence in nanoclusters, the effect of temperature on the fluorescence properties of these clusters has also been studied.

The different sized nanoclusters ranging from a few dozen atoms to hundreds of atoms form a bridge between discrete atoms and the plasmonic nanocrystals; the latter involves essentially collective electron excitation-a phenomenon well explained by classical physics as opposed to quantum physics. The central question is: at what size does this transition from quantum behavior to classical behavior occur? To unravel this, we have successfully synthesized a series of silver nanoclusters. The precise formula assignment and their structural determination are still ongoing. We have successfully demonstrated the application of these water-soluble Au nanoclusters in photodynamic therapy for the treatment of cancer. We have successfully demonstrated that Au nanocluster system can produce singlet oxygen without the presence of any organic photosensitizers. In a collaborative project with Dr. Peteanu's group, the quenching efficiency of organic dyes by these water soluble nanoclusters is studied in different systems.

Overall, this thesis outlines the successful synthesis of a family of water-soluble nanoclusters, their optical, chiroptical and fluorescence properties, as well as some applications of these nanoclusters.

Table of Contents

List of Figures

List of Tables

List of Schemes

LIST OF ABBREVIATIONS

BSA	-	Bovine serum albumin
Captopril	-	(*2S*)-1-[(*2S*)-2-methyl-3 -sulfanylpropanoyl] pyrrolidine-2-carboxylic acid
CD	-	circular dichroism
CH_2Cl_2	-	Dichloromethane
$Co_2(CO)_8$	-	Dicobalt octacarbonyl
CsOAc	-	Cesium acetate
CV	-	Cyclic voltammogram
DAD	-	Diode array detector
DFT	-	Density functional theory
ESI	-	Electrospray ionization
Exp	-	Exponential
fcc	-	Face-centered cubic
FWHM	-	Full width at half maximum
FW	-	Formula weight
GSH	-	Glutathione
$HAuCl_4$	-	Tetrachloroauric(III) acid

HPLC	-	High Pressure Liquid Chromatography
HRTEM	-	High resolution transmission electron microscopy
HSA	-	Human serum albumin
IR	-	Infra red
LDI	-	Laser desorption ionization
MALDI	-	Matrix-assisted laser desorption ionization
MeCN	-	Acetonitrile
MS	-	Mass spectrometry
$NaBH_4$	-	Sodium borohydride
NIR	-	Near Infra red
NMR	-	Nuclear magnetic resonance
PAGE	-	Polyacrylamide gel electrophoresis
PhC_2H_4SH	-	2-phenylethanethiol (PET)
PhSH	-	Phenyl thiol
p-MBA	-	*p*-mercaptobenzoic acid
QY	-	Quantum yield
SAM	-	Self-assembled monolayer
SDS	-	Sodium dodecyl sulfate
SEC	-	Size exclusion chromatography
SERS	-	Surface Enhanced Raman Spectroscopy
SPR	-	Surface plasmon resonance
SR	-	Thiolate
TCSPC	-	Time-Correlated Single Photon Counting
TEM	-	Transmission electron microscopy
TGA	-	Thermogravimetric analysis
THF	-	Tetrahydrofuran
TOAB	-	*n*-tetraoctylammonium bromide
TOF	-	Time-of-flight
UV	-	Ultra violet
XRD	-	X-ray diffraction

Chapter 1

Introduction

1.1 History of metal nanoparticles

The earliest use of metal nanoparticles dates back to the ancient history of Roman, Egyptian and Chinese civilizations, although nanoparticles were not identified then. Gold and silver nanoparticles, were used to stain glasses for cathedrals and other decorative purposes. The application though, was not just restricted to decoration. In ancient India, metal nanoparticles had been used in medicinal application to cure arthritis and had a high cosmetic value. Despite these common applications, their size range was unknown due to the unavailability of nanoscale imaging techniques. The most significant scientific experiment came forward in mid-19th century when Michael Faraday reported the synthesis of gold colloid by the reduction of gold salt with white phosphorus in a two-phase system.

Figure 1.1 (A) Stained glass in Roman Cathedral, (B) Lycurgus Cup Glass4th Century AD. (Source: http://www.britishmuseum.org)

Faraday believed that the particles of his colloid were of dimensions smaller than the wavelength of visible light.[1]The ruby red color of gold colloid stimulated much interest in scientific research. After half an century, Gustov Mie solved the Maxwell equation in 1908 and successfully modeled the optical spectra of gold colloid. This was the first study of interaction of light with nanoparticles (gold) and it explained the absorption and scattering properties of gold nanoparticles. The invention of transmission electron microscopy (TEM) by Knoll and Raska in

1931 was an important asset, as the size of the synthesized nanoparticles could be precisely measured. The pioneering work[2] of J. Turkevich on the synthesis and TEM imaging of gold nanoparticles was an intriguing work; the synthesis of gold nanoparticles was done by employing citrate ions and gold salt in aqueous solution. The citrate ions serve as both a reducing agent and the stabilizer for protecting the gold nanoparticles.[2] The synthesis produced gold nanoparticles of size 10-20 nm measured by TEM. This method was further modified by G. Frens and it has since become a common method utilized even now a days for preparing citrate-capped gold nanoparticles of > 10 nm diameter.[3,4] The early synthesis of some of the metal nanoparticles followed this approach of using some kind of stabilizer to prevent the nanoparticles from aggregation due to collisions in the solution state. The common stabilizers used are surfactants, amphiphilic polymers, ligands, and even solvent molecules if they can bind to nanoparticle surfaces.[5] An early example of producing magnetic nanoparticles for early recording purposes was proposed by Hess et. al. to prepare Co colloid of 10-100 nm. In this method, $Co_2(CO)_8$ was heated to a high temperature in the presence of dispersant polymer.[6] The generation of metal nanoparticles by thermal decomposition of metal-organic precursor in the presence of a stabilizer became a common approach for the synthesis of Fe, Co, Ni, and Cd metal nanoparticles.[7-9] Another approach to synthesize metal nanoparticles with better size control was achieved by using high concentrations of reducing agents like citrate or sodium borohydride. Schmid et al developed the synthesis of phosphine protected gold nanoparticles with a size of ~ 1.4 nm by using excess $NaBH_4$.[10]

A quite popular method reported for gold nanoparticle synthesis was the “Brust-Schriffin method” reported in 1994. This method was motivated by the thiol self- assembled- monolayer (SAM) on metal surfaces.[11-13] This was the first report of using thiol as a capping ligand for the synthesis of gold nanoparticles. The Brust method involves two steps where the first step involves the phase transfer of gold salt by using a phase transfer agent (surfactant) and subsequently the Au (I) thiolate polymer was reduced by $NaBH_4$ to form nanoparticles. The use of excess of reducing agent (typically 10 times the gold salt) helped in narrowing the size distribution. The strong interaction of thiol with the gold surface and the Van der Waals interactions make this nanoparticle system highly stable. The size of the nanoparticle can be effectively controlled by the ratio of precursor gold salt to alkanethiol. Due to their extraordinary stability, these thiol protected nanoparticles can be even isolated and stored in powder form and further re-dispersed

in any desired solvent. This was in strong contrast to the behavior of gold colloid in solution stabilized by charge stabilization.[14-16]

1.2 Plasmonic properties of metal nanoparticles

The interaction of light with metal involves Plasmon excitation. The collective oscillation of conduction electrons on the metal surface excited by the incident light at the metal-dielectric interface refers to surface plasmon resonance (SPR). The resonance is achieved when the frequency of the incident photon matches with the frequency of the oscillating conduction electrons against the attractive force of the positive nuclei as shown in figure 1.2.[17] For many metals such as Cd, Pb, Hg, and Sn, the plasma frequency lies in the UV region of the spectrum, so no color effect is observed.

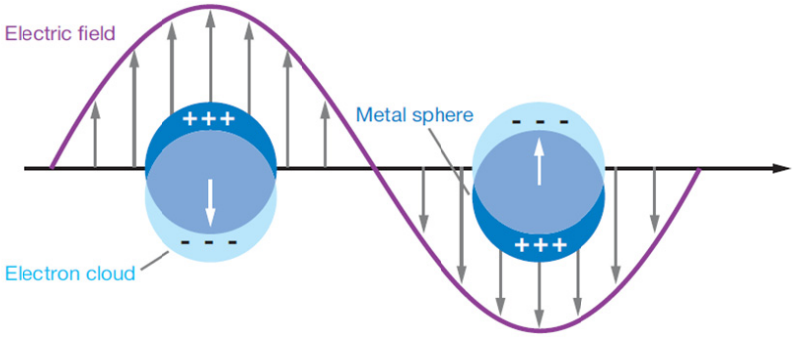

Figure 1.2 Schematic representation of surface plasmon for a metal sphere, showing the displacement of electron cloud relative to the nuclei. Reproduced from ref. 17 with permission. Copyright 2007 Annual Reviews.

For noble metals the plasma frequency lies in the visible region, so they show strong colors. Gold nanoparticles show a distinct surface plasmon band between 500-570 nm depending upon their size (i.e spherical particles). Similarly, silver shows the surface plasmon band between 430-460 nm. The size and shape of the gold and silver nanoparticles can be tailored to attain any color in visible spectrum as shown in figure 1.3 (a). As the size of these noble metal nanoparticles increases, the polarization of nanoparticles by the incident light is no longer homogeneous. As a result, the retardation effect of the electromagnetic field across the nanoparticle can cause plasmon broadening and huge shift in the peak wavelength as shown in figure 1.3 (b).[18] The SPR of gold or silver nanoparticles also depends upon the particle-particle interaction, the capping ligand around the nanoparticle, and also the dielectric medium of the

nanoparticle. The surface plasmon for gold nanoparticles is well defined for nanoparticles between 2-100 nm. The effect of increasing size has already been discussed, but if the size decreases below 2 nm the plasmon properties disappear and the quantum confinement starts playing important roles in the spectral properties. This effect will be explained in the later section.

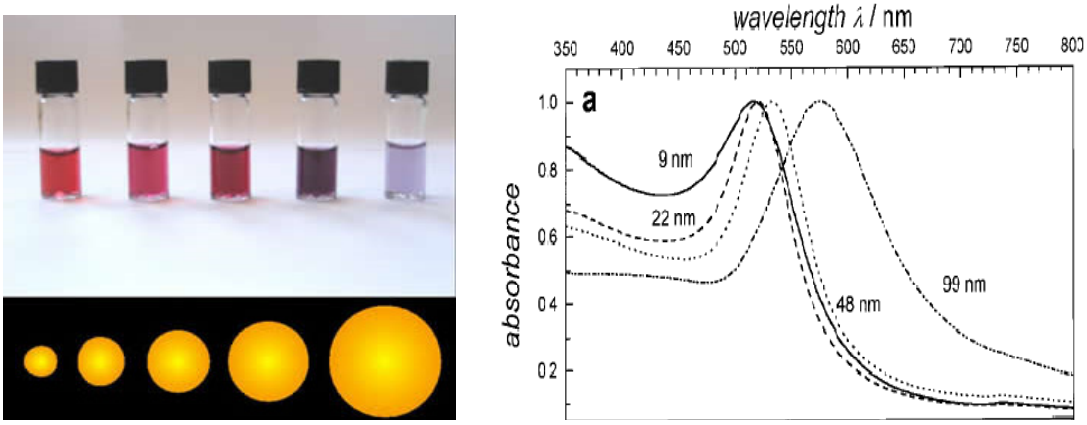

Figure 1.3 (a) Change in the color of nanoparticles solution with the core diameter. (Source: http://www.webexhibits.org/causesofcolor), **(b)** Surface plasmon peak shift and broadening with the change in the size of gold nanoparticle diameter. Reproduced from ref. 18 with permission. Copyright 1999 American Chemical Society.

1.3 Thiolate-protected gold nanoparticles

The synthesis of gold nanoparticles, which started as Au colloid by Faraday and further evolved into charge stabilized nanoparticle solution, was further explored by researchers and various synthesis of gold nanoparticles was reported in the solution state. As mentioned above, researchers explored the use of surfactants, polymers, phosphine and other various stabilizers to synthesize gold nanoparticles in solution. The thiol-protected Au nanoparticles prepared by the "Brust-Schiffrin method" are quite stable and can be conveniently stored in the powder form; post-synthetic manipulations such as functionalization and ligand exchange on such nanoparticle surfaces have been widely practiced.

Murray and co-workers employed various thiols such as straight chain alkanethiols (C_6, C_8, and C_{12}) to form gold nanoparticle with a core diameter of 1.2 nm and theoretical modeling suggested the nanoparticles to be of ~ 309 gold atoms and ~95 alkanethiols. Their work also showed that both solid and solution state characterization can be used for these nanoparticles as they can be

converted in powder form or dispersed in a solvent of choice.[19] In their successive work Murray et. al. used ω-substituted thiol to perform ligand exchange with the gold nanoparticles capped with unsubstituted thiol. The resultant gold nanoparticles were capped with the mixed monolayer of both the substituted and unsubstituted thiol.[20] Murray group also reported the synthesis of dodecanethiolate-protected Au nanoparticle with a mean diameter of 1.5-5.2 nm and studied the electronic properties of the gold core; they also employed different types of arenethiols for the synthesis of monolayer protected gold nanoparticles.[21,22]

The "Brust-Schiffrin method" was also adapted for the synthesis of water-soluble thiol protected gold nanoparticles. The use of thiol with hydrophilic substitution resulted in water solubility and surfactant molecules were used to stabilize gold nanoparticles.[23] Kornberg et al used various carboxylic acid substituted thiols to produce thiolated-gold nanoparticles with core diameter 1.5-4 nm.[24] The initial goal of these syntheses was to achieve narrow size distribution for the resultant nanoparticles. Several post-synthetic modifications were used to improve the size distribution of thiol- protected gold nanoparticles, such as, 1) non-solvent mediated size-selective precipitation,[25] 2) chromatographic separation,[26-28] 3) heat treatment.[29-31] The post-synthetic heat treatment was also termed "Digestive Ripening" in which the as-synthesized polydisperse-gold nanoparticles were further heated with excess thiol.[32] The other approach to achieving good control on the size distribution was developed by various groups, in which polymeric thioether, polymeric thiol, and mercapto-succinic acid were explored as capping ligands for the gold nanoparticle synthesis.[33-35]

1.4 Nanocrystals Vs Nanoclusters

The term nanocrystals' refers to the nanoparticles which are crystalline, while nanoparticles refer to entities that are not necessarily crystalline (e.g. polymer nanoparticles). On the other hand, nanoclusters are often reserved for the ultra small nanoparticles (e.g <2 nm). Whetten and co-workers achieved the synthesis of ultrasmall gold nanoparticles with a narrow size distribution;[25,36] specifically, Alvarez *et al* employed solvent based precipitation where a typical size can be selectively precipitated by using solvent with different polarity. They isolated Au nanocrystals in the size range of 1.5-3.5 nm which were estimated to have ~100 to ~1300 gold atoms. These isolated fractions were further analyzed by laser desorption ionization mass spectrometry (LDI-MS). These fractionated nanoparticles were readily forming superlattice,

which indicated there high monodispersity.[25,36,37] The LDI-MS revealed several critical sizes of Au nanocrystals, including 27-29 k, 45-46 k, 57 k, and 92-93 k species (k=1000 amu units).

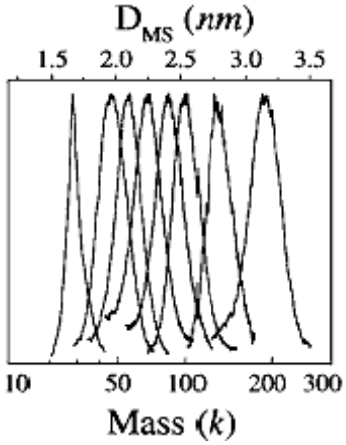

Figure 1.4 Different fractions of gold nanocrystals (3.2, 2.7, 2.5, 2.4, 2.2, 2.1, 2.0, and 1.7 nm, passivated by thiolate SC_6). Reproduced from ref. 34 with permission. Copyright 1997 American Chemical Society.

Figure 1.4 shows the eight isolated fractions of gold nanocrystals with their core diameters and masses determined by LDI-MS. The 92 k species was further studied by HR-TEM and found to be fcc lattice arrangement. Theoretical calculations suggested the optimum size of the Au core to be Au_{459} (92 k, 2.5 nm), Au_{314} (57 k, 2.1 nm), Au_{225} (45 k, 2 nm), and Au_{140} (28 k, 1.7 nm) species.[38] Murray et al also reported the Au nanocrystals with the core diameter of ~ 1.5 nm and estimated it to be ~ Au_{400}.[19] In all these cases even if the reported size was less than 2 nm, the nanoparticles still showed surface plasmon resonance. This was because of the purity of the isolated nanoparticles. The high molar absorptivity coefficient of plasmonic nanoparticle will dominate the spectral feature of smaller nanoparticles. So the intriguing question is how the spectral properties of nanoparticle changes, when their size is smaller than 2 nm? In section 1.2 the SPR for nanoparticles > 2nm was explained and it was mentioned that as the size of the nanoparticle system decreases below 2 nm the quantum confinement of electrons in the particle governs the spectral properties. When the size of nanoparticles is below 2 nm, the metal core only possesses has a countable number of atoms (up to ~200) and such ultrasmall particles behave as clusters of atoms or like molecules. The properties of such clusters are different than the bulk metal, and also different than their larger counterparts (i.e. conventional nanoparticles). Some of the clusters are also called superatoms as they show some of the properties like atoms. It

would be interesting to know at what size (i.e. precise number of atoms) the gold nanoparticles starts showing quantum confinement.

By using the free electron model one can estimate the quantum size regime. As the size of the particle becomes smaller, the average spacing (δ) of the electronic energy levels becomes considerable and δ increases with decreasing size. The average spacing (δ) can be roughly expressed as

$$\delta \approx \frac{E_f}{N}$$

where E_f refers to the Fermi energy and N is the number of metal atoms, since N can be expressed as $\propto d^3$ (d is the nanoparticle diameter). So the spacing is inversely proportional to the cube of particle diameter. If one uses the room temperature thermal energy (k_BT) as a criterion for considering quantum confinement, then one has the following relation,

$$\delta = k_BT$$

after substituting the value of Fermi energy for gold, E_f = 5.5 eV into the equation we can get the critical number of gold atom to be ~220 atom. The number of gold atom and the particle volume are related as

$$N = (59\ \text{nm}^{-3}).V$$

This gives the value of equivalent diameter to be ~2 nm. Thus, for gold nanoparticles below 2 nm the electronic energy quantization will dominate and the collective plasmon mode will no longer be supported. To differentiate such ultrasmall particles from conventional plasmonic nanoparticles, they are often called nanoclusters.

1.5 $Au_n(SR)_m$ nanoclusters

1.5.1 Initial synthesis of nanoclusters

The initial synthesis reported by Whetten and Murray were able to produce nanoparticle of size ~ 2 nm. Whetten and coworkers modified the synthesis by considering the Au:SR ratio to 1:3 and by varying the thiol linker length (C_4, C_6, C_{12}, and C_{18}) to obtain nanoclusters which would have size smaller than 2 nm. Several different sizes, 8 k (1.1 nm ~38 atoms), 14 k (1.3 nm ~75 atoms), 22-23 k (1.5 nm ~101 aoms), and 28-29 k (1.7 nm ~146 atoms) were successfully isolated and analyzed by LDI-MS as shown in figure 1.5 (a).[39] Powder X-ray diffraction patterns were obtained and theoretical calculations were carried out to model and determine the structural

information of these nanoclusters which proposed decahedra structures for the 14 k, and 22 k species as shown in figure 1.5 (b).[38] The optical absorption spectrum for 8 k species showed a step like appearance.

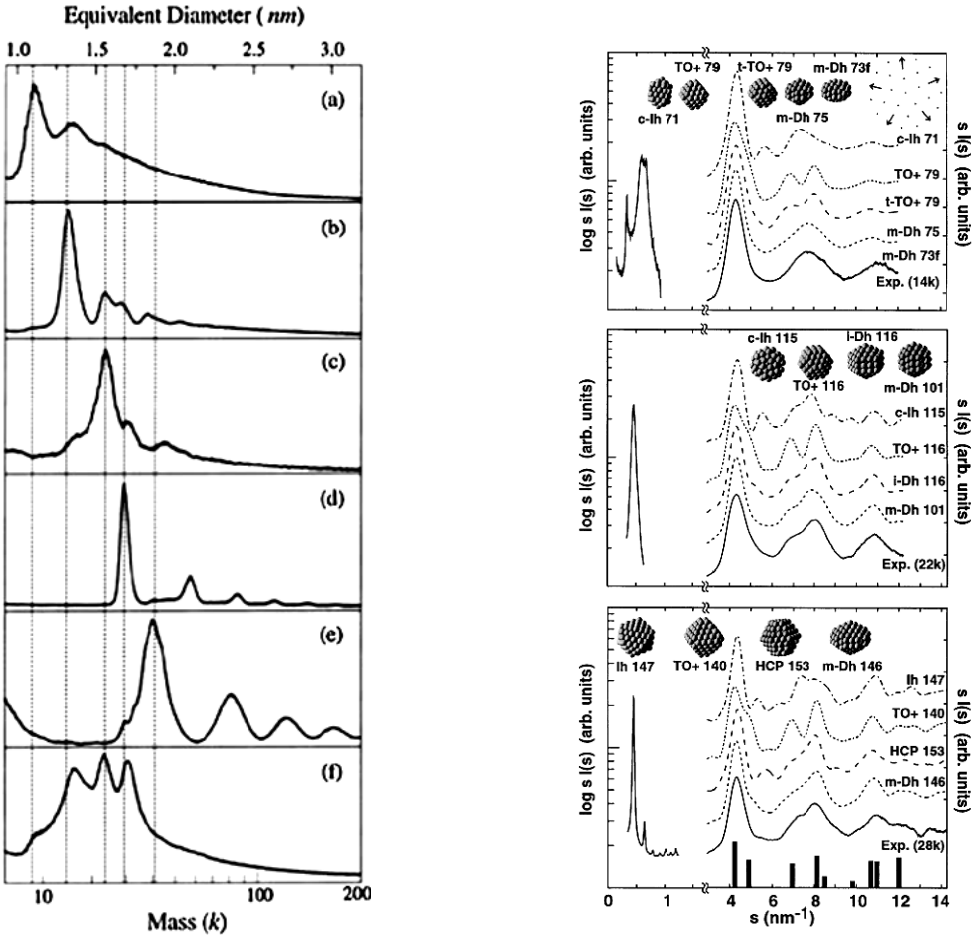

Figure 1.5 (a) LDI-MS of the size separated clusters. Reproduced from reference 39 with permission. Copyright 1997 American Chemical Society, **(b)** Experimental and calculated p-XRD intensities plotted against s (nm^{-1}). Reproduced from reference 38 with permission. Copyright 1997 American Physical Society.

This was the first time that gold nanoclusters with distinct spectra than plasmonic absorption was shown.[39] The nanoclusters reported by Whetten and coworkers were hydrophobic in nature as the capping ligand was alkanethiol or arylthiol which overall governed the solubility of nanoclusters. The mass assignment of the nanoclusters was made based on their LDI-MS analysis. LDI is a very harsh technique, as the laser tends to fragment the cluster. This means that

Au-S, S-C, or Au-Au bond can even be cleaved due to the high laser intensity. This will reduce the chance of getting the exact mass of the cluster, so the precise formula of a nanoclusters cannot be determined with accuracy. On the other hand, ESI-MS is a much softer ionization technique than LDI-MS, but in those days ESI-MS was restricted to water-soluble samples only. It is important to note here that ESI-MS can now be done for nanoclusters in both aqueous and organic solvents, but years ago the restriction of ESI-MS for only aqueous soluble samples prompted researchers to explore water-soluble thiol ligands. Schaff *et al* employed a tripeptide glutathione (GSH=γ-Glu-Cys-Gly) as a water-soluble thiol. Glutathione has a cystine unit in the middle which has a thiol group; this thiol group can be used to bind with gold. Glutathione is a very important biologically molecule as it is present in every living organism, as it maintains cellular potential in the reduced state. The use of glutathione was also advantageous, as its steric bulkiness provides a large cone angle and hence helps in controlling the cluster size. Schaff *et al* synthesized gold nanoclusters using GSH as a ligand and its water-solubility provided an opportunity to purify the cluster by running it through polyacrylamide gel electrophoresis (PAGE). The PAGE purification enabled the isolation of intact clusters and the ESI-MS analysis revealed the mass of the cluster to be 10.4 kDa as shown in figure 1.6 (a).[40] Based on the mass, the formula assigned to the cluster was $Au_{28}(SG)_{16}$ (later corrected as $Au_{25}(SG)_{18}$ by Tsukuda group via high resolution ESI-MS determination of the precise mass of the cluster). The absorption spectrum of this cluster showed multiple absorption bands which were manifestations of the quantum confinement for this cluster as shown in figure 1.6 (b).[40] Murray and coworkers used phenylethanethiol, and hexane thiol ligands and synthesize a cluster species that showed a similar optical spectrum as the $Au_{28}(SG)_{16}$ (corrected as $Au_{25}(SG)_{18}$ later).[41,42] Unfortunately the cluster formula was erroneously assigned to $Au_{38}(PhCH_2CH_2)_{24}$, later they corrected the formula as $Au_{25}(SCH_2CH_2Ph)_{18}$.

Similarly several other groups reported the synthesis of molecular sized clusters but the mass assignment and the formula identification was mistaken.[43,44]

Tsukuda and coworkers used the glutathione ligand and performed a one-phase synthesis to obtain a series of water-soluble clusters. These species were isolated by running it through PAGE. The high resolution ESI mass spectrometry data revealed and identified six different species, 1= $Au_{18}(SG)_{11}$, 2 = $Au_{21}(SG)_{12}$, 3 = $Au_{25\pm1}(SG)_{14\pm1}$, 4 = $Au_{28}(SG)_{16}$, 5 = $Au_{32}(SG)_{18}$, 6 = $Au_{39}(SG)_{23}$.[45] In their follow up work, the use of high density gel and the use of their own

modified ESI mass spectrometry enabled them to isolate and correctly identify 9 distinct species as shown in figure 1.7 (a) and (b).[46]

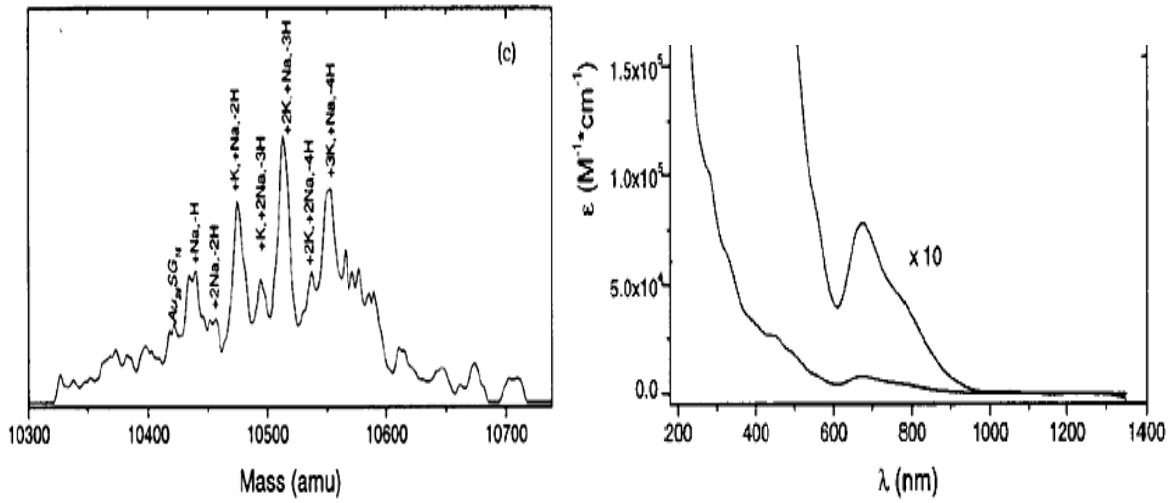

Figure 1.6 (a) Deconvulated ESI-MS spectra of the cluster, the satellite peak around the main peak are sodium and potassium adduct, **(b)** Absorption spectra of the gel isolated cluster. Reproduced from ref. 40 with permission. Copyright 1988 American Chemical Society.

In the ESI-MS work by Tsukuda *et al* the cluster fragmentation was largely suppressed, hence the molecular ion peaks for all the clusters were reliably observed and the formulas were finally assigned unequivocally. The nine clusters identified were $Au_{10}(SG)_{10}$, $Au_{15}(SG)_{13}$, $Au_{18}(SG)_{14}$, $Au_{22}(SG)_{16}$, $Au_{22}(SG)_{17}$, $Au_{25}(SG)_{18}$, $Au_{29}(SG)_{20}$, $Au_{33}(SG)_{22}$, and $Au_{39}(SG)_{24}$.[46] This was the first time that the detail formula assignment was completed for $Au_{25}(SG)_{18}$ and its standard spectrum was reported. The study of these clusters also revealed that $Au_{25}(SG)_{18}$ has superior stability compared to all other clusters in the reported series.[47]

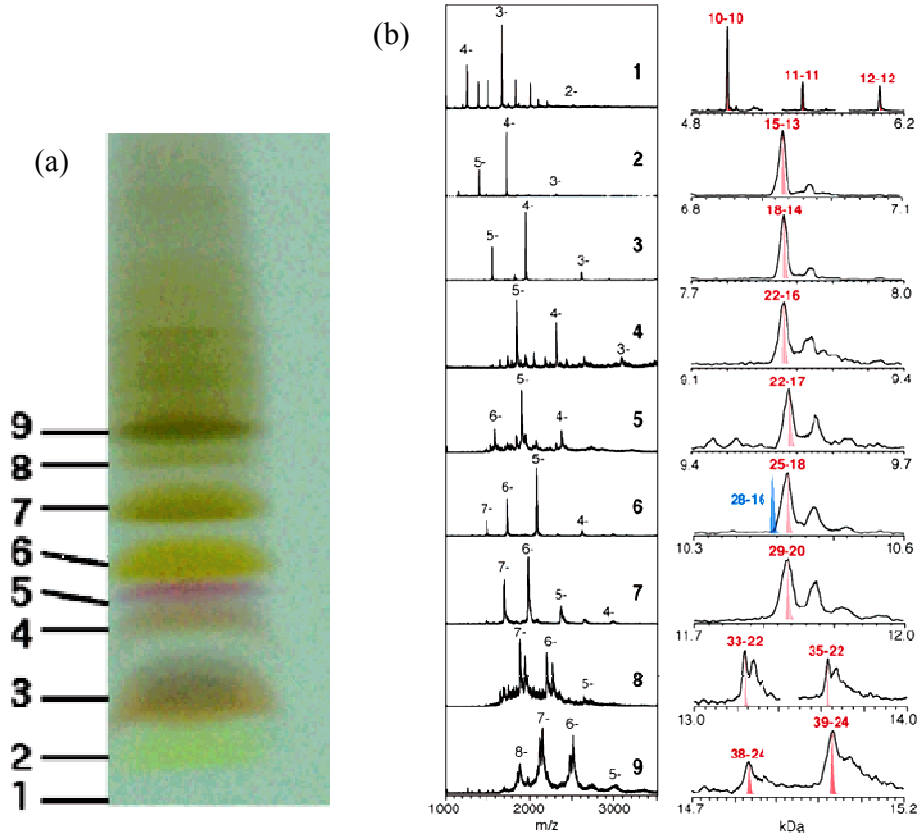

Figure 1.7 (a) PAGE image of the 9 distinct species with lowest mass cluster shown in the bottom, **(b)** high resolution ESI mass spectra of the gel separated cluster. Right panel shows the deconvulated mass spectra. Reproduced from ref. 46 with permission. Copyright 2005 American Chemical Society.

1.5.2 Synthesis of atomically precise $Au_n(SR)_m$ nanoclusters

The work by Tsukuda and coworkers was an important milestone in the synthesis of atomically precise nanoclusters, i.e. the clusters should have a certain number of metal atoms and ligands. Jin group started working on the nanoclusters and several important contributions have been made in last 4-few years. Zhu *et al* developed a kinetically controlled synthesis of Au_{25} clusters capped with phenyl ethanethiol in high yield.[48] The kinetic control of the Au(I) intermediate species allowed the exclusive formation of high purity Au_{25} clusters. The high purity of the synthesized clusters allowed the growth of single crystals (vide infra). By a similar synthetic modification and using a lower concentration of the reducing agent and slow reduction of Au(I) intermediate, Zhu *et al* obtained Au_{20} clusters capped with phenyl ethanethiol.[49] The large band

gap of 2.15 eV was observed for this cluster which was significantly higher than that of Au_{25} nanocluster (gap energy: 1.3 eV). Also the stability of the Au_{20} was significantly higher against thiol etching. Qian *et al* reported a large-scale synthesis of Au_{38} nanoclusters capped by dodecanthiol. The synthesis was carried in two steps, where the first step involves the synthesis of a polydisperse mixture, $Au_n(SR)_m$. This mixture was then etched with excess ligand to obtain molecularly pure $Au_{38}(SC_{12}H_{25})_{24}$ nanoclusters.[50] In a similar synthetic modification Qian *et al* reported the synthesis of $Au_{144}(SCH_2CH_2Ph)_{60}$. In these syntheses, the starting polydisperse mixture was used as a precursor for the second step where "size focusing" occurred, which gave rise to molecularly pure nanoclusters. The "size focusing" method involves the etching of the polydisperse mixture in the presence of excess thiol and is primarily driven by the thermodynamics, which eventually "focuses" the cluster size towards a stable cluster size.[51] Qian *et al* also reported the synthesis of Au_{40} and Au_{55} clusters.[52,53] The thiol etching mechanism was further extended to other ligands. Researchers have also demonstrated that phosphine protected gold clusters can be utilized in making thiolate-protected gold clusters. Murray and coworkers used phosphine protected Au_{55} nanoclusters to generate Au_{75} nanoclusters capped with hexanethiol.[54] Tsukuda and coworkers utilized phoshine-capped Au_{11} to make thiolate-capped Au_{25} clusters as well as phoshpine/thiolate rod-shaped Au_{25} clusters. Qian *et al* synthesized the Au_{25} nanospheres and Au_{25} nanorods by thiol etching of polydisperse Au nanoparticles capped with phosphine. The synthesis was done by both one-phase and two-phase approaches and this work demonstrated that the shape of Au_{25} nanoclusters can be conveniently controlled by the judicious choice of the ligand in the thiol-etching step using the regular nanoparticles as the precusor.[55]

1.5.3 Crystal structure determination of $Au_n(SR)_m$ clusters

The crystal structure of nanoclusters reveals the nature of bonding and the packing of atoms. The synthesis and formula determination does explain the identity of the synthesized nanoclusters, but the atomic packing, the nature of bonding between metal atoms and the ligand, and the electronic properties of clusters cannot be understood without knowing the structure. Bulk gold has a fcc structure, so do conventional gold nanocrystals; but what would happen as we go further down in the size regime was an interesting question. If the structures of the nanoclusters are not fcc then what other structures would be adopted in such clusters?

The first breakthrough was achieved by Korenberg and coworkers when they reported the synthesis and total structure determination of Au_{102} nanoclusters capped with 44 *p*-mercaptobenzoic acid.[56] The Au_{102} structure can be viewed as a Au_{79} core with D_{5h} symmetry. The rest 10 gold atoms cap the 10 square shaped Au facets of the Au_{79} core with a pseudo D_{5h} symmetry, which form a protecting layer. The remaining 13 gold atoms are connected with multiple bonds from the Au_{79} core atoms. The thiols in the crystal structure were shown to be bonded with both gold atoms. This gives a rigid surface layer to the crystal structure as shown in figure 1.8.[56] The structure showed that Au_{102} is chiral with both enantiomers present in the unit cell, hence, making the arrangement as a racemic mixtutre.

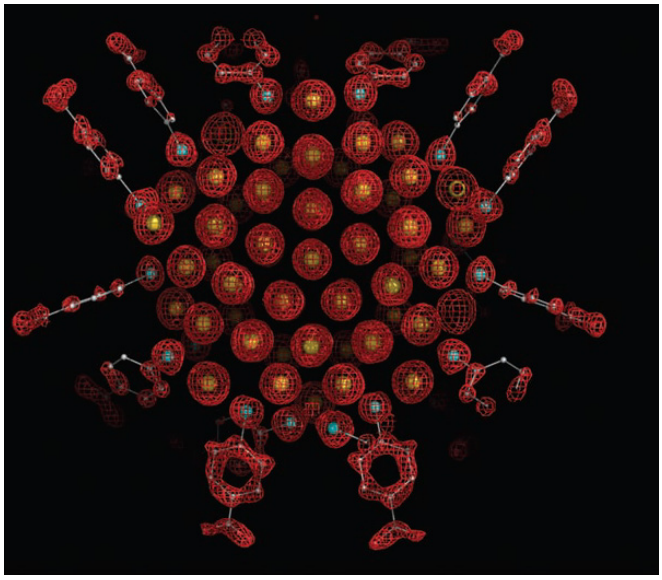

Figure 1.8 X-ray crystal structure of Au102(p-MBA)44 with Au atoms shown in yellow and S shown in Cyan. Reproduced with permission from ref. 56. Copyright 2007 AAAS.

The second successful report of crystal structure determination was independently reported by Murray and Jin groups for the $[Au_{25}(SCH_2CH_2Ph)_{18}]$ cluster (counterion: TOA^+).[57,58] In the work by Zhu *et al*, the high purity of the synthesized clusters via the approach of kinetic control was the key to successfully obtain the crystal structure. Murray and coworkers also successfully obtained the crystal structure of $[Au_{25}(SCH_2CH_2Ph)_{18}]^{-1}$ at the same time by using PhSH in the crystal growth solution.[58] In Zhu's crystallization method, the crystal was grown directly from the solution phase. The X-ray crystallographic analysis of Au_{25} revealed the presence of a Au_{13} icosahedron core with 12 remaining gold atoms arranged along the ±x, y, and z axes of the core.

As icosahedron has 20 triangular faces, so this leaves eight Au_3 triangular face uncapped. The 18 thiolate ligands cover the Au_{13} icosahedral core by six Au_2S_3 staple motifs as shown in figure 1.9 (a). Zhu *et al* also determined the crystal structure of charge-neutral $[Au_{25}(SCH_2CH_2Ph)_{18}]^0$ which was obtained by the loss of one electron from the anion through air oxidation shown in figure 1.9 (b).[59] Although the structural arrangement for both the anion and the neutral Au_{25} are the same, the anionic $Au_{25}S_{18}$ system showed distortions in the crystal structure while no such distortions was observed for Au_{25}^0.

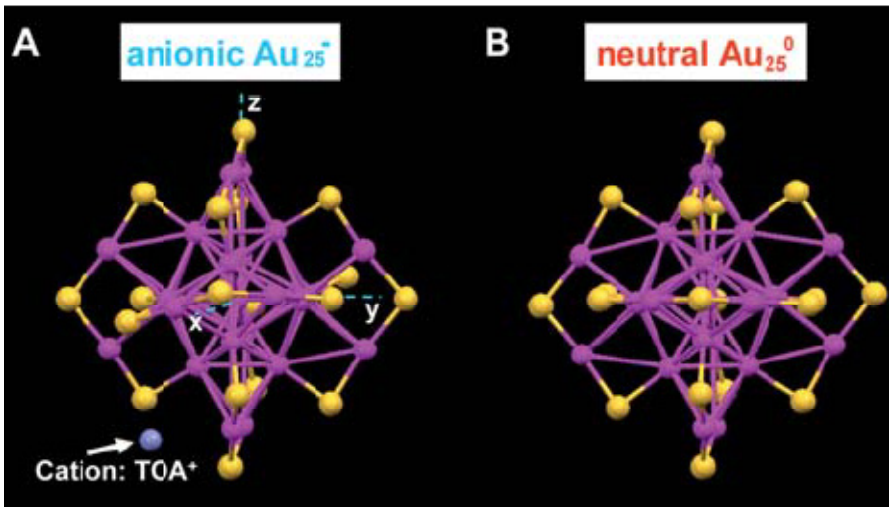

Figure 1.9 (a) Crustal structure of $[Au_{25}(SCH_2CH_2Ph)_{18}]^{-1}$, and **(b)** Crystal structure of $[Au_{25}(SCH_2CH_2Ph)_{18}]^0$. Reproduced with permission from ref. 59. Copyright 2009 American Chemical Society.

The initial work by Qian *et al* on the large scale synthesis of $Au_{38}(SC_{12}H_{25})_{24}$ clusters with high purity prompted the subsequent synthesis of $Au_{38}(SC_2H_4Ph)_{24}$. The latter was successfully grown into single crystals, followed by the determination of the crystal structure of $Au_{38}(SR)_{24}$. The high purity of the clusters and judicious design of crystallization conditions were the key for successful crystallization.[60]

The crystal structure of $Au_{38}(SCH_2CH_2Ph)_{24}$ also showed chiral structures (both enantiomers present in the unit cell, figure 1.9(a)). The crystal structure showed face-fused bi-icosahedral Au_{23} core capped by second shell of 15 Au atoms (shown in figure 1.9 (b)). If one accounts for the thiol ligands in the structure, then it can be visualized as Au_{23} core capped with three

monomeric staple motifs of the $Au(SR)_2$ form and six dimeric staple motifs of the $Au_2(SR)_3$ form.[60]

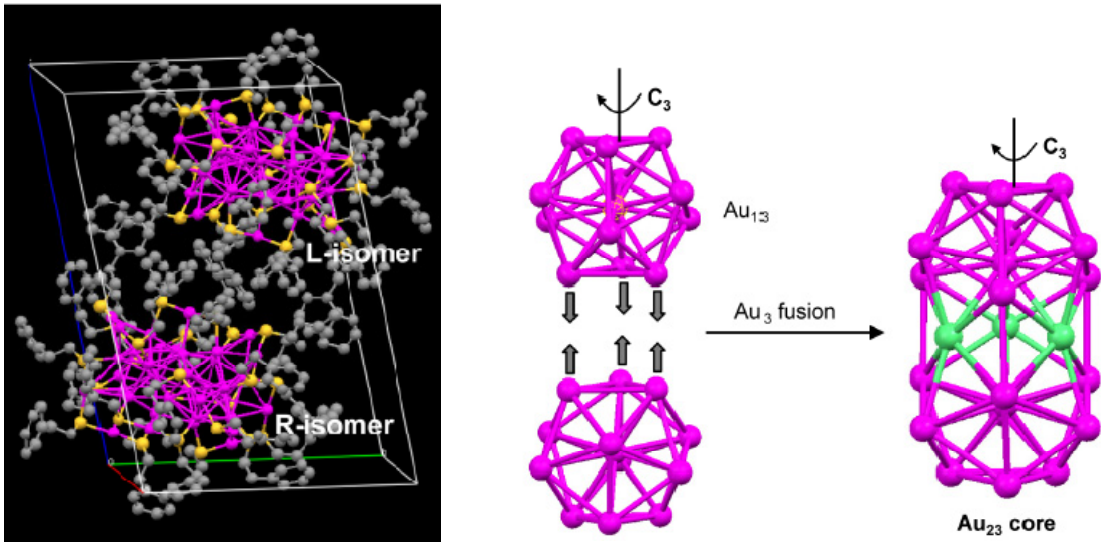

Figure 1.10 (a) Crystal structure of $Au_{38}(SCH_2CH_2Ph)_{24}$ showing the enantiomers in the same unit cell, with Au atoms on magenta, S in yellow, and C in grey, **(b)** Anatomy of the Au_{23} core arrangement in the Au_{38} structure. Reproduced with permission from ref. 60. Copyright 2010 American Chemical Society.

1.6 Synthesis of Au nanoclusters with other ligands

The synthesis, characterization and structural determination of several reported Au nanoclusters discussed in the previous sections delivered a great deal of information to the researchers; about the structure and bonding, optical and electronic properties and also about the stability of these nanoclusters. This also directs the research of noble metal nanoclusters towards various biological applications. To make the nanoclusters compatible for biological applications the ligand design becomes important. Researchers explored plethora of ligands including proteins, peptides, DNA sequences, polymers, and dendrites to synthesize Au nanoclusters with different size and moreover with distinct properties like photoluminescence, sensing and molecular probes. Ying and coworkers reported the use of bovin serum albumin (BSA) protein as a capping ligand for the synthesis of highly fluorescent gold nanoclusters.[61] The nanocluster was reported to be

Au_{25} capped with BSA ligand. This work was followed by many research groups; several other proteins like HSA, lysozyme, trypsin and other ferritin family of proteins were reported for the synthesis of Au nanoclusters.[62-65] With respect to polymers and dendrimers, Tan and coworkers used thioether polymer ligand to prepare Au and Ag nanoclusters with strong blue fluorescence.[66] Dickson and coworkers used different dendrimers to synthesize Au nanoclusters with strong fluorescence.[67] Chen and coworkers employed DNA, peptides, and amino acids to synthesize atomically precise Au nanoclusters where they performed biomolecular etching of bigger nanoparticles or nanorods.[68]

1.7 Thesis overview

This dissertation focuses on the synthesis of water-soluble gold and silver nanoclusters. The goal is to achieve enhanced stability, study the optical and chiroptical properties of various ligand capped gold clusters and application of these nanoclusters in diverse fields.

Chapter 2 focuses on the synthesis of water-soluble Au_{25} nanoclusters capped with (*2S*)-1-[(*2S*)-2-methyl-3-sulfanylpropanoyl]pyrrolidine-2-carboxylic acid also called Captopril (Capt for short). The rationale of using Captopril as a ligand is to achieve high thermal stability for water-soluble Au_{25} nanoclusters. In addition to the thermal stability, the enhanced photoluminescence and chiroptical response of $Au_{25}(Capt)_{18}$ clusters are compared with the reported clusters. Also, the quantum confinement of the Au_{25} nanoclusters and its effect on its optical properties are compared with the Au nanocrystals or plasmonic nanoparticles.

Chapter 3 describes the enantioselective synthesis of Au_{38} nanoclusters in high yield. The synthesis of enantiomerically pure nanoclusters has been a challenge in the field of nanoclusters. The chirality of metal core and the capping ligand governs the overall chirality of the nanoclusters. In this work the synthesis of enantiomerically pure Au_{38} nanoclusters has been achieved by using optically active ligand. The origin of chirality and the enantiomeric purity of the cluster are compared with the literature. Also, this chapter involves synthesis and isolation of water-soluble Au_{40} nanoclusters capped with captopril and their optical purity.

Chapter 4 focuses on the origin of photoluminescence properties in gold nanoclusters. In that regard, the effect of capping ligand and the varying core size has been studied. The steady state and time resolved photoluminescence properties of these clusters are studied to better understand the mechanism of fluorescence as the core size or the ligand shell changes. Also, the

fluorescence properties are studied at cryogenic temperature to understand the electronic contribution in the fluorescence mechanism.

Chapter 5 explains all the ongoing work and finally concludes our work on synthesis and application of these water-soluble nanoclusters. The synthesis of silver nanoclusters to uncover the exact boundary where the transition from molecular behavior to plasmonic behavior will be demonstrated. This chapter also focuses on the application of nanoclusters in diverse directions. The optical, photoluminescence, chiroptical, and high thermal stability properties of nanoclusters are explored in practical applications such as catalysis, cancer biology, and energy science.

1.8 References

1) Faraday, M. *Philos. Trans. R. Soc. London* **1857**, *147*, 145-181.
2) Turkevich, J.; Stevenson, P. C.; Hillier, J. *Discuss. Faraday Soc.* **1951**, *11*, 55-75.
3) Frens, G. *Colloid Polym. Sci.* **1972**, *250*, 736-741.
4) Frens, G. *Nature* **1973**, *241*, 20-22.
5) Lee, P. C.; Meisel, D. *J. Phys. Chem.* **1982**, *86*, 3391-3395.
6) Hess, P. H.; Parker, P. H. *J. Appl. Polym. Sci.* **1966**, *10*, 1915-1927.
7) Griffiths, C. H.; O'Horo, M. P.; Smith, T. W. *J. Appl. Phys.* **1979**, *50*, 7108-7115.
8) Rossetti, R.; Brus, L. *J.Phys.Chem.***1982**, *86*, 4470-4472.
9) Bard, A. J. *Science* **1980**, *207*, 139-144.
10) Schmid, G.; Pfeil, R.; Boese, R.; Bandermann, F.; Meyer, S.; Calis, G. H. M.; van der Velden, J. W. A. *Chem. Ber.* **1981**, *114*, 3634-3642.
11) Bain, C. D.; Evall, J.; Whitesides, G. M. *J. Am.Chem. Soc.* **1989**, *111*, 7155-7164.
12) Bain, C. D.; Whitesides, G. M. Angew. *Chem. Int. Ed.* **2003**, *28*, 506-512.
13) Dubois, L. H.; Nuzzo, R. G. *Annu. Rev. Phys. Chem.* **1992**, *43*, 437-463.
14) Brust, M.; Walker, M.; Bethell, D.; Schiffrin , D. J.; Whyman, R. *J. Chem. Soc.* **1994**, 801-802.
15) Brust, M.; Fink, J.; Bethell, D.; Schiffrin, D.; Kiely, C. *J. Chem. Soc.* **1995**, 1655-1656.
16) Brust, M.; Schiffrin, D. J.; Bethell, D.; Kiely, C. *J. Adv. Mater.* **2004**, *7*, 795-797.
17) Willets, K. A.; Van Duyne, R. P. *Annu. Rev. Phys. Chem.* **2007**, *58*, 267-297.
18) Link, S.; El-Sayed, M. A. *J. Phys. Chem. B* **1999**, *103*, 8410-8426.
19) Terrill, R. H.; Postlethwaite, T. A.; Chen, C.-h.; Poon, C.-D.; Terzis, A.; Chen, A.; Hutchison, J. E.; Clark, M. R.; Wignall, G.; Londono, J. D.; Superfine, R.; Falvo, M.; Johnson Jr, C. S.; Samulski, E. T.; Murray, R. W. *J. Am. Chem. Soc.* **1995**, *117*, 12537-12548.
20) Hostetler, M. J.; Green, S. J.; Stokes, J. J.; Murray, R. W. *J. Am. Chem. Soc.* **1996**, *118*, 4212-4213.
21) Hostetler, M. J.; Wingate, J. E.; Zhong, C.-J.; Harris, J. E.; Vachet, R. W.; Clark, M. R.; Londono, J. D.; Green, S. J.; Stokes, J. J.; Wignall, G. D.; Glish, G. L.; Porter, M. D.; Evans, N. D.; Murray, R. W. *Langmuir* **1998**, *14*, 17-30.
22) Chen, S.; Murray, R. W. *Langmuir* **1998**, *15*, 682-689.

23) Johnson, S. R.; Evans, S. D.; Brydson, R. *Langmuir* **1998**, *14*, 6639-6647.

24) Ackerson, C. J.; Jadzinsky, P. D.; Kornberg, R. D. *J. Am. Chem. Soc.* **2005**, *127*, 6550-6551.

25) Alvarez, M.; Khoury, J.; Schaaff, T.; Shafigullin, M.; Vezmar, I.; Whetten, R. *Chem. Phys. Lett.* **1997**, *266*, 91-98.

26) Wilcoxon, J. P.; Martin, J. E.; Provencio, P. *Langmuir* **2000**, *16*, 9912-9920.

27) Song, Y.; Jimenez, V.; McKinney, C.; Donkers, R.; Murray, R. W. *Anal. Chem.* **2003**, *75*, 5088-5096.

28) Jimenez, V. L.; Leopold, M. C.; Mazzitelli, C.; Jorgenson, J. W.; Murray, R. W. *Anal. Chem.* **2003**, *75*, 199-206.

29) Zhong, C.; Zhang, W.; Leibowitz, F.; Eichelberger, H. *Chem. Commun.* **1999**, 1211-1212.

30) Stoeva, S.; Klabunde, K. J.; Sorensen, C. M.; Dragieva, I. *J. Am. Chem. Soc.* **2002**, *124*, 2305-2311.

31) Prasad, B.; Stoeva, S. I.; Sorensen, C. M.; Klabunde, K. J. *Langmuir* **2002**, *18*, 7515-7520.

32) Lin, X.; Wang, G.; Sorensen, C.; Klabunde, K. *J. Phys. Chem.B* **1999**, *103*, 5488-5492.

33) Hussain, I.; Graham, S.; Wang, Z.; Tan, B.; Sherrington, D. C.; Rannard, S. P.; Cooper, A. I.; Brust, M. *J. Am. Chem. Soc.* **2005**, *127*, 16398-16399.

34) Wang, Z.; Tan, B.; Hussain, I.; Schaeffer, N.; Wyatt, M. F.; Brust, M.; Cooper, A. I. *Langmuir* **2007**, *23*, 885-895.

35) Yao, H.; Kojima, H.; Sato, S.; Kimura, K. *Langmuir* **2004**, *20*, 10317-10323.

36) Alvarez, M. M.; Khoury, J. T.; Schaaff, T. G.; Shafigullin, M. N.; Vezmar, I.; Whetten, R. L. *J. Phys. Chem.B* **1997**, *101*, 3706-3712.

37) Whetten, R. L.; Shafigullin, M. N.; Khoury, J. T.; Schaaff, T. G.; Vezmar, I.; Alvarez, M. M.; Wilkinson, A. *Accounts Chem. Res.* **1999**, *32*, 397-406.

38) Cleveland, C. L.; Landman, U.; Schaaff, T. G.; Shafigullin, M. N.; Stephens, P. W.; Whetten, R. L. *Phys. Rev. Lett.* **1997**, *79*, 1873-1876.

39) Schaaff, T.; Shafigullin, M.; Khoury, J.; Vezmar, I.; Whetten, R.; Cullen, W.; First, P.; Gutierrez-Wing, C.; Ascensio, J.; Jose-Yacaman, M. *J. Phys. Chem. B* **1997**, *101*, 7885-7891.

40) Schaaff, T. G.; Knight, G.; Shafigullin, M. N.; Borkman, R. F.; Whetten, R. L. *J. Phys. Chem. B* **1998**, *102*, 10643-10646.

41) Donkers, R. L.; Lee, D.; Murray, R. W. *Langmuir* **2004**, *20*, 1945-1952.
42) Jimenez, V. L.; Georganopoulou, D. G.; White, R. J.; Harper, A. S.; Mills, A. J.; Lee, D.; Murray, R. W. *Langmuir* **2004**, *20*, 6864-6870.
43) Quinn, B. M.; Liljeroth, P.; Ruiz, V.; Laaksonen, T.; Kontturi, K. *J. Am. Chem. Soc.* **2003**, *125*, 6644-6645.
44) Abad, J. M.; Sendroiu, I. E.; Gass, M.; Bleloch, A.; Mills, A. J.; Schiffrin, D. J. *J. Am. Chem. Soc.* **2007**, *129*, 12932-12933.
45) Negishi, Y.; Takasugi, Y.; Sato, S.; Yao, H.; Kimura, K.; Tsukuda, T. *J. Am. Chem. Soc.* **2004**, *126*, 6518-6519.
46) Negishi, Y.; Nobusada, K.; Tsukuda, T. *J. Am. Chem. Soc.* **2005**, *127*, 5261-5270.
47) Shichibu, Y.; Negishi, Y.; Tsunoyama, H.; Kanehara, M.; Teranishi, T.; Tsukuda, T. *Small* **2007**, *3*, 835-839.
48) Zhu, M.; Lanni, E.; Garg, N.; Bier, M. E.; Jin, R. *J. Am. Chem. Soc.* **2008**, *130*, 1138-1139.
49) Zhu, M.; Qian, H.; Jin, R. *J. Am. Chem. Soc.* **2009**, *131*, 7220-7221.
50) Qian, H.; Zhu, M.; Andersen, U. N.; Jin, R. *J. Phys. Chem. A* **2009**, *113*, 4281-4284.
51) Qian, H.; Jin, R. *Nano Lett.* **2009**, *9*, 4083-4087.
52) Qian, H.; Zhu, Y.; Jin, R. *J. Am. Chem. Soc.* **2010**, *132*, 4583-4585.
53) Qian, H.; Jin, R. *Chem. Commun.* **2011**, *47*, 11462-11464.
54) Balasubramanian, R.; Guo, R.; Mills, A. J.; Murray, R. W. *J. Am. Chem. Soc.* **2005**, *127*, 8126-8132.
55) Qian, H.; Zhu, M.; Lanni, E.; Zhu, Y.; Bier, M. E.; Jin, R. *J. Phys. Chem. C* **2009**, *113*, 17599-17603.
56) Jadzinsky, P. D.; Calero, G.; Ackerson, C. J.; Bushnell, D. A.; Kornberg, R. D. *Science* **2007**, *318*, 430-433.
57) Zhu, M.; Aikens, C. M.; Hollander, F. J.; Schatz, G. C.; Jin, R. *J. Am. Chem. Soc.* **2008**, *130*, 5883-5885.
58) Heaven, M. W.; Dass, A.; White, P. S.; Holt, K. M.; Murray, R. W. *J. Am. Chem. Soc.* **2008**, *130*, 3754-3755.
59) Zhu, M.; Eckenhoff, W. T.; Pintauer, T.; Jin, R. *J. Phys. Chem. C* **2008**, *112*, 14221-14224.
60) Qian, H.; Eckenhoff, W. T.; Zhu, Y.; Pintauer, T.; Jin, R. *J. Am. Chem. Soc.* **2010**, *132*, 8280-8281.

61) Xie, J.; Zheng, Y.; Ying, J. Y. *J. Am. Chem. Soc.* **2009**, *131*, 888-889.
62) Hu, L.; Han, S.; Parveen, S.; Yuan, Y.; Zhang, L.; Xu, G. *Biosens.and Bioelect.* **2012**, *32*, 297-299.
63) Le Guével, X.; Daum, N.; Schneider, M. *Nanotechnology* **2011**, *22*, 275103.
64) Zhou, T.; Huang, Y.; Li, W.; Cai, Z.; Luo, F.; Yang, C. J.; Chen, X. *Nanoscale* **2012**, *4*, 5312-5315.
65) Chen, T. H.; Tseng, W. L. *Small* **2012**, *8*, 1912-1919.
66) Huang, X.; Li, B.; Li, L.; Zhang, H.; Majeed, I.; Hussain, I.; Tan, B. *J. Phys. Chem. C* **2011**, *116*, 448-455.
67) Zheng, J.; Petty, J. T.; Dickson, R. M. *J. Am. Chem. Soc.* **2003**, *125*, 7780-7781.
68) Zhou, R.; Shi, M.; Chen, X.; Wang, M.; Chen, H. *Chem-Eur J.* **2009**, *15*, 4944-4951.

Chapter 2

Water-Soluble $Au_{25}(Capt)_{18}$ Nanoclusters: Synthesis, Thermal Stability, and Optical Properties

2.1 Introduction

Metal nanoclusters of gold having 10 to few dozen atoms constitute a new class of material that has been extensively studied in recent years.[1-9] The size (less than 2 nm) of these nanoclusters differentiates them from bulk gold and gold nanocrystals. This size effect leads to the discrete electronic structure of the core due to the quantum size effect.[10,11] Because of this effect, the absorption spectrum for these clusters shows a step-like absorption. The unique size and electronic arrangement of these clusters are responsible for various interesting properties like chirality,[12-18] magnetism,[19-21] redox properties,[2,22,23] and also their potential applications in catalysis,[24-26] and bio-labeling and imaging.[27-29] The significance of these clusters have led to the synthesis, characterization, and application of various cluster size with atomic precision.[2,30-43] Further insight into their structural arrangement was established by the total structure determination of $Au_{102}(SR)_{44}$,[38] $Au_{25}(SR)_{18}$,[44,45] and $Au_{38}(SR)_{24}$[16] by single crystal X-ray crystallography. The structure determination not only explained the nature of bonding between the core gold atoms in these molecular clusters, but also explained the nature of gold-sulfur bonding. It also elucidated the structure and bonding in staple motifs like Au_2SR_2 and Au_2SR_3 which passivates the Au core in these clusters. Knowing the structural arrangement also helped in explaining the spectral properties of these clusters which were a result of electronic transitions.[45] Among all these thiolate protected clusters, $Au_{25}(SR)_{18}$ and $Au_{144}(SR)_{60}$ are most widely studied due to their high stability in comparison to the other cluster sizes. The synthesis of these clusters and other stable clusters are always mediated by thiols soluble in organic solvents. As a result the nanoclusters are soluble in organic solvents only. The water-solubility of the nanoclusters becomes important for many applications such as bio-labelling, imaging, and therapeutics. Although there has been reports of several gold nanoclusters capped with proteins,

peptides, DNA sequences, polymers, and dendrites in last few years, their composition and stability has always been questionable. The synthesis of atomically precise, water-soluble metal nanoclusters has largely been limited to the gold-glutathione system.[12,37] Tsukuda *et al* for the first time reported the synthesis of different Au_n clusters capped with glutathione (GSH). The different core-sized nanoclusters have been isolated by separating the polydisperse $Au_n(SG)_m$ clusters through poly acrylamide gel electrophoresis (PAGE). This method always led to the low yield of any specific core size, as a statistical distribution of sizes were observed, albeit $Au_{25}(SG)_{18}$ was the predominant species. Tsukuda *et al* also reported a large scale synthesis of $Au_{25}(SG)_{18}$ clusters by the ligand exchange reaction of $Au_{11}(PPh_3)_8Cl_3$ with glutathione.[46] However, the stability of $Au_{25}(SG)_{18}$ cluster has always been ambiguous at high temperature. The hydrolysis of GSH to pyroglutamic acid has always been observed in the ESI-mass spectrometry of these clusters.[37] The fragile nature of these clusters has always been a concern not limited to mass spectrometric studies. Poor stability limits the application of these clusters in catalysis and other biological application where several other nanoclusters with aromatic thiol capping have been used. The stability of $Au_{25}(SG)_{18}$ cluster has also prevented it from any type of crystallization studies. Although the Au_{25} system is stable, the nature of glutathione ligand plays an important role in its stability. Glutathione (GSH) is a tripeptide (γ-Glu-Cys-Gly). It exists as disulphide GSSG. The bulky size of this ligand, easily hydrolysable amide bond, and stability restricted to lower temperatures makes it vulnerable to different degradation process.

The synthesis of stable clusters like $Au_{25}(SCH_2CH_2Ph)_{18}$, $Au_{38}(SCH_2CH_2Ph)_{24}$, $Au_{102}(p\text{-}MBA)_{44}$ has always been done with the ligand having a rigid structure. The ligands phenyl ethane thiol or *p*-mercapto benzoic acid have a rigid benzene ring. This provides a certain degree of stability to the ligand structure. To get the same extent of stability, and still achieve water solubility, the design of ligand is very critical. This motivated us to choose (*2S*)-1-[(*2S*)-2-methyl-3-sulfanylpropanoyl] pyrrolidine-2-carboxylic acid (Captopril) as a ligand for the synthesis of the most explored Au nanocluster size Au_{25}. Captopril is a L-proline derivative. It has been used as a drug for the treatment of hypertension and congestive heart failure. The use of captopril as a ligand for nanocluster syntehsis has been recently reported by Kitaev *et al* for the synthesis of chiral Ag nanoclusters[47] but the stability of Ag nanoclusters limited the exploration of verstality of captopril as a choice of ligand for the synthesis.

In this chapter, we report the synthesis of Au_{25} cluster capped with captopril. The choice of captopril was not just based on its water solubility, but the five-membered pyrrolidone ring was expected to provide the same structural rigidity and stability as observed in case of phenyl ethane thiol ligand. The Au_{25} core is achiral but the chiral ligands induces some degree of chirality in the visible region to the cluster system. Since captopril in its original form is chiral, Au_{25} cluster capped with captopril should be chiral. The chirality of Au_{25} capped with three chiral ligands has been studied. Also, the thermal stability of $Au_{25}Capt_{18}$ system has been compared with $Au_{25}SG_{18}$ system to show its enhanced stability as compared to the glutathione system. The photoluminescence properties of $Au_{25}Capt_{18}$ nanoclusters are studied and compared with $Au_{25}SG_{18}$ at room temperature and at elevated temperatures.[48] Finally the absorption properties of Au_{25} nanoclusters capped with different ligands are compared with plasmonic nanoparticle or nanocrystal system to show the effect of quantum confinement on the optical absorption properties of these clusters.[49]

2.2 Experimental

2.2.1 Synthesis of Au_{25} nanoclusters

Synthesis of $Au_{25}(Capt)_{18}$: The synthesis of $Au_{25}Capt_{18}$ was done at room temperature in air. Typically $HAuCl_4.3H_2O$ (0.20mmol, 78.7 mg) and ToABr (0.23 mmol, 126.8 mg) was fisrt dissolved in 10 ml methanol and vigorously stirred for 20 min. The solution color changed from yellow-orange to deep red. After 20 min, Captopril (1 mmol, 217.2 mg) was dissolved in 5 ml methanol and rapidly injected in the the reaction mixture and further stirred for 30 min. The solution color quickly changed to white. After 30 min, $NaBH_4$ (2 mmol, 75.6mg) was disoolved in 5 ml of ice cold water and rapidly added with vigorous stirring. The solution color immediately changed to brown-black. The reaction was further run for 8 hr and then the reaction mixture was centrifuged to remove insoluble Au (I) polymer. The supernatant was collected and further concentrated by rotatry evapouration and then precipitated by adding ethanol. The precipitate was extracted several times with minimum ammount of methanol and finally precipitated by ethanol and dried in vacuum. The synthetic outline is shown in scheme 2.1 (A)

Synthesis of $Au_{25}(SG)_{18}$: The synthesis of $Au_{25}(SG)_{18}$ was done in two steps. First the $Au_n(SG)_m$ clusters were prepared by previously reported protocol. This polydisperse mixture was then etched with excess of glutathione at 55 °C in water. The etched product was then centrifuged to

remove insoluble Au(I):SR polymer and the supernatant was precipitated with ethanol. The precipitate was washed several times with ultrasonication and centrifugation to get the clean product. This etched product was run through the PAGE gel to obtain ultra pure $Au_{25}(SG)_{18}$ clusters as a major product (will be described in the next section). The synthetic outline is shown in scheme 2.1(B).

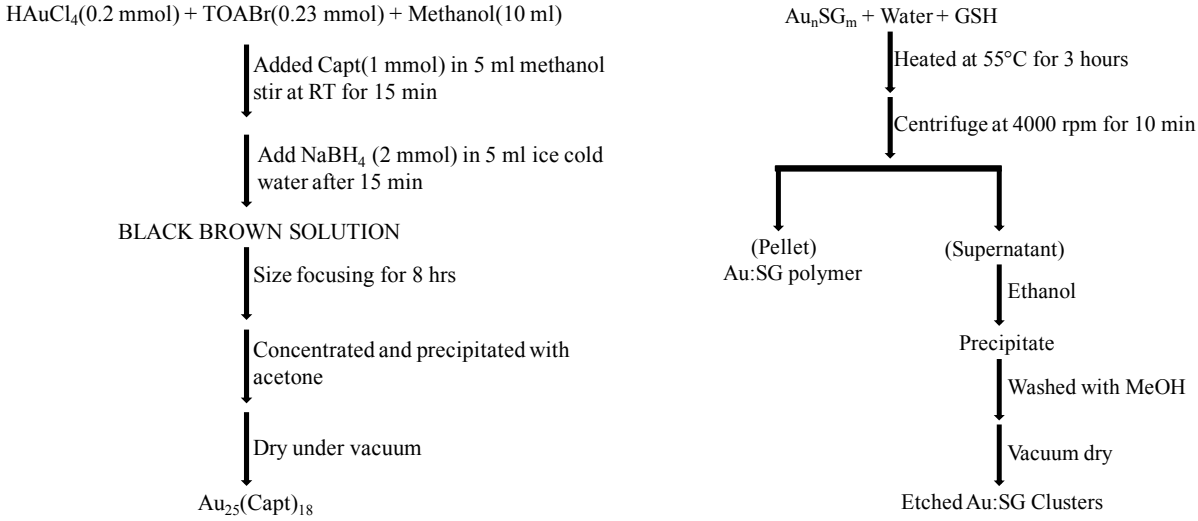

Scheme 2.1 (A) Synthesis of $Au_{25}Capt_{18}$ cluster with gold salt precursor left panel **(B)** Synthesis of etched Au:SG clusters right panel.

Synthesis of $Au_{25}(PET^{*})_{18}$: The Au_{25} capped with *S*-phenylpropane-1-thiol (PET^{*}) was done at room temperature in air. Typically $HAuCl_4.3H_2O$ (0.20mmol, 78.7 mg) and ToABr (0.23 mmol, 126.8 mg) was fisrt dissolved in 15 ml THF and vigorously stirred for 20 min. The solution color changed from yellow-orange to deep red. After 20 min, *S*-phenylpropane-1-thiol (1 mmol, 170 µl) was rapidly added in the the reaction mixture and further stirred for 30 min. The solution color quickly changed to white. After 30 min, $NaBH_4$ (2 mmol, 75.6mg) was disoolved in 5 ml of ice cold water and rapidly added with slow stirring(~100 rpm). The solution color immediately changed to brown-black. The stirring speed was further increased to 800 rpm after 5 min. The reaction was further run for 4-6 hr and then the reaction mixture was concentrated by rotatry evapouration and then methanol was added to the reaction mixture to precipitate the clusters. The precipitated clusters were repeatedly washed with methanol to remove unreacted thiols and reagents. The precipitate was finally extracted with MeCN to obtain pure

$Au_{25}(PET^{*})_{18}$ clusters. The MeCN solution was then evapourated in N_2 environment and further dried in vacuum.

2.2.2 Purification by polyacrylamide gel electrophoresis (PAGE)

PAGE has been utilized by biochemists for a very long time to separate and purify proteins. The gel separates the proteins on the basis of molecular weight. For proteins, the molecular mass is quite large and the size is quite big so they can be separated by a low density gel (4-15%). For nanoclusters, although the mass could range from 5-40 kDa, their hydrodynamic radii is quite small as they have a metallic core which is more densely packed than proteins. In order to separate the nanoclusters from the gel, the pore-size of the PAGE gel should be quite small. This can be done by increasing the monomer (acrylamide) concentartion and also the cross-linker (bis-acrylamide) concentartion. To separate the nanoclusters effectively, we increased the monomer concentartion in the range of 20-35 % with the cross linker concentration of 4-7 %. The other modification we made to run the nanoclusters through the gel is to run them without adding any sodium dodecyl sulfate (SDS). As the nanoclusters are negatively charged, they separate on the basis of their mass with lower molecular mass cluster travelling the farthest. Also, the nanoclusters are colored and did require any staining with a dye.

PAGE serves both as a qualitative and quantitative technique for nanoclusters. We have succesfully and precisely separated ~60 mg of nanoclusters in one run which can not be possible by any other technique for such a small system. The purity of a sample can be seen by the number of bands it separates into, and the width of the band gives a quantitative estimate of a particular size. PAGE experiment was carried by using OWL P10DS-2 vertical gel electrophoresis system. The gel size was 20 cm × 20 cm. The separating and stacking gel was prepared with 30 and 4 % monomer (acrylamide) concentration respectively with 4 % concentration of cross linker bis-acrylamide for best separation. The gel was eluted with 25 mM tris and 192 mM glycine buffer for 16 hr at 300V. The cluster was dissolved in 10 % v/v glycerol/water and loaded in the gel.

The as synthesized $Au_{25}(Capt)_{18}$ was dissolved in 10 % v/v glycerol/water and loaded in the gel with a high loading of 80 µl/well at a concentartion of 30 mg/ml. The high loading was to ensure that any impurity from smaller or bigger size be disctinctly visible, thus will be a qualitative test for the purity of the nanoclusters. The biggest advantage of running a nanoclusters sample through the gel is not just separating it from other nanoclusters, but the unreacted ligand or other

small molecule which is present as impurities travels faster than nanoclusters and hence easily get separated. $Au_{25}(Capt)_{18}$ appears as a single thick band with orange appearance with no visible sign of any band of either smaller or bigger mass as shown in figure 2.1 (A). The thick orange band ($Au_{25}(Capt)_{18}$) in the gel matrix was then cut, crushed and soaked in water for 2 hr. The nanoclusters due to their water-solubility, diffuse in water. The nanocluster solution with gel matrix was then filtered with 0.2 µm filter and concentrated by a cut off filter of 3 kDa. The concentarted solution was then precipitated with acetone and dried in vacuum to obtain ultra pure clusters $Au_{25}(Capt)_{18}$.

For the PAGE separation of the etched Au:SG cluster, it was dissolved in 10 % v/v glycerol/water and then loaded in the gel with a loading of 40 µl/well at a concentartion of 10 mg/ml. The lower loading was to insure the better separation of the nanoclusters of different size into well resolved band. The etched Au:SG clusters separated into 4 distinct well resolved band with $Au_{25}(SG)_{18}$ being the most dominant band as shown in figure 2.1 (B). The $Au_{25}(SG)_{18}$ portion was then cut, crushed and soaked in water for 2 hr. The $Au_{25}(SG)_{18}$ nanocluster solution with gel matrix was then filtered with 0.2 µm filter and concentrated by a cut off filter of 3 kDa. The concentarted solution was then precipitated with ethanol and dried in vacuo to obtain ultra pure clusters $Au_{25}(SG)_{18}$.

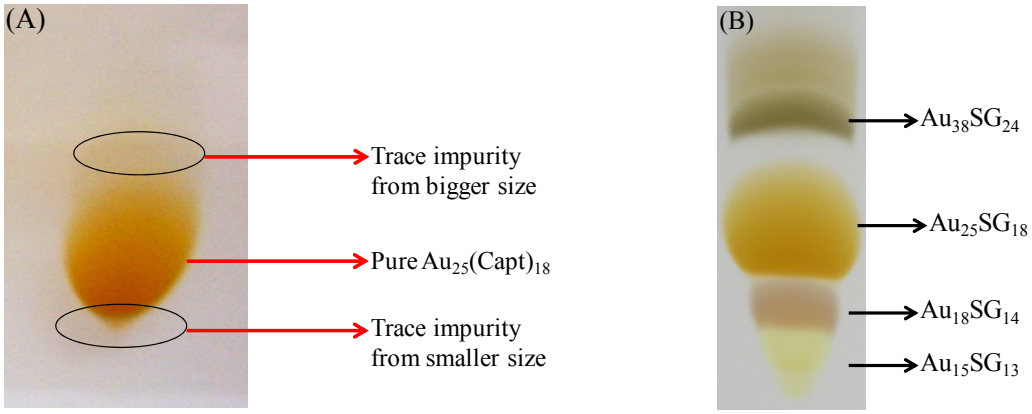

Figure 2.1 (A) PAGE gel image showing a thick band of $Au_{25}(Capt)_{18}$ with no impurity from bigger or smaller size, **(B)** PAGE image showing 4 distinct bands with $Au_{25}(SG)_{18}$ appeared as the most dominant band.

2.2.3 Characterization

UV-Vis spectra of the Au_{25} clusters were acquired by Hewlett- Packard (HP) Agilent 8453 diode array spectrophotometer at room temperature. Thermal stability was monitored by Hewlett-Packard (HP) Agilent 8453 diode array spectrophotometer quipped with Agilent 89090A temperature probe. Fluorescence spectra were recorded on a Fluorolog-3 spectrofluorometer (HORIBA Jobin Yvon). The excitation wavelength was fixed at 514 nm (from a Xe arc source) for all the cluster species in emission measurements. Electrospray ionization (ESI) mass spectra were recorded using a Waters Q-TOF mass spectrometer equipped with a Z spray source. The sample was dissolved in 50 % water/methanol mixture and injected at a flow rate of 5 μL/min. MALDI-MS were performed on a PerSeptiveBiosystems Voyager DE super-STR time-of-flight (TOF) mass spectrometer. 2,4-dihydroxy benzoic acid was acid as a matrix. Thermal gravimetric analysis (TGA) was obtained on a TG/DTA6300 analyzer (Seiko Instruments, Inc.) under a N_2 atmosphere (flow rate ~50 mL/min). NMR spectra were recorded at Bruker Avance™ 300 spectrometer operating at 300 MHz for ^1H using standard Brucker software. The chiroptical properties of Au_{25} clusters were measured on a JASCO J-810 CD spectrometer. $Au_{25}(SG)_{18}$ and $Au_{25}(Capt)_{18}$ were dissolved in water and S-$Au_{25}(PET^*)_{18}$ was dissolved in CH_2Cl_2. All the measurement was done at ambient temperature and under N_2 atmosphere.

2.3 Results and Discussion

2.3.1 Synthesis of $Au_{25}(Capt)_{18}$ clusters

The synthesis of $Au_{25}(Capt)_{18}$ was done in methanol as a solvent. Although Captopril is soluble in variety of solvents like water, methanol, ethanol, THF, and other polar organic solvents, the choice of solvent was critical for the controlled nucleation and growth process. The use of highly polar solvent like water can lead to the uncontrolled nucleation and despite the kinetic control on the growth process the size distribution can result to Au_{25} and other smaller size clusters. Similarly, use of less polar solvent like THF could shift the growth towards bigger particles. The synthesis was done in variety of solvents and the growth process was monitored with UV-Vis spectroscopy, and finally it was concluded that a non solvent like methanol works best for the kinetically controlled growth of Au_{25} clusters. The reaction was continuously monitored by UV-Vis, as the absorbance spectra for Au_{25} works as an optical signature for identification of Au_{25} cluster. The peak at 450 nm and 670 nm is the characteristic of Au_{25}. After 8 hr of incubation the

features of Au_{25} became well pronounced as shown in figure 2.2(A). The clusters after the removal of Au (I) polymer and some unreacted material showed a pronounced peak of Au_{25} as shown in figure 2.2(B).

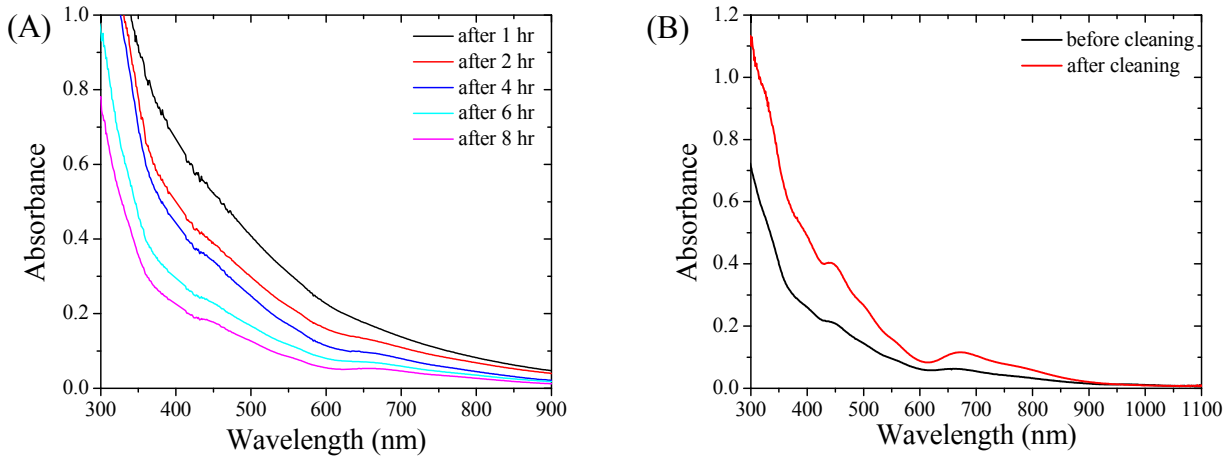

Figure 2.2 (A) Time evolution of the synthesis process (spectra has been offset for clarity). **(B)** $Au_{25}(Capt)_{18}$ before and after cleaning and precipitation. Reproduced from ref. 48 with permission. Copyright@ 2012 Royal Society of Chemistry.

The as separated clusters were sufficiently pure as observed from the spectral feature. However, the water solubility of the cluster gave an opportunity to run the sample through the PAGE. The high monomer concentration (30 %) of the gel allows separating the clusters based on their charge density. When $Au_{25}(Capt)_{18}$ was run through the gel, it was evident that $Au_{25}(Capt)_{18}$ was predominantly pure as shown in figure 2 .1(A). Running the sample through the gel helped removal of unreacted ligand and thiolate, which is evident from the enhancement in the feature of absorption spectra of the sample before and after running through the gel (figure 2.3).

2.3.2 Formula Assignment by TGA and mass-spectrometry

Although, the spectral features confirmed the identity of $Au_{25}(Capt)_{18}$, the sample was further characterized by TGA. Approximately 3 mg of the pure cluster was heated in N_2 atmosphere to monitor the loss of ligand and hence verify the purity and the assigned formula of $Au_{25}(Capt)_{18}$. The determined weight loss from TGA was 44.19 % which was extremely close to the calculated value of 44.14 % thus verifying the composition of the purified cluster. The $Au_{25}(Capt)_{18}$ started losing the ligands around 180°C as shown in figure 2.4.

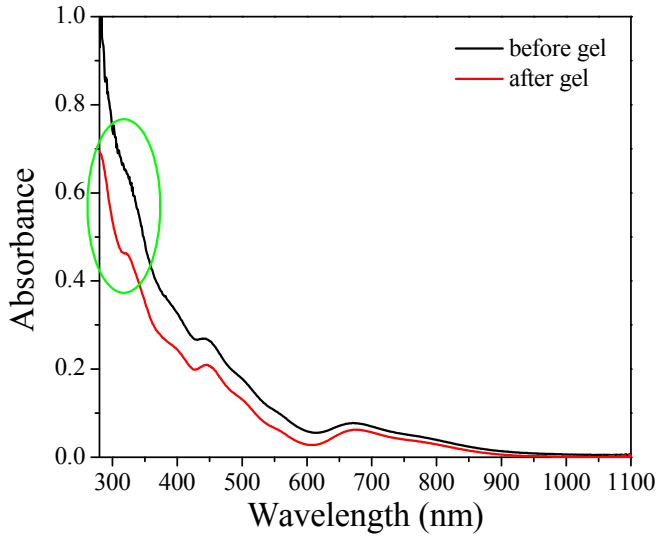

Figure 2.3 Absorbance spectra of $Au_{25}(Capt)_{18}$ before and after running through the gel.

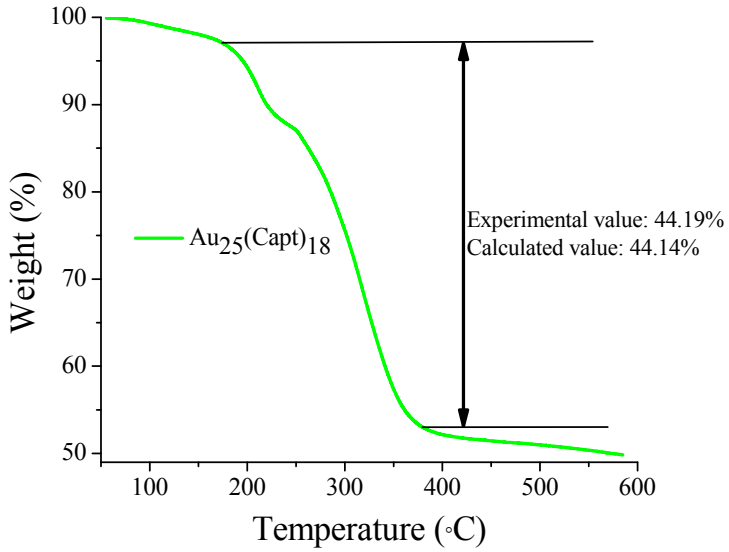

Figure 2.4 TGA data for $Au_{25}(Capt)_{18}$ showing the ligand loss.

The formula assignment was further confirmed by ESI-mass spectrometry. The ESI data can also confirm the presence of any fragmentation, explaining the stability of the clusters. The $Au_{25}(Capt)_{18}$ was dissolved in 50 % water/methanol mixture and injected at a flow rate of 5 µL/min. The ESI-mass spectrum showed a prominent peak at m/z 3101.6, with the 0.33 Da spacing of the isotope peaks indicating that the ions are 3+ charged (Figure 2.5 inset). The m/z 3101.6 is assigned to $[Au_{25}(Capt)_{18}Na_{22}]^{3+}$. The 22 Na atoms could be interpreted as all the 18 -

COOH groups of captopril are in sodium salt form and the native charge of $Au_{25}(Capt)_{18}^{-}$ was neutralized by an extra Na^{+}, with the three remaining Na^{+} imparting 3+ charge to the overall cluster. This was further conformed by simulation of the isotope pattern according to the elemental formula $Au_{25}(SC_9H_{13}NO_3Na)_{18}Na_4$. The simulation data perfectly matches with the experimental pattern (Figure 2.5 inset). The small peak at m/z 3040.6 (3+) is caused by two ligand loss with the same core. Importantly, the cluster showed no sign of fragmentation.

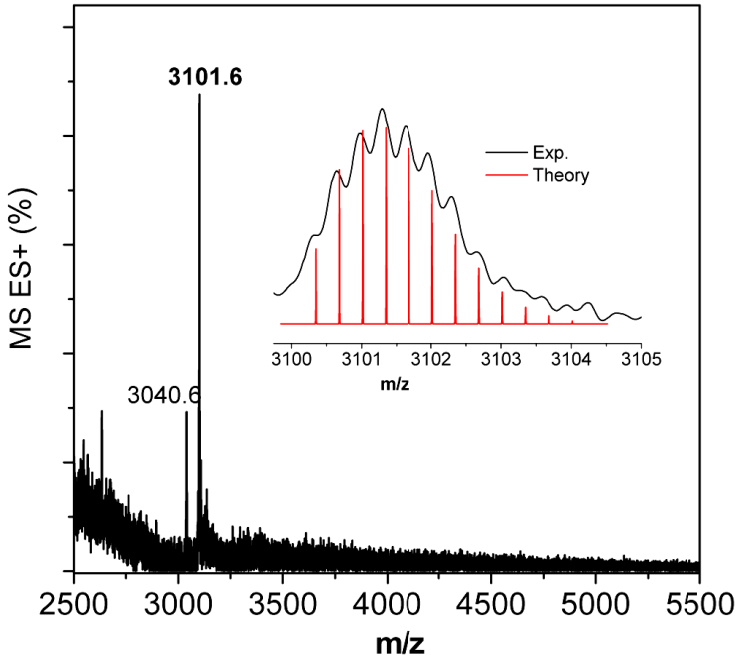

Figure 2.5 Positive mode ESI-MS analysis of the PAGE-purified product (Inset: the experimental and simulated isotope patterns; a formula of $Au_{25}(SC_9H_{13}NO_3Na)_{18}Na_4$ was used in the simulation). Reproduced from ref. 48 with permission. Copyright@ 2012 Royal Society of Chemistry.

To further verify the purity of the $Au_{25}(Capt)_{18}$ nanoclusters, we performed MALDI-MS analysis. MALDI can detect a much wider range than ESI. The $Au_{25}(Capt)_{18}$ nanoclusters and 2,4-dihydroxy benzoic acid (matrix) was both dissolved in water and then equal amount of matrix and the clusters solution was mixed and drop casted on the MALDI plate to co-crystallize. The laser power was maintained low to prevent any fragmentation. For the $Au_{25}(Capt)_{18}^{-}$ (counterion: Na^{+}), we did not find appreciable impurities (e.g. larger clusters), albeit the molecular ion peak was obtained with the loss of three ligand (figure 2.6).

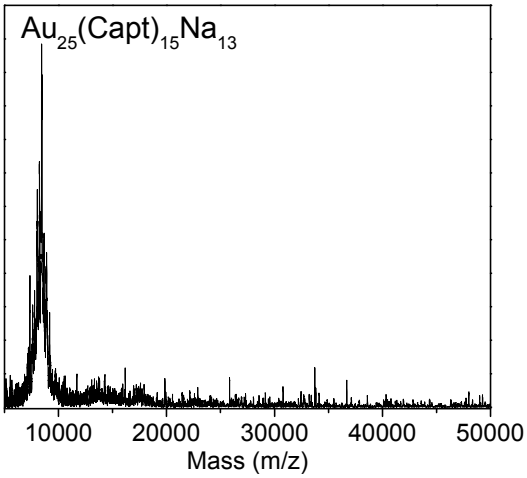

Figure 2.6 MALDI-MS spectra of $Au_{25}(Capt)_{18}$ clusters. Reproduced from ref. 48 with permission. Copyright@ 2012 Royal Society of Chemistry.

2.3.3 Thermal stability of $Au_{25}(Capt)_{18}$ clusters

The main focus of this work was to improve thermal stability for water soluble $Au_{25}(SR)_{18}$ nanoclusters as their stability has always been ambiguous. To determine the thermal stability, solutions of $Au_{25}(Capt)_{18}$ and $Au_{25}(SG)_{18}$ was made in water with nearly equal optical density and then heated at 80 °C for 12 hrs. The decay kinetics was monitored by UV-Vis. The spectra were recorded after every 30 min. The decay was monitored at 400, 450, 670, and 800 nm wavelength to quantify the degradation process. The absorption spectra for $Au_{25}(Capt)_{18}$ did not show any sign of degradation with time (figure 2.7 (A) top left panel), while $Au_{25}(SG)_{18}$ started degrading just after 4 hrs and in 12 hrs the spectra started looking featureless (figure 2.7 (B) top right panel).

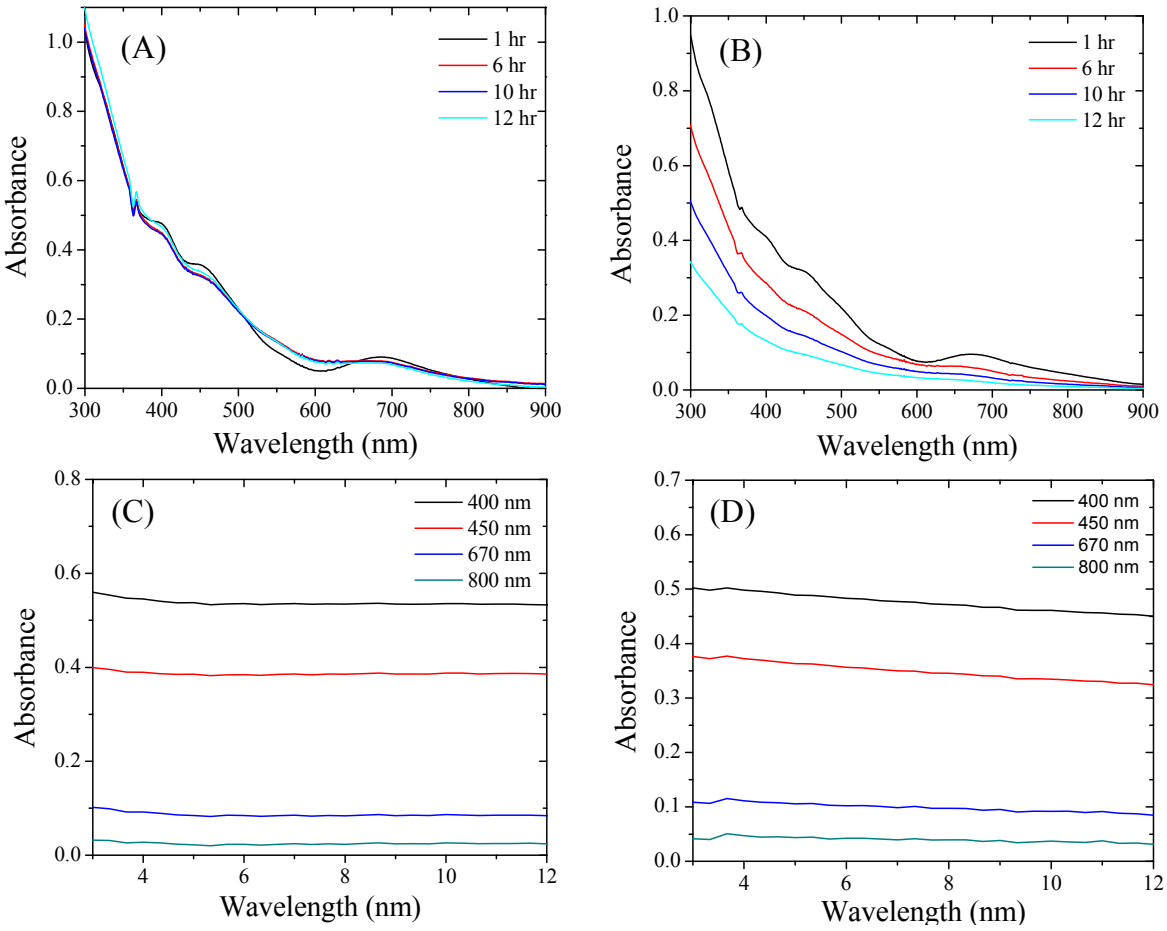

Figure 2.7 Time dependent thermal decay profile for **(A)** $Au_{25}(Capt)_{18}$ and **(B)** $Au_{25}(SG)_{18}$. The clusters were heated at 80 °C for 12 hr. Decay kinetics at different wavelength for **(C)** $Au_{25}(Capt)_{18}$ and **(D)** $Au_{25}(SG)_{18}$ clusters. Reproduced from ref. 48 with permission. Copyright@ 2012 Royal Society of Chemistry.

It is important to note that one-electron oxidation of $[Au_{25}(Capt)_{18}]^-$ to $[Au_{25}(Capt)_{18}]^0$ and finally to $[Au_{25}(Capt)_{18}]^+$ can shift the peak at 670, 450, 400 nm. This has already been observed in the previous study of Au_{25} nanoclusters capped with aromatic thiols.[23] The kinetic data for $Au_{25}(Capt)_{18}$, showed slight increase in the absorbance (at different wavelengths) in the beginning but became constant with time (figure 2.7 (C) bottom left panel). For $Au_{25}(SG)_{18}$ the absorbance showed a continuous decrease for all 4 wavelengths (see figure 2.7 (D) bottom left panel). This clearly establishes the high stability of $Au_{25}(Capt)_{18}$ with respect to $Au_{25}(SG)_{18}$. The solutions were heated till 24 hr and the absorption spectra were recorded. Captopril capped Au_{25} showed no sign of degradation while glutathione capped Au_{25} showed completely featureless spectra

(figure 2.8). Despite the two having the same Au_{25} metallic core, there stability is markedly different. This clearly indicates that it is the stability of Captopril over glutathione that governs the overall stability of the clusters.

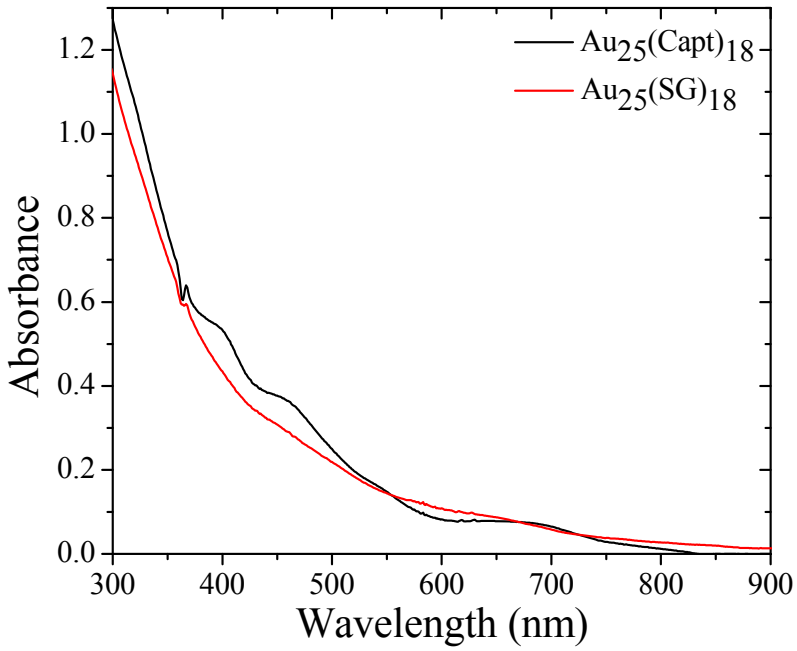

Figure 2.8 UV-Vis spectra of $Au_{25}(Capt)_{18}$ (black) and $Au_{25}(SG)_{18}$ (red) after heating for 24 hr at 80 °C

To visualize the effect of nanocluster degradation after heating, we took an aliquot of nanocluster solution of both Au_{25} nanoclusters and concentrated it to a lower volume ~ 70 µl. This concentrated solution was mixed with 5 µl of glycerol and loaded in the gel with the fresh solutions of nanoclusters and run side by side. For $Au_{25}(Capt)_{18}$ nanoclusters there was no sign of degradation in the gel image while $Au_{25}(SG)_{18}$ was completely degraded as shown in figure 2.9. Therefore, we concluded that the ligand plays an important role in the stability of the clusters and it is the stability of the ligand which dictates the overall stability of the nanoclusters. To prove this hypothesis we performed NMR experiment on the both the ligands. Equal concentration of glutathione and Captopril was prepared in D_2O and NMR spectra were recorded. Both the solution was then heated for 2 hr at 80 °C. The NMR spectra for Captopril was unchanged after heating, but the NMR spectra for glutathione changed and new peak appeared which clearly showed the degradation of glutathione as shown in figure 2.10. The new peaks in the NMR spectra, which appeared after heating glutathione ligand, corresponded to the pyroglutamic acid.

The degradation of glutathione to pyroglutamic acid has been observed in the ESI-mass spectrometry of $Au_{25}SG_{18}$ nanoclusters.[37] The hydrolysis of the amide bond in case of GSH leads to the degradation of the nanoclusters.

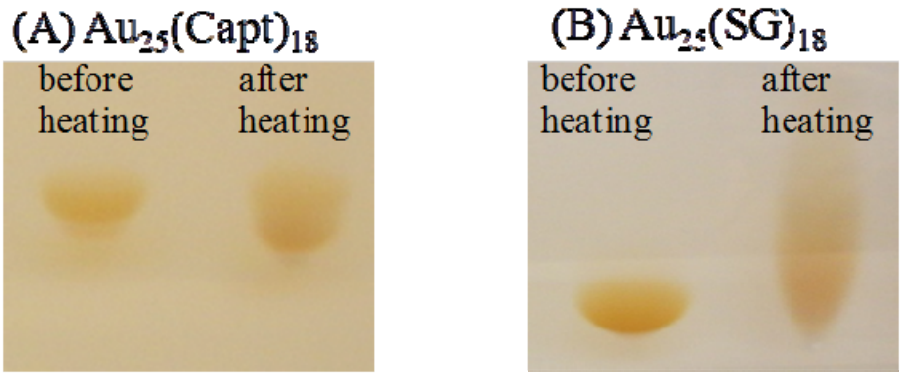

Figure 2.9 PAGE image of Au_{25} clusters after heating at 80 °C for 12 hr

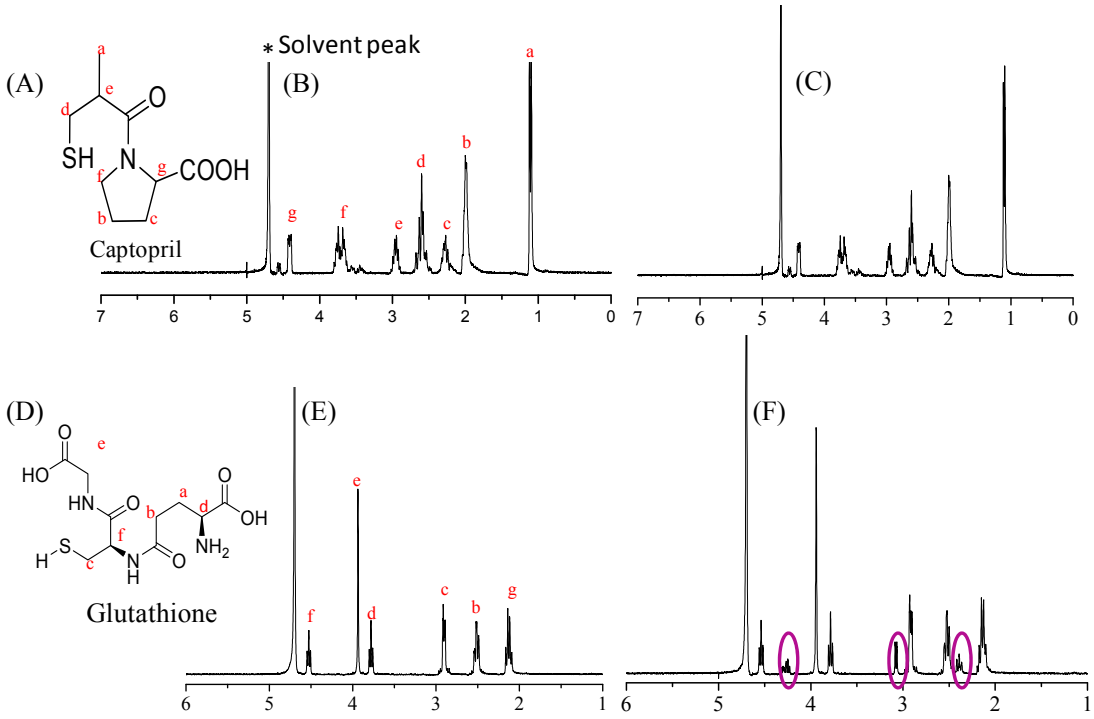

Figure 2.10 (A) and **(D)** refers to the structure of Captopril and Glutathione, **(B)** and **(E)** refers to the NMR spectra of Captoril and Glutathione in D_2O before heating, **(C)** and **(F)** refers to NMR of Captopril and Glutathione after heating at 80 °C. The NMR spectra of Glutathione

clearly shows some new peak after heating. Reproduced from ref. 48 with permission. Copyright@ 2012 Royal Society of Chemistry.

2.3.4 Photo-luminescence properties of Au_{25} nanoclusters

The fluorescence spectrum of $Au_{25}(Capt)_{18}$ was measured and compared with the $Au_{25}(SG)_{18}$ nanoclusters. The excitation wavelength was fixed at 514 nm. The $Au_{25}(SG)_{18}$ nanoclusters has been reported to have higher fluorescence intensity than any other reported Au_{25} nanoclusters capped with aromatic thiols.[50] The emission profiles were nearly the same for these two clusters, with Captopril capped Au_{25} having higher fluorescence than its glutathione counterpart, $Au_{25}(SG)_{18}$. This makes $Au_{25}(Capt)_{18}$ quite remarkable as it has enhanced photo-luminescence among all reported Au_{25} nanoclusters (figure 2.11). We have also compared the fluorescence of the two clusters before and after heating. Interestingly, both clusters exhibited a large enhancement in fluorescence during the 12 h heating process. The $Au_{25}(Capt)_{18}$ cluster showed an almost 20 times stronger fluorescence as compared to the room temperature sample and almost 11 times in comparison to the 1 h heated sample as shown in figure 2.12(A), while $Au_{25}(SG)_{18}$ showed twice more intense fluorescence compared to that prior to heating (or the 1 h heated sample). We speculate that the huge overall enhancement in the fluorescence is due to the change in the charge state of $Au_{25}(Capt)_{18}$ clusters (from -1 to 0 or +1), while the lower enhancement for $Au_{25}(SG)_{18}$ could be due to the degradation of majority of the nanoclusters in course of heating. Also, the electronic effect of the ligands can play a role in the overall luminescence properties.[50]

The huge enhancement in the fluorescence of $Au_{25}(Capt)_{18}$ after heating can be utilized in diverse way as the clusters shows significant fluorescence at room temperature but significantly high fluorescence after heating.

2.3.5 Chiroptical properties

The captopril is a proline derivative with L-configuration and has two chiral centers. We investigated the chiroptical properties of $Au_{25}(Capt)_{18}$ and compared it with other reported chiral ligand-capped $Au_{25}(SR)_{18}$ clusters, including –SG and $–SCH_2CH(Me)Ph$; the latter is a chirally modified analog of $–SCH_2CH_2Ph$ (abbreviated as PET*).[15] It is important to note here that the CD signals of all these chiral ligands lie in the UV region. However, for chiral ligand-capped nanoclusters, the CD signals are observed in the visible region which involves metal-based

electronic transitions; such signals are apparently not directly from the ligands, but from the metal cores due to a chiral induction effect.[15] We compared the CD spectra of $Au_{25}(SR)_{18}$ nanoclusters capped with the three chiral ligands mentioned above. All the three nanocluster solutions were prepared at the same optical density (0.1 OD at 670 nm) and their CD spectrum was recorded. The $Au_{25}(Capt)_{18}$ nanoclusters show two strong positive bands (at 275 and 480 nm) and two negative bands (at 310 and 430 nm) shown in figure 2.13 (C). For $Au_{25}(PET^{*})_{18}$, the CD spectra showed two strong negative bands (at 295 and 425 nm) while a weak positive band (at 550 nm) shown in figure 2.13 (B). The CD spectra of $Au_{25}(SG)_{18}$ showed three significant positive bands (at 275, 360, and 480 nm) while two weak negative bands (at 310 and 430 nm) shown in figure 2.13 (B). In Comparison to $Au_{25}(SG)_{18}$ and *S*-$Au_{25}(PET^{*})_{18}$ nanoclusters, the $Au_{25}(Capt)_{18}$ CD spectrum shows more intense positive band at ~480 nm and a more pronounced negative band at 430 nm. Therefore, the comparison of the chiroptical properties of these nanoclusters showed that $Au_{25}(Capt)_{18}$ has more pronounced chiroptical properties. Also, the CD spectra of $Au_{25}(SR)_{18}$ with different chiral ligands can serve as spectroscopic fingerprints for differentiating chiral ligand-capped Au_{25} nanoclusters.

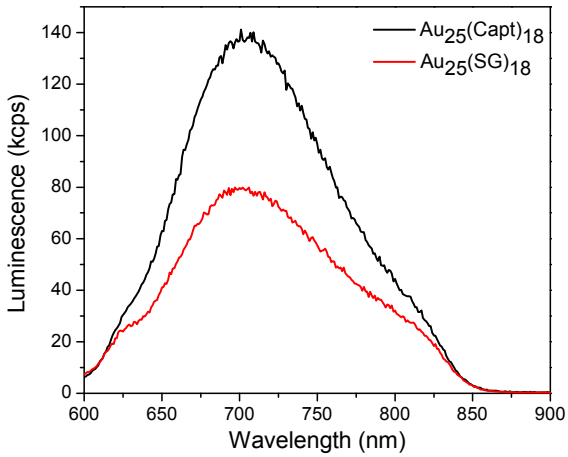

Figure 2.11 Comparison of the fluorescence spectra of $Au_{25}(Capt)_{18}$ and $Au_{25}(SG)_{18}$ (both dissolved in water, abs. (670 nm) = 0.15 OD). Excitation: 514 nm; Slit width: 5 nm. Reproduced from ref. 48 with permission. Copyright@ 2012 Royal Society of Chemistry.

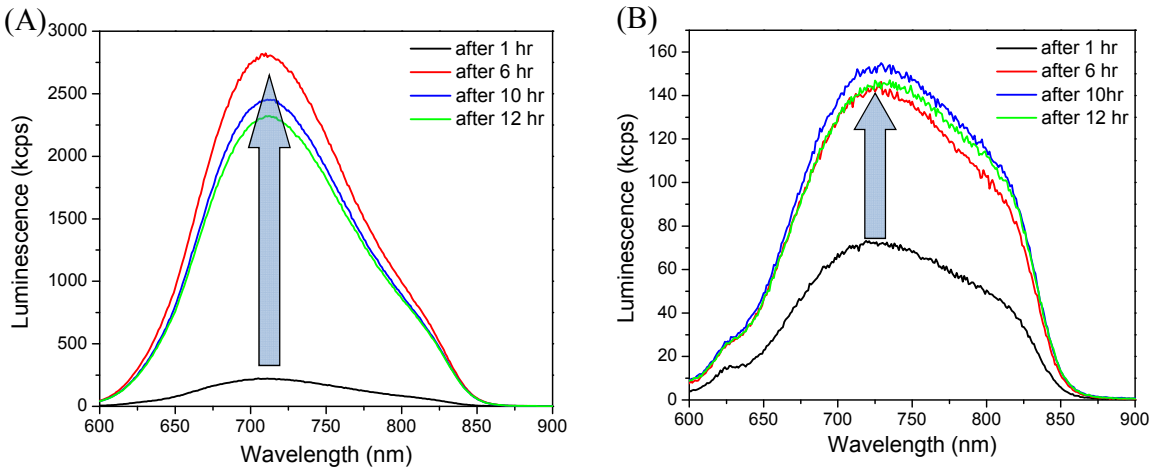

Figure 2.12 Time dependence fluorescence of **(A)** $Au_{25}(Capt)_{18}$, **(B)** $Au_{25}(SG)_{18}$, during the 12 hr heating process. Reproduced from ref. 48 with permission. Copyright@ 2012 Royal Society of Chemistry.

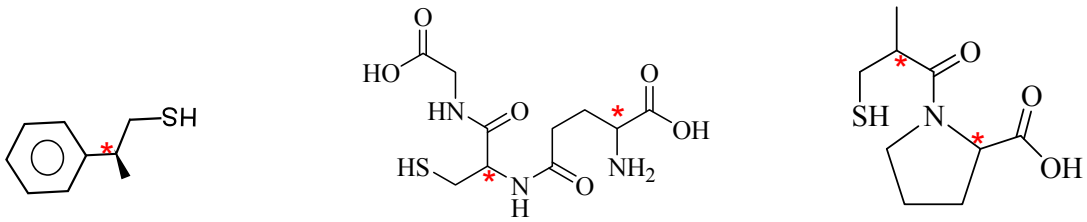

S-phenylpropane-1-thiol L-Glutathione L-Captopril

Scheme 2.2 The structure of the ligands, red star indicates the chiral center.

2.3.6 Optical absorption properties of Au_{25} nanoclusters

Noble metals (Au, Ag) nanoparticles are well characterized by their plasmonic behavior. The surface plasmon resonance (SPR) shown by these metals are well studied partly due to their strong color effect and their SPR frequency lies in the visible region of the spectrum.[51] The SPR gives an idea of the chemical environment of the nanoparticles.[52] The SPR is shown when the size of nanoparticle is between 3-100 nm and so size plays a very important role in the SPR of nanoparticles.[53] If the size of nanoparticle goes below 3 nm then the SPR is absent and molecule like behavior becomes dominant and the spectra for those size regimes depicts electronic transition. The nanoparticles with a size around 1~2 nm shows this discrete electronic transition clearly in their spectral behavior. Due to the presence of a few dozen atoms, they behave like a molecule or cluster of atoms and so called super atoms as they show properties like atom of an element. In this work, we have demonstrated the distinct optical behavior of cluster $Au_{25}SR_{18}$

which greatly differs from the bulk gold and the bigger nanoparticle capped with various thiols. So this work highlights the distinct optical absorption properties of Au_{25} nanoclusters and compares it with the reported plasmonic gold nanoparticle system.[49]

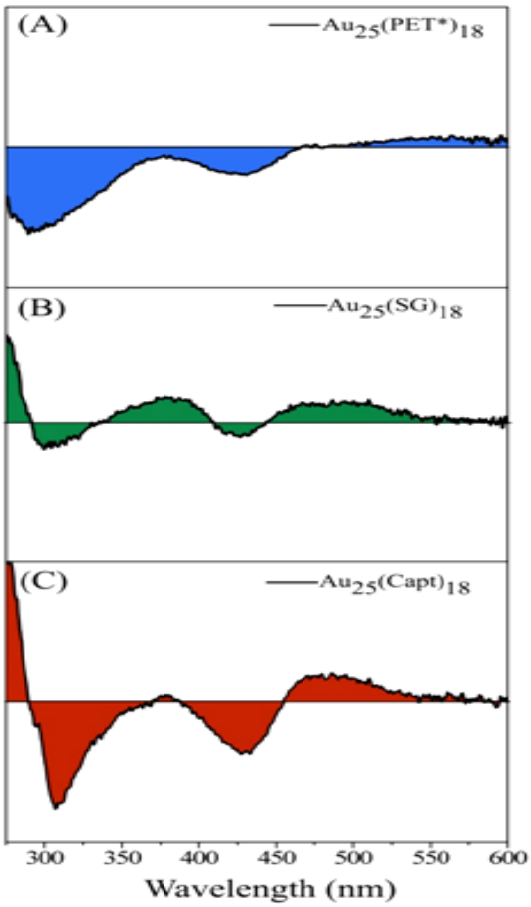

Figure 2.13 CD spectra of chiral ligand-modified Au_{25} nanoclusters. Reproduced from ref. 48 with permission. Copyright@ 2012 Royal Society of Chemistry.

Firstly, we compared the optical absorption of $Au_{25}SG_{18}$ and Au colloid of 6 nm diameter both in the solution phase. The 6-nm Au nanoparticles show a distinct SPR peak at ~520 nm (figure 2.14 black profile). In contrast, glutathione-capped $Au_{25}(SG)_{18}$ nanoclusters do not show such a SPR band; instead, multiple peaks are observed at 400, 450 and 680 nm in the UV-vis spectrum (Figure 2.14, red profile).

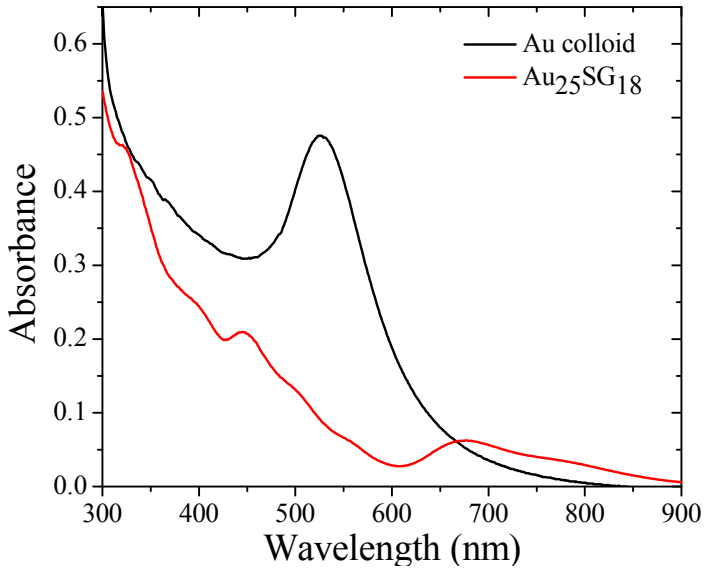

Figure 2.14 UV-Vis spectra of Au_{25} capped with glutathione and plasmonic Au nanoparticle. Reproduced from ref. 49 with permission. Copyright@ 2012 Simplex academic publisher.

According to theoretical simulations, the lowest energy band at ~680 nm is attributed to the HOMO-LUMO transition (Scheme 3), which is of single electron transition in nature, as opposed to collective-electron excitation in plasmonic Au nanocrystals. The other two peaks at 400 and 450 nm are also attributed to discrete electronic transitions (Scheme 3). The optical excitations in $Au_{25}(SR)_{18}$ nanoclusters involve molecular-like one-electron transitions; no collective SPR excitations were observed in Au_{25} nanoclusters. This optical behavior of $Au_{25}(SR)_{18}$ is in stark contrast with conventional Au nanoparticles. The distinctive optical absorption of Au_{25} nanoclusters originates from the quantum confinement effect due to the extremely Au core (1 nm), which leads to a quantized *sp* band (Scheme 3), in contrast with the quasicontinuous *sp* conduction band in plasmonic Au nanoparticles.

2.3.6.1 Effect of capping ligand

We then investigated the effect of capping ligands on the optical absorption of Au_{25} nanoclusters. For conventional plasmonic nanoparticles, the passivating ligands were found to cause red- or blue-shift in the optical spectra.[54] To investigate whether nanoclusters showed such an effect, we synthesized Au_{25} nanoclusters using three different thiol ligands, including phenylethanethiol (abbreviated as PET), glutathione (GSH), and captopril (Capt). The Au_{25} nanoclusters capped with glutathione and captopril were dissolved in water and the phenylethanethiolate-capped Au_{25}

was dissolved in toluene. We found that the ligands do not affect the optical absorption spectrum (i.e. no red- or blue-shift of peaks occurring in nanoclusters) (Figure 2.15). This indicates another important difference between nanoclusters and plasmonic nanoparticles, that is, the one-electron transitions in $Au_{25}(SR)_{18}$ nanoclusters (Scheme 3) are not sensitive to the type of thiolate ligands. The observation in nanoclusters that the optical spectral properties do not change with the ligand shell is quite remarkable as compared to plasmonic nanoparticles.

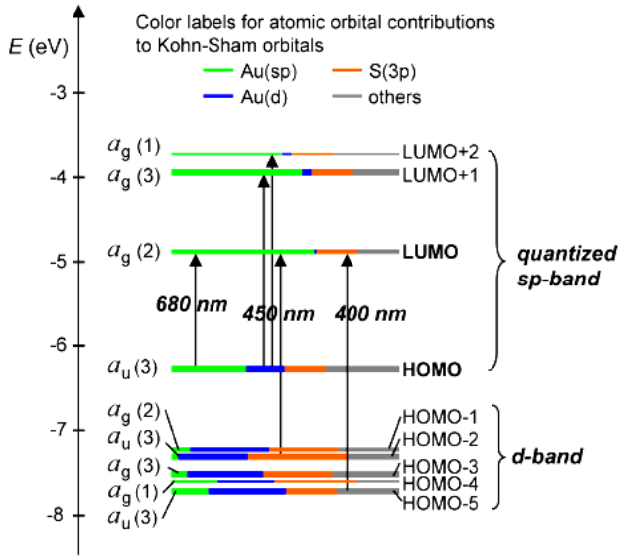

Scheme 2.3. Quantized electron energy levels in $Au_{25}(SR)_{18}$ nanoclusters. The different colors indicate the atomic orbital contributions to the Kohn-Sham orbitals, and the line thickness indicates the orbital degeneracy (such as the triply degenerate HOMO orbital *a* u(3)). Reproduced from ref. 49 with permission. Copyright@ 2012 Simplex academic publisher.

2.3.6.2 Effect of physical states

Another effect of potential interest pertains to the influence of physical environments on the optical properties of Au_{25} nanoclusters. For plasmonic nanoparticles, it is well known that the substrate (e.g. glass, on which nanoparticles are deposited) or the physical state (e.g. solid vs solution of nanoparticles) strongly affects the spectra of metal nanoparticles. Generally, the plasmon peak broadens as the physical state is changed from solution to the solid state due to plasmon coupling when nanoparticles are brought closer in the solid state. In the case of plasmonic nanoparticles deposited on substrates, the shift in SPR position may also be caused by

the change in dielectric constant.[55,56] Interestingly, for nanoclusters, we found that the spectral features for all the three types of dried $Au_{25}(SR)_{18}$ nanoclusters deposited on quartz substrates exhibit similar optical absorption features as in the solution phase This is in sharp contrast to the behavior of plasmonic metal nanoparticles on substrates. Thus, our results show that the optical transitions in Au_{25} nanoclusters are not sensitive to the physical environment (figure 2.16)

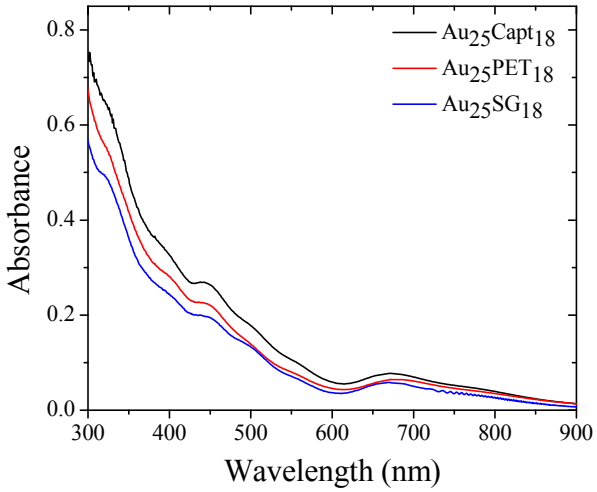

Figure 2.15 Au_{25} capped with captopril, phenyl ethane thiol, and glutathione. The spectra have been slightly offset for clarity. Reproduced from ref. 49 with permission. Copyright@ 2012 Simplex academic publisher.

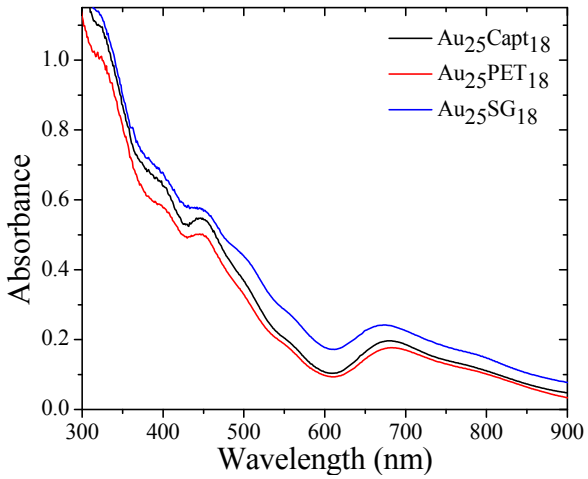

Figure 2.16 Au_{25} capped with different ligand on quartz substrate. The spectra have been offset for clarity. Copyright@ 2012 Simplex academic publisher.

2.3.6.3 Effect of dielectric constants of solvents

Since the Au_{25} spectra did not show any shift in peak position between the solution and solid states, it indicates that the dielectric constant (ε) of the medium does not affect the spectral properties of these quantum-sized nanoclusters. To further investigate the effect of dielectric constant on the optical absorption of Au_{25} nanoclusters, we studied the spectra of $Au_{25}(PET)_{18}$ nanoclusters in various solvents that have different dielectric constants and chemical environments. Table 1 lists the organic solvents investigated in this work and their respective dielectric constants ($\varepsilon = n^2$, where n = refractive index) at optical frequencies. For plasmonic nanoparticles, the SPR wavelength red shifts with increasing n and the sensitivity is typically about 100 nm (i.e. SPR peak wavelength shift) per unit of refractive index (n) for spherical nanoparticles,[57] and non-spherical nanoparticles can be even more sensitive.[56] In contrast, our results show that the $Au_{25}(PET)_{18}$ nanocluster solution did not show any discernible shift in their peak wavelengths with different solvents (figure 2.17). This is again a distinct feature compared to the behavior of plasmonic nanoparticles.

Solvents	Dielectric constant
Acetonitrile (MeCN)	37.5
Dichloromethane (DCM)	9.1
Tetrahydrofuran (THF)	7.5
Toluene	2.3

Table 2.1 Solvents and their dielectric constants

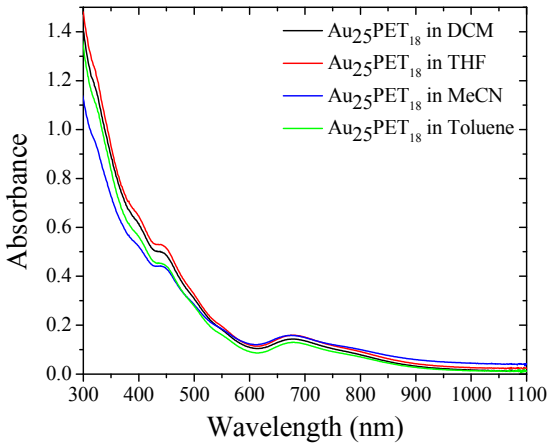

Figure 2.17 $Au_{25}(PET)_{18}$ in different solvents. The spectra have been slightly offset for clarity. Copyright@ 2012 Simplex academic publisher.

2.3.6.4 Effect of nanoclusters assembly

We also investigated the effect of Au_{25} nanocluster linked together by bi-linkers on the optical absorption property. For plasmonic nanoparticle solutions, the addition of bi-linker molecules typically leads to a large red-shift in the SPR peak.[58,59] For closely spaced nanoparticles, a new plasmon mode may also appear at longer wavelength due to strong plasmon coupling.[60] To link Au_{25} nanoclusters together, we added a dithiol, bis-biphenyl-4,4`-dithiol, to a Au_{25} $(PET)_{18}$ solution at a ratio of averagely ~6 dithiol molecules per $Au_{25}(PET)_{18}$ cluster.

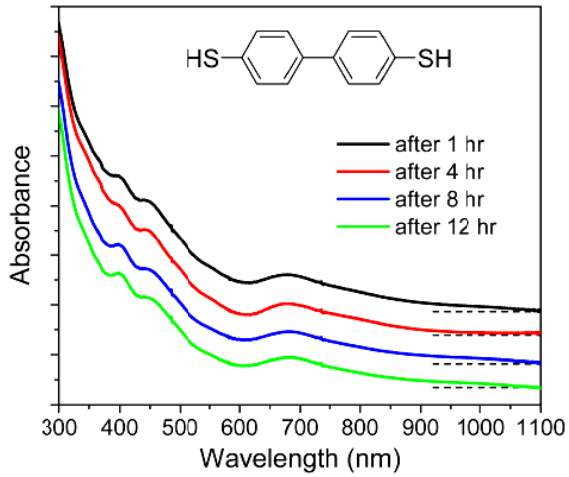

Figure 2.18 Effect of Linking Au_{25} nanoclusters on their optical properties. Copyright@ 2012 Simplex academic publisher.

The addition of excess thiol was to ensure that each cluster is linked with multiple dithiol molecules. Interestingly, no spectral change was observed before/after linking nanoclusters together (even after ~12 hr), Figure 2.18. This result indicates that unlike plasmonic nanoparticles, linking Au_{25} nanoclusters together does not influence their optical absorption behavior. This is due to the absence of near-field for nanoclusters, while the near field is quite strong for plasmonic nanoparticles and, when two plasmonic nanoparticles are brought together, near-field coupling occurs, leading to plasmon coupling or the creation of new plasmon mode.[60]

2.4 Summary

In conclusion, we have prepared highly robust water-soluble $Au_{25}(Capt)_{18}$ nanoclusters. The UV-Vis, PAGE analysis, TGA, MALDI and ESI-mass spectrometry has been utilized to demonstrate its purity. The thermal stability study revealed the extraordinary stability of $Au_{25}(Capt)_{18}$ over

$Au_{25}(SG)_{18}$ nanoclusters. The high stability of $Au_{25}(Capt)_{18}$ clusters has been explained by the ligand stability of Captopril over Glutathione. Photoluminescence study showed that $Au_{25}(Capt)_{18}$ nanoclusters have high fluorescence than glutathione or aromatic thiols capped Au_{25} nanoclusters reported before. The thermal study revealed that the fluorescence enhancement of ~20 times can be achieved for $Au_{25}(Capt)_{18}$ by heating the nanocluster solution. The chiral ligand does induce chirality to the overall cluster. $Au_{25}(Capt)_{18}$ captopril showed enhanced chiroptical properties than the other reported nanoclusters. CD spectra of various chiral ligand capped $Au_{25}(SR)_{18}$ can serve as fingerprint for the detection of nanoclusters.

Also, the optical absorption study of Au_{25} nanoclusters and its comparison with plasmonic nanoparticles revealed that the nanocluster system shows fundamentally distinct optical properties than their larger counterpart-plasmonic nanoparticles. The absorption spectra of Au_{25} nanoclusters showed no effect of capping ligand, physical state, and dielectric environment which has a significant effect on the plasmonic nanoparticles. The distinct optical absorption of these nanocluster systems has been explained by the discrete energy level transition as compared to the quasi-continuous band in case of plasmonic nanoparticles.

2.5 References

1) Jin, R.; Zhu, Y.; Qian, H. *Chem.-Eur. J.* **2011**, *17*, 6584-6593.
2) Parker, J. F.; Fields-Zinna, C. A.; Murray, R. W. *Acc.Chem. Res.* **2010**, *43*, 1289-1296.
3) Tsukuda, T. B. *Chem. Soc. Jpn.* **2012**, *85*, 151-168.
4) George, A.; Shibu, E.; Maliyekkal, S. M.; Bootharaju, M.; Pradeep, T. *ACS App. Mater. Inter.* **2012**, *4*, 639-644.
5) Price, R. C.; Whetten, R. L. *J. Am. Chem. Soc.* **2005**, *127*, 13750-13751.
6) Qian, H.; Zhu, Y.; Jin, R. P. *Natl. Acad. Sci.* **2012**, *109*, 696-700.
7) Dass, A. *J. Am. Chem. Soc.* **2011**, *133*, 19259-19261.
8) Pei, Y.; Pal, R.; Liu, C.; Gao, Y.; Zhang, Z.; Zeng, X. C. A. *J. Am. Chem. Soc.* **2012**, *134*, 3015-3024.
9) Noguez, C.; Garzón, I. L. *Chem. Soc. Rev.* **2009**, *38*, 757-771.
10) Jin, R. *Nanoscale* **2010**, *2*, 343-362.
11) Negishi, Y.; Chaki, N. K.; Shichibu, Y.; Whetten, R. L.; Tsukuda, T. A. *J. Am. Chem. Soc.* **2007**, *129*, 11322-11323.
12) Schaaff, T. G.; Whetten, R. L. *J. Phys. Chem. B* **2000**, *104*, 2630-2641.
13) Gautier, C.; Bürgi, T. *Chem. Phys. Chem.* **2009**, *10*, 483-492.
14) Yao, H. *Current Nanoscience* **2008**, *4*, 92-97.
15) Zhu, M.; Qian, H.; Meng, X.; Jin, S.; Wu, Z.; Jin, R. *Nano Lett.* **2011**, *11*, 3963-3969.
16) Qian, H.; Eckenhoff, W. T.; Zhu, Y.; Pintauer, T.; Jin, R. A. *J. Am. Chem. Soc.* **2010**, *132*, 8280-8281.
17) Tlahuice, A.; Garzón, I. L. *Phys. Chem. Chem. Phys.* **2012**, *14*, 3737-3740.
18) Qian, H.; Zhu, M.; Gayathri, C.; Gil, R. R.; Jin, R. *ACS Nano* **2011**, *5*, 8935-8942.
19) Zhu, M.; Aikens, C. M.; Hendrich, M. P.; Gupta, R.; Qian, H.; Schatz, G. C.; Jin, R. A. *J. Am. Chem. Soc.* **2009**, *131*, 2490-2492.
20) Negishi, Y.; Tsunoyama, H.; Suzuki, M.; Kawamura, N.; Matsushita, M. M.; Maruyama, K.; Sugawara, T.; Yokoyama, T.; Tsukuda, T. A. *J. Am. Chem. Soc.* **2006**, *128*, 12034-12035.
21) Jiang, D. E.; Whetten, R. L. *Phys. Rev.B* **2009**, *80*, 115402.
22) Venzo, A.; Antonello, S.; Gascón, J. A.; Guryanov, I.; Leapman, R. D.; Perera, N. V.; Sousa, A.; Zamuner, M.; Zanella, A.; Maran, F. *Anal. Chem.* **2011**, *83*, 6355-6362.

23) Liu, Z.; Zhu, M.; Meng, X.; Xu, G.; Jin, R. *J. Phys. Chem. Lett.* **2011**, *2*, 2104-2109.
24) Liu, Y.; Tsunoyama, H.; Akita, T.; Tsukuda, T. *Chem. Commun.* **2010**, *46*, 550-552.
25) Zhu, Y.; Qian, H.; Drake, B. A.; Jin, R. *Angew. Chem. Int. Ed.* **2010**, *49*, 1295-1298.
26) Zhu, Y.; Qian, H.; Zhu, M.; Jin, R. *Adv. Mater.* **2010**, *22*, 1915-1920.
27) Wu, X.; He, X.; Wang, K.; Xie, C.; Zhou, B.; Qing, Z. *Nanoscale* **2010**, *2*, 2244-2249.
28) Retnakumari, A.; Setua, S.; Menon, D.; Ravindran, P.; Muhammed, H.; Pradeep, T.; Nair, S.; Koyakutty, M. *Nanotechnology* **2010**, *21*, 055103.
29) Liu, C. L.; Wu, H. T.; Hsiao, Y. H.; Lai, C. W.; Shih, C. W.; Peng, Y. K.; Tang, K. C.; Chang, H. W.; Chien, Y. C.; Hsiao, J. K. *Angew. Chem. Int. Ed.* **2011**, *50*, 7056-7060.
30) Jin, R.; Qian, H.; Wu, Z.; Zhu, Y.; Zhu, M.; Mohanty, A.; Garg, N. *J. Phys. Chem. Lett.* **2010**, *1*, 2903-2910.
31) Wyrwas, R.; Alvarez, M.; Khoury, J.; Price, R.; Schaaff, T.; Whetten, R. *Eur. Phys. J. D* **2007**, *43*, 91-95.
32) Zhu, M.; Lanni, E.; Garg, N.; Bier, M. E.; Jin, R. *J. Am. Chem. Soc.* **2008**, *130*, 1138-1139.
33) Wu, Z.; Suhan, J.; Jin, R. *J. Mater. Chem.* **2009**, *19*, 622-626.
34) Negishi, Y.; Kurashige, W.; Kamimura, U. *Langmuir* **2011**, *27*, 12289-12292.
35) Qian, H.; Zhu, Y.; Jin, R. *ACS Nano* **2009**, *3*, 3795-3803.
36) Schaaff, T. G.; Shafigullin, M. N.; Khoury, J. T.; Vezmar, I.; Whetten, R. L. *J. Phys. Chem. B* **2001**, *105*, 8785-8796.
37) Negishi, Y.; Nobusada, K.; Tsukuda, T. *J. Am. Chem. Soc.* **2005**, *127*, 5261-5270.
38) Ackerson, C. J.; Jadzinsky, P. D.; Kornberg, R. D. *J. Am. Chem. Soc.* **2005**, *127*, 6550-6551.
39) Qian, H.; Zhu, Y.; Jin, R. *J. Am. Chem. Soc.* **2010**, *132*, 4583-4585.
40) Zhu, M.; Qian, H.; Jin, R. *J. Am. Chem. Soc.* **2009**, *131*, 7220-7221.
41) Zhu, M.; Qian, H.; Jin, R. *J. Phys. Chem. Lett.* **2010**, *1*, 1003-1007.
42) Nimmala, P. R.; Dass, A. *J. Am. Chem. Soc.* **2011**, *133*, 9175-9177.
43) Zeng, C.; Qian, H.; Li, T.; Li, G.; Rosi, N. L.; Yoon, B.; Barnett, R. N.; Whetten, R. L.; Landman, U.; Jin, R. *Angew. Chem.* **2012**, *124*, 13291-13295.
44) Heaven, M. W.; Dass, A.; White, P. S.; Holt, K. M.; Murray, R. W. *J. Am. Chem. Soc.* **2008**, *130*, 3754-3755.

45) Zhu, M.; Aikens, C. M.; Hollander, F. J.; Schatz, G. C.; Jin, R. *J. Am. Chem. Soc.* **2008**, *130*, 5883-5885.
46) Shichibu, Y.; Negishi, Y.; Tsukuda, T.; Teranishi, T. *J. Am. Chem. Soc.* **2005**, *127*, 13464-13465.
47) Cathcart, N.; Kitaev, V. *J. Phys. Chem. C* **2010**, *114*, 16010-16017.
48) Kumar, S.; Jin, R. *Nanoscale* **2012**, *4*, 4222-4227.
49) Santosh Kumar, R. J. *J. Nanoscience Lett.* **2013**, *3*, 5.
50) Wu, Z.; Jin, R. *Nano letters* **2010**, *10*, 2568-2573.
51) Ghosh, S. K.; Pal, T. *Chem. Rev.* **2007**, *107*, 4797-4862.
52) Rampi, M. A.; Schueller, O. J.; Whitesides, G. M. *Appl. Phys. Lett.* **1998**, *72*, 1781-1783.
53) Heath, J. *Phys. Rev.B* **1989**, *40*, 9982.
54) Ghosh, S. K.; Nath, S.; Kundu, S.; Esumi, K.; Pal, T. *J. Phys. Chem. B* **2004**, *108*, 13963-13971.
55) Yamaguchi, T.; Yoshida, S.; Kinbara, A. *Thin Solid Films* **1974**, **21**, 173-187.
56) Duval Malinsky, M.; Kelly, K. L.; Schatz, G. C.; Van Duyne, R. P. *J. Phys. Chem. B* **2001**, *105*, 2343-2350.
57) Underwood, S.; Mulvaney, P. *Langmuir* **1994**, *10*, 3427-3430.
58) Quinten, M.; Kreibig, U. *Surf. Sci.* **1986**, *172*, 557-577.
59) Thomas, K. G.; Zajicek, J.; Kamat, P. V. *Langmuir* **2002**, *18*, 3722-3727.
60) Chen, G.; Wang, Y.; Tan, L. H.; Yang, M.; Tan, L. S.; Chen, Y.; Chen, H. *J. Am. Chem. Soc.* **2009**, *131*, 4218-4219.

Chapter 3

Large-scale Enantioselective Synthesis of Chiral Au_{38} and Au_{40} Nanoclusters

3.1 Introduction

Ever since chirality was described in early 19th century, it has continued to garner a lot of interest in diverse areas of scientific research, including the more recent field of nanotechnology. Indeed, special types of macromolecules like DNA and metal nanoparticles exhibit this intriguing feature, which in turn has been shown to have direct effect on catalysis, medicine and a variety of applications.[1] In this direction, major advances in the synthesis of colloidal nanoparticles in recent years has enabled widespread exploration of chirality in nanostructures. For example, chiral nanoparticles have shown promise in potential applications,[1] like chiral catalysis,[2-4] chiroptics (e.g. negative refractive index materials),[5,6] chiral separation of analytical and biological molecules,[7] and chiral recognition and sensor design.[8,9]

In the past, several strategies have been employed to achieve chiral nanostructures. These include i) direct synthesis in the presence of chiral ligands or chiral surfactants,[10] ii) post-synthetic modification of achiral nanoparticles by chiral stabilizers,[4] iii) chiral assembly of nanoparticles in the presence of chiral templates[11] or even without template.[12] In this regard, various chiral stabilizers have been used, most significant of them being chiral thiols (for e.g. L-glutathione, L- or D-cysteine) and inherently chiral biomolecules like DNA and peptides.[13-18] Many types of optical active nanoparticles have been reported utilizing such strategies; noteworthy examples include chiral Au nanospheres and nanorods, chirally assembled Au nanosphere and nanorods, chiral Ag nanoparticles, and even chiral semiconductor quantum dots.[4-6,10,11,17] The key feature in such chiral metal nanoparticles is essentially the circular dichroism (CD) response which emerges in the metal-based optical absorption region such as the vicinity of surface plasmon resonance (SPR) and typically lies beyond the region of the ligand itself (usually in the UV region). With respect to the CD signal of the ligand, it is often enhanced by the plasmon of metal nanoparticles and scales as the plasmon intensity.

In view of these interesting properties, an interesting question of chiral nanoparticles pertains to the origin of the optical activity, including both chiral surface plasmon resonance (SPR) observed in metal nanoparticles > 2 nm in size and the chiroptical response in *non-plasmonic* ultrasmall nanoparticles (i.e. nanoclusters). Several mechanisms have been advocated in previous reports; however, these mechanisms are still being debated. In general, for plasmonic nanoparticles, the CD response in the vicinity of the plasmon frequency is attributed to the surface molecule induced chiral currents in the nanoparticles.[19] Meanwhile, for *non-plasmonic* nanoclusters three different mechanisms have been proposed,[13] i) chiral metal core,[20] ii) chiral adsorption pattern (or a related model called chiral footprint model),[16] and iii) chiral induction or vicinal effect (i.e. electronic induction by chiral molecules).[21] It is well-established that chiral molecules on the particle surface can impart chirality to nanoparticles, thereby inducing chiroptical response from the particle. This feature is evident in plasmonic or excitonic CD responses in the visible to near IR wavelengths.

Prominent examples include the CD responses at ~400 nm for Ag nanoparticles, at ~520 nm for gold nanoparticles, and multiple CD peaks for nanoclusters due to quantized electronic structure. In addition, Tang and coworkers observed unique bi signated CD bands around the longitudinal SPR of Au nanorods through 1D end-to-end assembly of cysteine end-functionalized gold nanorods, and the optical activity was attributed to the collective tip-enhanced electromagnetic field in the 1D assembly of nanorods.[22] Inherently chiral $Au_{38}(SCH_2CH_2Ph)_{24}$ nanoclusters have also been reported. Further, separation of the (±)-Au_{38} and (±)-Au_{40} enantiomers was achieved very recently by chiral high-performance liquid chromatography (HPLC).[23,24] In this regard, a key question which arises is whether selective synthesis of enantiomers can be achieved in one step, that is, to form one enantiomer against the other, which is often critical for practical applications of such non-plasmonic chiral nanoparticles.

In order to address this issue, we attempted the enantioselective synthesis of different ligand-protected Au_{38} nanoclusters by a direct approach using chiral ligands including (*R*) and (*S*)-2-phenylpropane-1-thiol (abbreviated as *R*- and *S*-PET, or collectively as PET*), (*2S*)-1-[(*2S*)-2-methyl-3-sulfanylpropanoyl] pyrrolidine-2-carboxylic acid (commercial name: Captopril, abbreviated as Capt), and L-glutathione(GSH) and Au_{40} capped with Captopril. To this end, we successfully achieved the synthesis of Au_{38} nanoclusters protected by all of aforementioned ligands. Further in order to confirm the chiral nature of these clusters, their anisotropy factors

(ΔA/A) were measured and found to be comparable to that of the reported pure $Au_{38}(SCH_2CH_2Ph)_{24}$ enantiomers separated by chiral HPLC.[23]

3.2 Experimental

3.2.1 Synthesis of $Au_{38}(PET^*)_{24}$

In a typical synthesis, $HAuCl_4 \cdot 3H_2O$ (0.1612 g, 0.41 mmol) was dissolved in 5 mL Nanopure water, and tetraoctylammonium bromide (TOAB, 0.2596 g, 0.47 mmol) was dissolved in 10 mL toluene. The two solutions were combined in a 25 mL tri-neck round bottom flask. The solution was vigorously stirred (~1100 rpm) with a magnetic stir bar to facilitate phase transfer of Au (III) salt into the toluene phase. After ~15 min, phase transfer was completed, leaving a clear aqueous phase at the bottom of the flask; the aqueous layer was then removed using a 10 mL syringe. The toluene solution of Au (III) was cooled to 0 °C in an ice bath over a period of 30 min under magnetic stirring. After stirring was reduced to a very low speed (~50 rpm), (*R*)- or (*S*)-2-phenylpropane-1-thiol (0.17 mL, ~3 equivalents of the moles of gold) was added. The solution was kept stirring after thiol addition, during which the solution color slowly changed from deep red to faint yellow, then gradually phased out and eventually became clear over a ~1 h period. After the solution turned clear, the stirring speed was increased to ~1100 rpm. 10 mL of aqueous solution of $NaBH_4$ (0.1561 g, 4 mmol, 10 equivalents per mole of gold, freshly made in 10 mL ice-cold Nanopure water) was rapidly added to the solution all at once. The reaction was allowed to proceed for ~20 hours. After that, the black toluene phase was dried by rotary evaporation at room temperature and ethanol was added to separate the Au nanoclusters from TOAB and other side products. Acetonitrile was added to extract the Au_{25} clusters impurity from the black mixture, and the remaining black solid was polydisperse gold nanoclusters. The black solid obtained in the first step (about 20 mg) was dissolved in 20mL toluene. 1.0 mL (*R*)- or (*S*)-2-phenylpropane-1-thiol was added to the solution. The solution was then heated to 80 ^oC and maintained at 80 ^oC for about 12 hours under constant magnetic stirring. After that, 20 mL methanol was added to the solution to precipitate Au nanoparticles. Au_{38} nanoparticles and Au(I)-SR exist in the black precipitation. Since Au(I)-SR is poorly soluble in any organic solvents, Au_{38} can be extracted with toluene and CH_2Cl_2.

3.2.2 Synthesis of $Au_{38}(Capt)_{24}$

The synthesis of $Au_{38}(Capt)_{24}$ was done at room temperature under air. $HAuCl_4 \cdot 3H_2O$ (0.20 mmol, 78.7 mg) and TOABr (0.23 mmol, 126.8 mg) were first dissolved in 15 ml methanol and vigorously stirred (1200 rpm). The solution color changed from yellow-orange to deep red. After 15 min, captopril (0.6 mmol, 130 mg) was added into the reaction mixture under stirring. The solution color quickly changed to white. After 30 min, the stirring speed was reduced to 600 rpm and $NaBH_4$ (1mmol, 37.8 mg, dissolved in 5 ml of ice cold water) was rapidly added to the reaction mixture. The solution color immediately turned brown-green. The reaction was allowed to proceed for 48 h and the reaction was monitored continuously through UV-Vis spectroscopy. After 48 h, the spectral feature was clearly like Au_{38} as shown in figure 3.1. The reaction mixture was then centrifuged to remove unreacted, insoluble Au(I):SR polymers. The supernatant was collected and concentrated in vacuo. The clusters were precipitated by adding acetone to the solution. The precipitate was extracted with minimum amounts of methanol several times and precipitated with acetone. The clean precipitate was finally dried under vacuum.

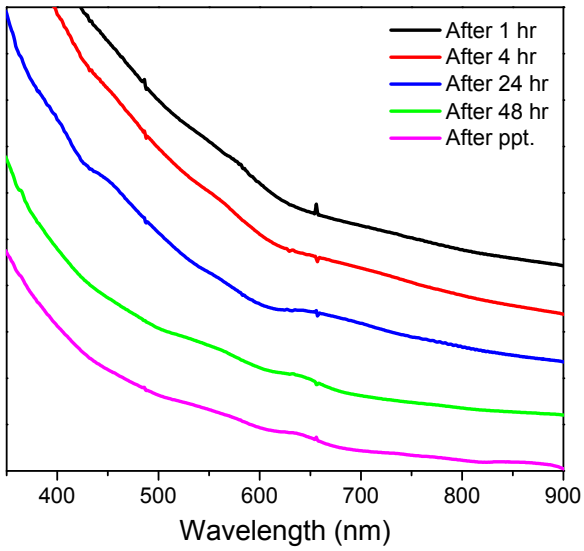

Figure 3.1 Time evolution of the synthesis process of $Au_{38}(Capt)_{24}$ (spectra has been offset for clarity).

3.2.3 Synthesis of $Au_{38}(SG)_{24}$

The synthesis of $Au_{38}SG_{24}$ was done in two steps. First the polydisperse $Au_n(SG)_m$ clusters were prepared by previously reported protocol.[25] This mixture was then etched with excess of

glutathione at 55 °C in water.[26] The etched product was then centrifuged to remove insoluble Au(I):SR polymer and the supernatant was precipitated with ethanol. The precipitate was washed several times, ultrasonicated and centrifuged to obtain the clean product. The etched product was run through the PAGE gel with 30 % monomer concentration for 16 hr at 200 V. $Au_{38}(SG)_{24}$ appears as well separated band (figure. 3.2). The pure $Au_{38}(SG)_{24}$ clusters was then cut from the gel and soaked in water for 2 h and then filtered with 0.2 µm filter. The filtered solution was then concentrated with a cut-off filter of 3 kDa. The concentrated solution was then precipitated with ethanol and then dried in vacuum.

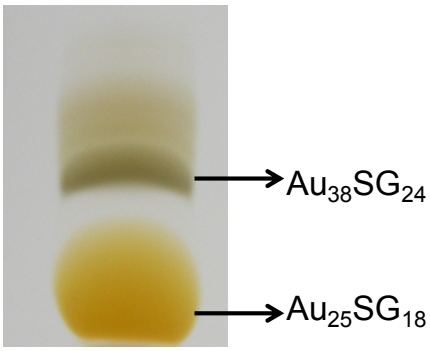

Figure 3.2 PAGE image of the etched $Au_n(SG)_m$ nanoclusters.

3.2.4 Synthesis of $Au_{40}(Capt)_{24}$

The synthesis of $Au_{40}(Capt)_{24}$ was done in one pot. In the synthesis of $Au_{38}(Capt)_{24}$ process, if the reaction is aged for 24-30 hr and the product is isolated, it generates $Au_{40}(Capt)_{24}$ along with $Au_{38}(Capt)_{24}$. This is quite similar to the work of Qian *et al.* where the $Au_{40}(PET)_{24}$ nanoclusters was isolated by stopping the thiol etching process at 18 hr instead of 48 hr.[27] The Au_{40} nanoclusters were isolated by running the gel and isolating the Au_{40} fraction (as shown in figure 3.3) by the regular protocol for isolation of nanoclusters from the gel.

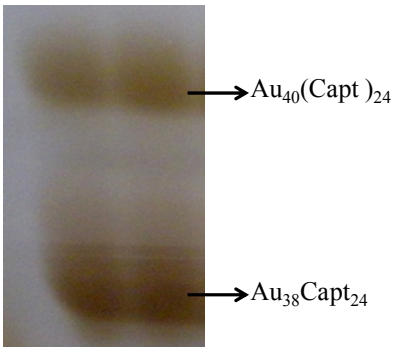

Figure 3.3 PAGE image of the isolated $Au_{40}(Capt)_{24}$ nanoclusters.

3.2.5 Characterization

The UV-vis absorption spectra (190-1100 nm range) of the cluster were recorded in CH_2Cl_2 (for organic soluble Au_{38}) and water (for aqueous soluble Au_{38}) at room temperature using a Hewlett-Packard (HP) 8453 diode array spectrophotometer. The UV-vis-NIR spectra (190-2000 nm range) were recorded on a Varian Cary 5000 vis-NIR spectrophotometer at room temperature. Electrospray ionization (ESI) mass spectra were recorded using a Waters Q-TOF mass spectrometer equipped with a Z spray source. Water soluble $Au_{38}(Capt)_{24}$ was dissolved in 50 % water/methanol and injected at a flow rate of 5 μL/min. For $Au_{38}(PET^*)_{24}$, a solution of CsOAc salt (50 mM in dry methanol) was added to form Cs^+ adducts of nanoclusters (dissolved in toluene or CH_2Cl_2, ~1 mg/mL) during the ESI process, and the positively charged adducts were then detected by ESI-MS. Circular dichroism (CD) spectra of the clusters were recorded in CH_2Cl_2 (for organic soluble Au_{38}) and in water (for aqueous soluble Au_{38}) at room temperature on a JASCO J-810 CD spectrometer. Thermal gravimetric analysis (TGA) was performed on a TG/DTA6300 analyzer (Seiko Instruments, Inc.) under a N_2 atmosphere (flow rate ~50 mL/min).

3.3 Results and Discussion

3.3.1 Synthesis of $Au_{38}(PET^*)_{24}$

Our synthetic strategy to obtain chiral Au_{38} nanoclusters capped with *R*- and *S*-PET is different from that employed for obtaining racemic $Au_{38}(SCH_2CH_2Ph)_{24}$.[28] In a previous work,[28] a two-phase method for synthesis of Au_{38} nanoclusters was proposed. Here, the first step involved the synthesis of water-soluble polydisperse glutathione-capped $Au_n(SG)_m$ clusters followed by ligand exchange with excess $HSCH_2CH_2Ph$. Hence, this process involves phase transfer from water to organic phase, followed by size focusing of polydisperse $Au_n(SCH_2CH_2Ph)_m$ into molecularly pure $Au_{38}(SCH_2CH_2Ph)_{24}$. However, this method failed to yield the direct synthesis of chiral Au_{38}. Therefore, we developed a new one-phase protocol to achieve enantioselective synthesis. In this method, we synthesized polydisperse $Au_n(PET^*)_m$ clusters, where PET refers to either (*R*)-PET* or (*S*)-PET*, in the first step in lieu of water soluble glutathione in previous work. The second step involved the conversion of the polydisperse $Au_n(PET^*)_m$ clusters to molecular purity $Au_{38}(PET^*)_{24}$ product in presence of excess chiral thiol at ~80 ^oC. Chiral $Au_{38}(PET^*)_{24}$ nanoclusters were separated from the side product (i.e. Au(I)-PET* complexes, which are less soluble in most solvents) by extracting it with toluene or CH_2Cl_2. In the new one-

phase synthesis, the synthetic conditions for the (*R*)-PET* and (*S*)-PET* capped chiral Au_{38} nanoclusters are the same.

Although their optical absorption spectra are identical, the as-prepared Au_{38} clusters (denoted as (*R*)-Au_{38} and (*S*)-Au_{38}) show mirror-imaged CD spectra, as illustrated in figure 3.4 A and B. These nanoclusters are non-plasmonic, evidenced by the absence of the typical SPR band of gold nanoparticles; indeed, their absorption spectra are superimposable with the pure, racemic $Au_{38}(SCH_2CH_2Ph)_{24}$ nanoclusters.[29]

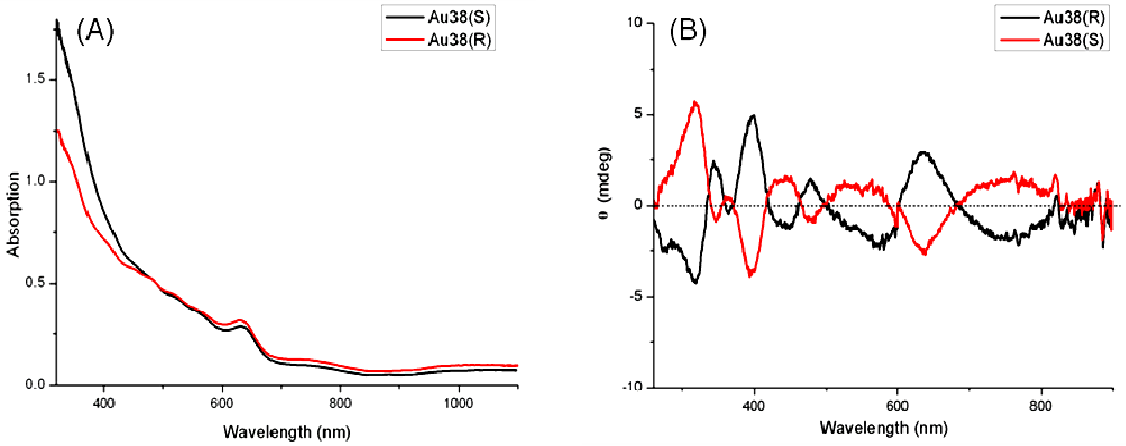

Figure 3.4 (A) UV-vis absorption of (*R*-) and (*S*-) Au_{38} nanoclusters. (B) Circular dichroism (CD) spectra of the (*R*-) and (*S*-) Au_{38} nanoclusters.

To further confirm that the as-prepared nanoclusters are pure $Au_{38}(PET^*)_{24}$, we performed electronspray ionization (ESI) mass spectrometric analysis. Since Au_{38} nanoclusters are charge-neutral, a solution of CsOAc salt was added to the cluster solution to facilitate ionization of the clusters. Using (*R*)-Au_{38} as the example, ESI-MS analysis show two major peak at *m/z* 11247.1 and 5689.9 (figure 3.5), which correspond to singly charged $[Au_{38}(PET^*)_{24}Cs]^+$ (calculated FW: 11247.3, experimental deviation: 0.2 Da) and doubly charged $[Au_{38}(PET^*)_{24}Cs_2]^{2+}$ (as revealed by the isotope peak spacing δ=0.5; calculated FW: 5690.1, experimental deviation: 0.2 Da). It is worthy to note that the low mass end (m/z < ~5000) shows several uniformly spaced $[CsOAc]_xCs^+$ m/z peaks with 192 Da spacing (corresponding to the formula weight of CsOAc). Moreover, no other species was observed, thereby confirming the high purity of the Au_{38} nanoclusters. The (*S*)-$Au_{38}(PET^*)_{24}$ clusters also exhibited as-expected mass peaks.

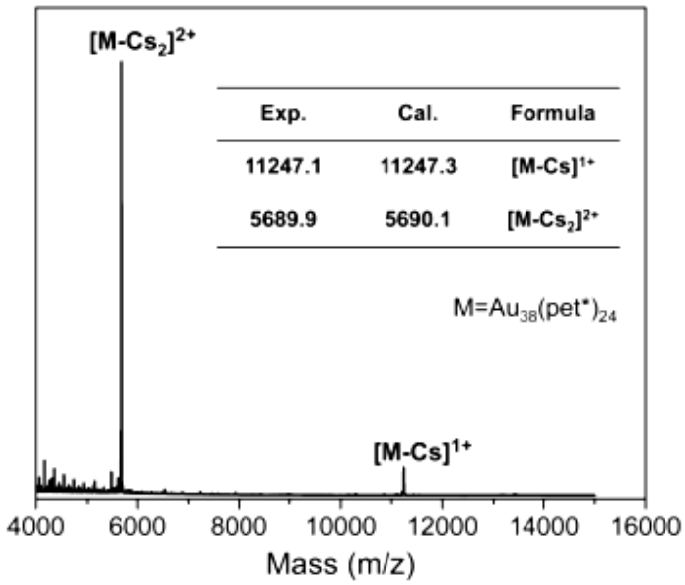

Figure 3.5 ESI mass spectrum of (*R*)-$Au_{38}(PET^*)_{24}$ nanoclusters.

3.3.2 Chiroptical properties of (*R*-) and (*S*-) $Au_{38}(PET)_{24}$ nanoclusters

The CD spectra for both (*R*)- and (*S*)-$Au_{38}(PET^*)_{24}$ display distinct CD signals (figure 3.4 B). Moreover, they exhibit a precise mirror image relationship. Four positive bands at 318 nm, 440 nm, 560 nm, 760 nm and four negative bands at 345 nm, 399 nm, 483 nm, 637 nm are observed in the CD spectra of (*S*)-$Au_{38}(PET^*)_{24}$ nanoclusters. On the other hand, the (*R*)-$Au_{38}(PET^*)_{24}$ enantiomer shows the opposite polarity peaks but at the same peak wavelengths. Of note, the CD signals at longer wavelengths (e.g. the HOMO-LUMO transition at 1050 nm) cannot be measured due to the detection limit of the CD spectrometer (<800 nm). Here, it is worthy to note that the observed CD signals are not from the thiol ligands themselves, as the chiral ligand's signals are in the UV region (<250 nm), rather than in the measured wavelength region.

In 2010, Qian *et al* determined the crystal structure of racemic $Au_{38}(SCH_2CH_2Ph)_{24}$ by single crystal X-ray crystallography, where a pair of enantiomers (i.e. right-handed and left-handed isomers) were found in the unit cell.[29] Both enantiomers exhibit the same Au_{23} kernel comprising of two icosahedra joined together via face fusion along the C_3 axis of the icosahedron. The kernel of D_{3h} symmetry is further capped by a shell comprising of 15 surface gold atoms and 24 ligands, which are arranged into three monomeric staples (RS-Au-SR, abbreviated as $Au(SR)_2$ below) and six dimeric staples (RS-Au-S(R)-Au-SR, abbreviated as $Au_2(SR)_3$). For the left-handed enantiomer, the six dimeric staples (resembling six "blades") exhibit a clock-wise

rotating distribution, while the right-handed enantiomer exhibits an anti-clockwise distribution (scheme 3.1). This rotating distribution of the dimeric staples is the origin of chirality in $Au_{38}(SR)_{24}$ nanocluster. Very recently, Burgi and coworkers successfully isolated the two enantiomers via chiral HPLC;[23] the first eluted enantiomer (designated as **1** by Burgi *et al*) exhibits a CD spectrum similar to (*S*)-Au_{38} in our work, and the second eluted enantiomer's (designated **2**) is similar to CD polaritiy of our (*R*)-Au_{38}. For convenience of discussion, we choose the polarity of the CD band at 630 nm as a signature to specify the enantiomers since the 630-nm peak is quite prominent in the Au_{38} absorption spectrum and may serve as a spectroscopic fingerprint of this cluster. Previous theoretical calculations on the right-handed isomer have shown a negative CD band at 630 nm.[30] In view of these results, enantiomer 1 in Burgi's work and our (*S*)-Au_{38} become the (–)-Au_{38} and are geometrically left-handed (Scheme 3.1, left panel), while enantiomer 2 and (*R*)-Au_{38} become (+)-Au_{38} and are geometrically right-handed (Scheme 3.1, right panel).

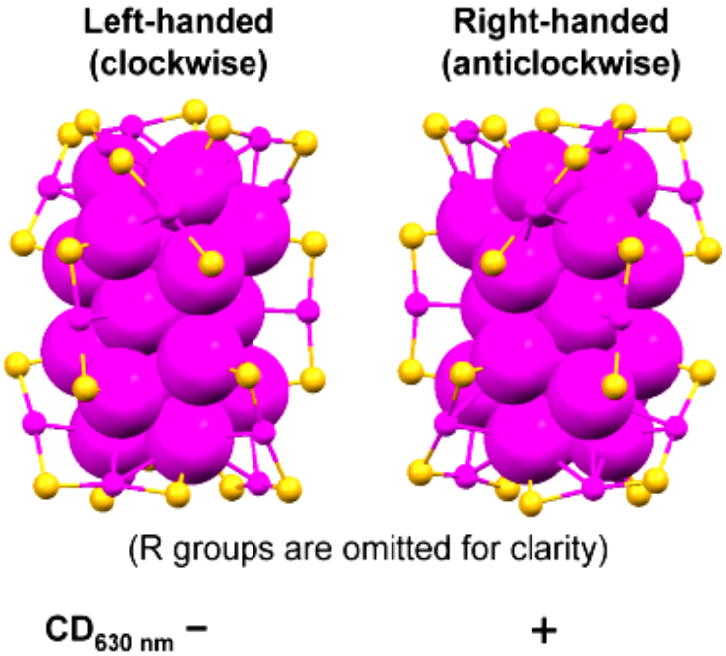

Scheme 3.1 Enantiomers of $Au_{38}(SCH_2CH_2Ph)_{24}$.

Next, we discuss the effect of chiral ligands on the metal-core structure of the Au_{38} nanoclusters. The close similarity between the absorption and CD spectra of chiral PET ligand-capped Au_{38} and achiral PET-capped Au_{38} emphatically indicates that these clusters have the same atom packing structure. Therefore, the introduction of chiral ligand does not disrupt the Au_{38} metal

core structure. More importantly, our results demonstrate that the (*S*)-PET* ligand can selectively form the left-handed Au_{38} enantiomer, while the (*R*)-PET* forms the right-handed enantiomer exclusively. It is worth analyzing the origin of chiroptical activity. In Burgi's work, the origin of the observed CD signals is attributed to the chiral Au_{38} core (i.e., no chiral ligand induction effect),[15] while in our system effects from both the Au_{38} chiral core and chiral ligand induction are present, but the latter's contribution is much smaller compared to the metal core-induced CD signals.

The attainment of (*R*)-$Au_{38}(PET^*)_{24}$ and (*S*)-$Au_{38}(PET^*)_{24}$ nanoclusters via bulk solution phase synthesis opens the possibility for practical applications such as chiral catalysis. However, their full exploitation for potential applications is somewhat limited by the fact that they are only organic soluble. Meanwhile, water-soluble nanoclusters are equally important, especially in the realm of biological applications. Thus, we further pursued the synthesis of chiral Au_{38} nanoclusters with water-soluble thiol ligands such as glutathione and captopril.

3.3.3 Synthesis of $Au_{38}(Capt)_{24}$ and $Au_{38}(SG)_{24}$ nanoclusters

The synthesis of captopril-capped $Au_{38}(Capt)_{24}$ was done via the one-pot procedure (see Experimental section for details). Briefly, $HAuCl_4 \cdot 3H_2O$ and captopril were mixed in a molar ratio of 1:3 to yield Au(I)-thiolate complexes or polymers. These Au(I) species were further reduced by addition of a relatively small amount of $NaBH_4$.

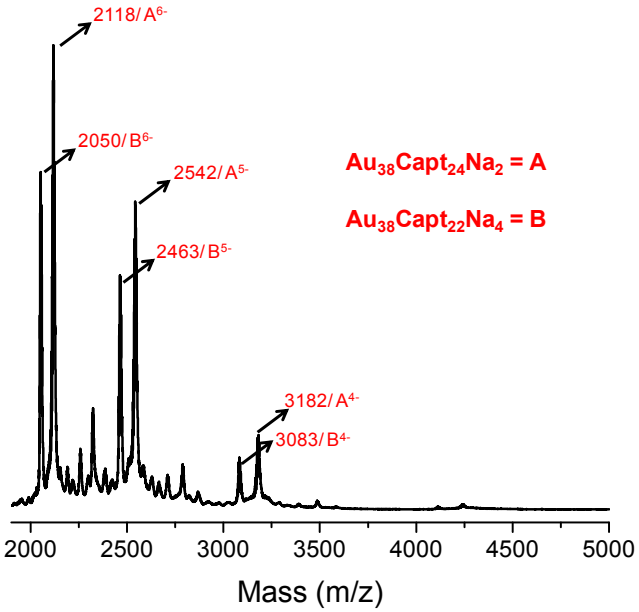

Figure 3.6 ESI-mass spectrum of $Au_{38}(Capt)_{24}$.

The size-focusing of the mixture occurred over a period of 2 days at room temperature. The final product was found to exhibit the spectral features of Au_{38}. The product was further purified by centrifugation to remove insoluble Au(I):thiolate polymer residuals. This in turn was followed by precipitation of the concentrated mixture and multiple washings with ethanol to yield pure $Au_{38}(Capt)_{24}$. The formula was further confirmed by ESI-mass spectrometry (figure 3.6). Since the ligand captopril is intrinsically charged on account of the presence of a carboxylic acid group, addition of CsOAc salt to facilitate cluster ionization was deemed unnecessary. Indeed, the $Au_{38}(Capt)_{24}$ clusters appeared as sodium adducts in the 4-, 5-, and 6- charge states in the negative mode ESI spectrum. Moreover, no other fragments were observed in the lower or higher mass range, which strongly confirms the high purity of $Au_{38}(Capt)_{24}$. The formula assignment was further confirmed by thermogravimetric analysis (TGA), where a weight loss of 40.92% was observed (figure 3.7). This value is in complete agreement with the calculated theoretical value (40.90%).

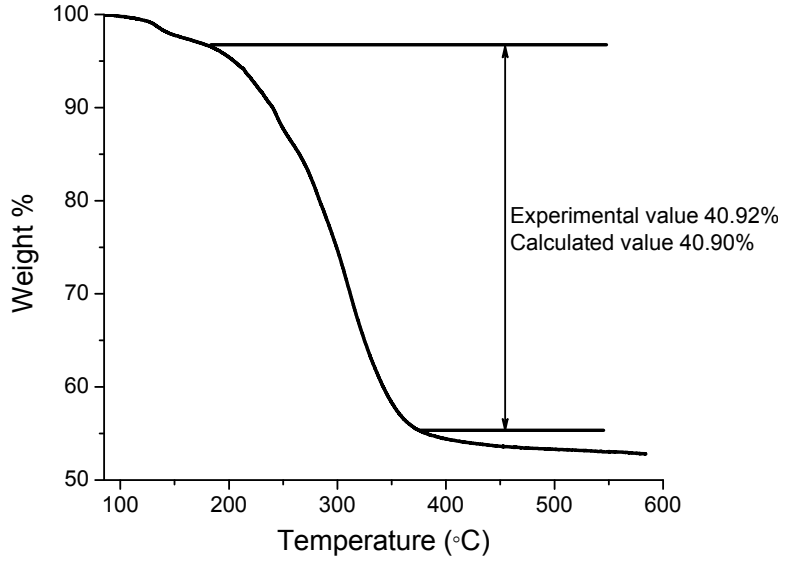

Figure 3.7 TGA of $Au_{38}(Capt)_{24}$. The weight loss at ~120 ^{o}C is due to hydroscopic nanoclusters, rather than ligand loss.

For the synthesis of water soluble, glutathione-capped $Au_{38}(SG)_{24}$, a two-step strategy was employed as opposed to the one-pot synthesis of $Au_{38}(Capt)_{24}$. In the first step, polydisperse $Au_n(SG)_m$ clusters were prepared by a previously reported protocol.[25] These size-mixed clusters were then treated with excess glutathione at 55 °C in water for 4-5 hr.[26] The product so obtained

was then centrifuged to isolate it from insoluble Au(I):SG polymers. The supernatant (containing nanoclusters) was further precipitated with ethanol to obtain pure nanoclusters. The collected product was subjected to polyacrylamide gel electrophoresis (PAGE). $Au_{38}(SG)_{24}$ appears as a well separated band. The $Au_{38}(SG)_{24}$ clusters were then isolated as described in the experimental section. The UV-Vis-NIR absorption spectrum of the as-collected product confirms Au_{38} nanoclusters, evidenced by the presence of all the signature peaks of racemic $Au_{38}(PET)_{24}$.[28] The $Au_{38}(SG)_{24}$ nanoclusters have a prominent peak around 625 nm and 1060 nm (figure 3.8), with the latter being attributed to the HOMO-LUMO gap absorption; of note, the HOMO-LUMO absorption peak is damped in the UV-vis spectra (up to 1100 nm only) shown in Figure 3.4 A (afore-discussed) and Figure 3.9 (*vide infra*) due to its proximity to the detection limit of the silicon photodiode detector (up to 1100 nm wavelength).

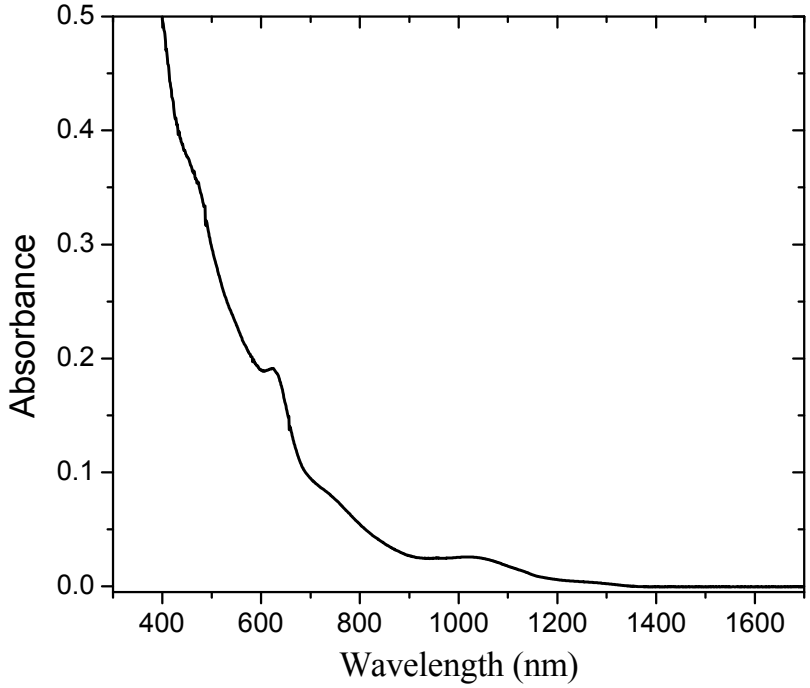

Figure 3.8 UV-Vis-NIR absorption spectra of $Au_{38}(SG)_{24}$. The 1100 nm peak corresponds to the HOMO-LUMO gap absorption of the cluster.

3.3.4 Chiroptical properties of $Au_{38}(Capt)_{24}$ and $Au_{38}(SG)_{24}$ nanoclusters

The absorption spectra for $Au_{38}(Capt)_{24}$ and $Au_{38}(SG)_{24}$ are shown in figure 3.9 (left panels A and B). Indeed, their CD spectra exhibit quite different signals, figure 3.9 (right panels C and D).

In particular, the CD signal for $Au_{38}(SG)_{24}$ shows three positive bands at 350 nm, 388 nm, 636 nm and four negative bands at 282 nm, 446 nm, 563 nm, 743 nm.

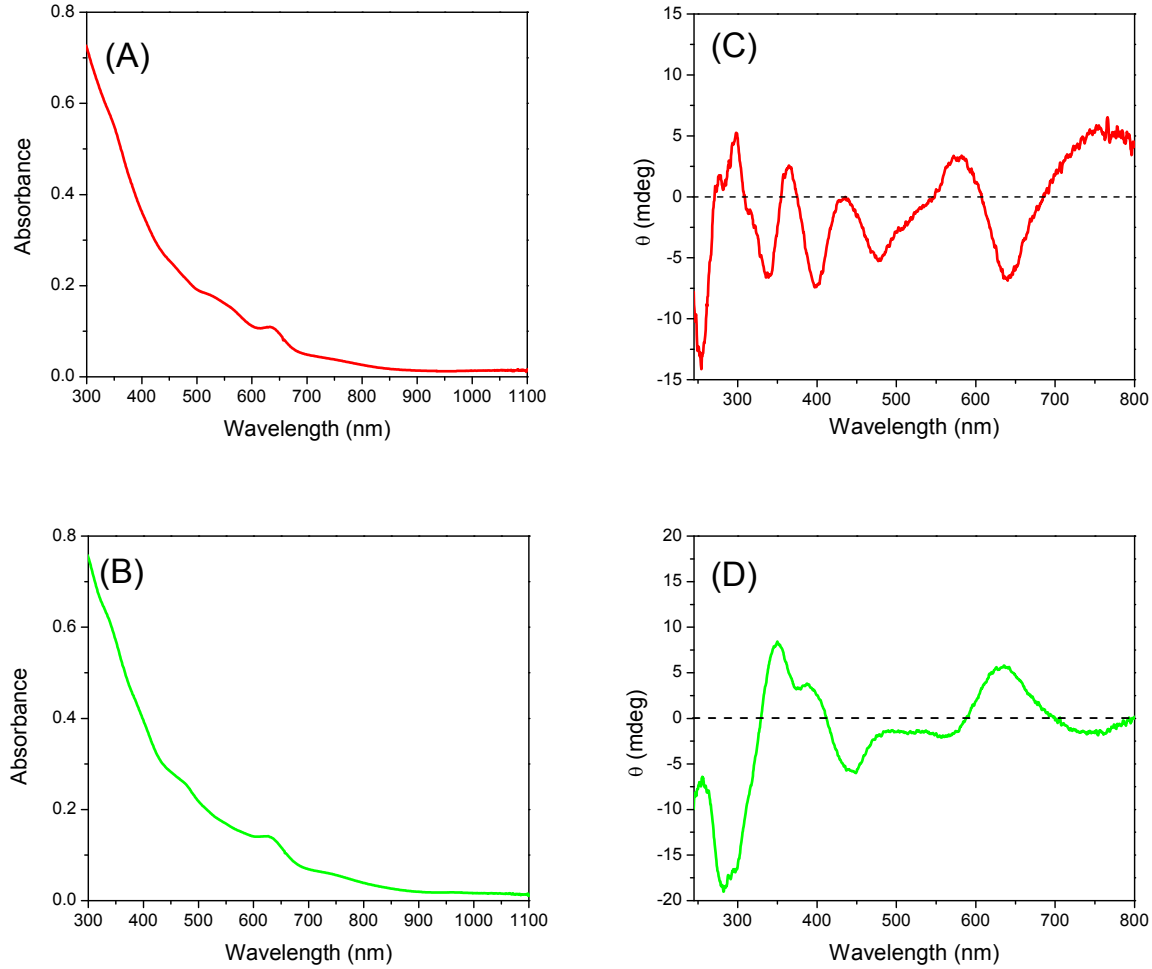

Figure 3.9 UV-Vis absorption spectra of (A) $Au_{38}(Capt)_{24}$ and (B) $Au_{38}(SG)_{24}$ (left panels). CD spectra of (C) $Au_{38}(Capt)_{24}$ and (D) $Au_{38}(SG)_{24}$ (right panels).

The anisotropy factor ($\Delta A/A=g$, where A stands for absorbance) calculated for the $Au_{38}(SG)_{24}$ cluster at various wavelengths is tabulated in 3.1. The highest value observed for the anisotrpy factor is $+1.08\times10^{-3}$ at 620 nm which is comparable to Burgi's chiral HPLC-isolated enantiomers of $Au_{38}(SCH_2CH_2Ph)$. The sample purity and the PAGE gel conditions govern the purity of the final product. In our work, the clusters are of molecular purity where no impurities were detected, as verified by running the PAGE gel multiple times. We next look closely at the CD spectrum of $Au_{38}(Capt)_{24}$, it shows four positive bands at 297 nm, 365 nm, 577 nm, 754 nm and five negative bands at 255 nm, 338 nm, 400 nm, 480 nm, 639 nm. These are somewhat different from both

$Au_{38}(SG)_{24}$ and Au_{38}(PET*), indicating the influence of the specific ligand type on the CD signals from the Au_{38} metal core. We further calculated the anisotropy factor for $Au_{38}(Capt)_{24}$ at different wavelengths (table 3.1). The highest anisotropy factor observed for this cluster was found to be $+4\times10^{-3}$ at 747 nm. This, indeed, is the highest anisotropy value obtained for any of the previously reported gold nanoclusters with any ligand.

Table 3.1 Wavelength and anisotropy factor (g), and signs for $Au_{38}SG_{24}$ and $Au_{38}(Capt)_{24}$ clusters

Wavelength (nm)	$Au_{38}SG_{24}$ (g)	Wavelength (nm)	$Au_{38}(Capt)_{24}$ (g)
747	-8.3×10^{-4}	747	$+4\times10^{-3}$
620	$+1.08\times10^{-3}$	629	-1.4×10^{-3}
568	-3.5×10^{-4}	564	$+4.9\times10^{-4}$
512	-2.3×10^{-4}	479	-7.1×10^{-4}
449	-6.4×10^{-4}	449	-1.8×10^{-4}
385	$+2.4\times10^{-4}$	393	-5.1×10^{-4}
354	$+4.3\times10^{-4}$	345	-2.6×10^{-4}
296	-6.6×10^{-4}	298	$+2.1\times10^{-4}$
239	-1.8×10^{-4}	245	-2.4×10^{-4}

3.3.5 Comparison of the absorption and chiroptical properties of Au38 Capped with different ligand

The different chiroptical responses of the Au_{38} clusters capped with the three different ligands are fascinating, which is in striking contrast with their similar UV-vis absorption spectra (as shown in figure 3.10 left panel). This explicitly proves that inspite of having the same core (i.e. Au_{38}) and the same types of staple motifs (i.e. dimeric and monomeric staples) around the core, the capping ligand shell plays quite a significant role in defining the chiroptical behavior. Since the Au_{38} core is inherently chiral, the influence of different chiral ligands shows a pronounced difference in the chiroptical response of the overall cluster. Not only some of the CD band locations are changed, but also the chiroptical response for the clusters shows quite different chiral response below 600 nm wavelength (figure 3.10 , right panel).

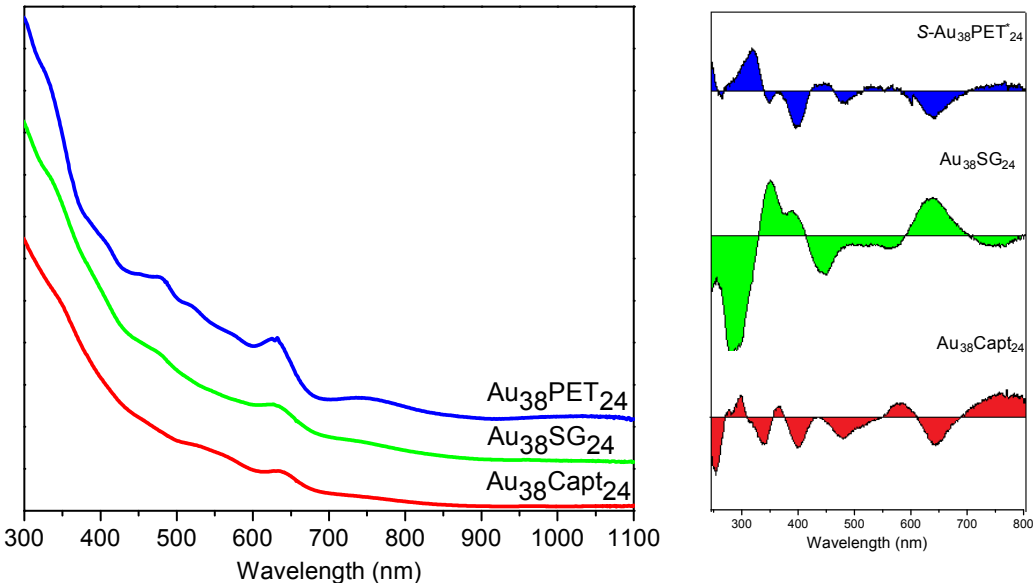

Figure 3.10 Absorption spectra (left panel) and CD spectra for (*S*)-$Au_{38}(PET^*)_{24}$, $Au_{38}(SG)_{24}$, and $Au_{38}(Capt)_{24}$

3.3.6 Synthesis of $Au_{40}(Capt)_{24}$ nanoclusters

The size focusing synthesis of $Au_{38}(Capt)_{24}$ was stopped at 24-30 hr to control the growth process which results to $Au_{40}(Capt)_{24}$ nanoclusters. It is important to mention that if the size-focusing reaction is run for 48 hr all the $Au_{40}(Capt)_{24}$ nanoclusters are converted into more stable $Au_{38}(Capt)_{24}$ nanoclusters. Therefore, the controlled growth process governs the formation of Au_{40} nanoclusters. Figure 3.11 (A) shows the UV-Vis absorption spectra and (B) TGA of the gel isolated $Au_{40}(Capt)_{24}$ clusters

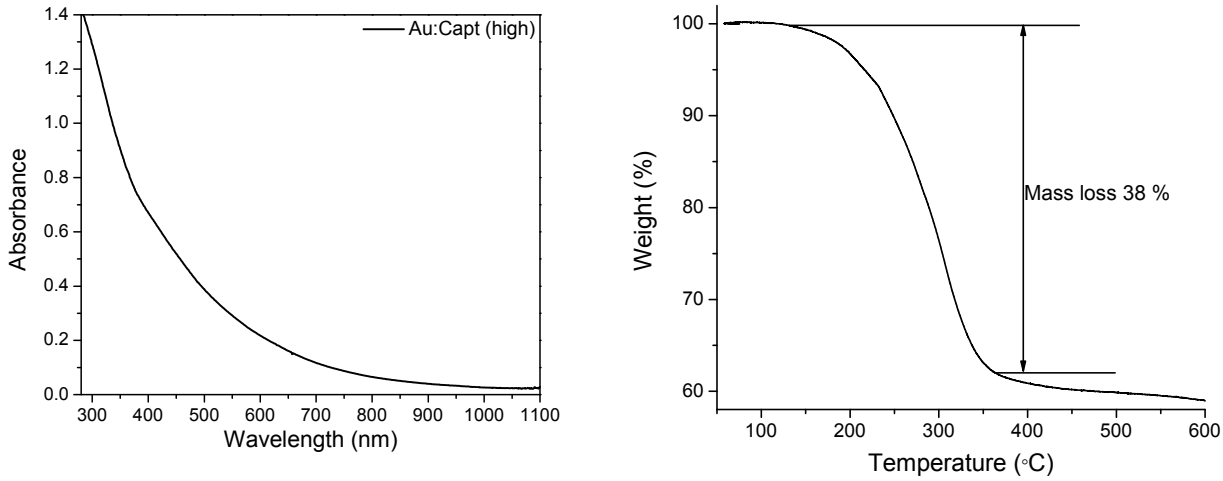

Figure 3.11 (A) Absorption spectra and (B) TGA of the $Au_{40}(Capt)_{24}$ nanoclusters.

3.4 Summary

In conclusion, we have successfully achieved the first direct enantioselective synthesis of Au_{38} and Au_{40} nanocluster enantiomers using chiral ligands. Although the Au_{38} nanocluster exhibits inherent chirality due to the staple motifs, the structure of chiral ligands can influence the chiroptical behavior of the core to a significant extent, as evidenced by the different CD spectra of the Au_{38} nanoclusters capped by the different types of ligands. These observations explicitly prove that the chiral response of ligand-protected nanoclusters has major influences from both the metal atom arrangement and the ligand shell around it. In addition, the high molecular purity and the facile synthesis of chiral Au_{38} and Au_{40} nanoclusters are expected to make them attractive candidates for future exploration of chiral catalysis and other chiroptical applications.

3.5 References

1) Wang, Y.; Xu, J.; Wang, Y.; Chen, H. *Chem. Soc. Rev.* **2013**, *42*, 2930-2962.
2) Hashmi, A. S. K.; Hutchings, G. J. *Angew. Chem. Int. Ed.* **2006**, *45*, 7896-7936.
3) Gautier, C.; Taras, R.; Gladiali, S.; Burgi, T. *Chirality* **2008**, *20*, 486-493.
4) Tamura, M.; Fujihara, H. *J. Am. Chem. Soc.* **2003**, *125*, 15742-15743.
5) Plum, E.; Zhou, J.; Dong, J.; Fedotov, V.; Koschny, T.; Soukoulis, C.; Zheludev, N. *Phys. Rev. B* **2009**, *79*, 035407-035411.
6) Zhang, S.; Park, Y. S.; Li, J.; Lu, X.; Zhang, W.; Zhang, X. *Phys. Rev. Lett.* **2009**, *102*, 23901-23905.
7) Shukla, N.; Bartel, M. A.; Gellman, A. J. *J. Am. Chem. Soc.* **2010**, *132*, 8575-8580.
8) Astruc, D.; Daniel, M. C.; Ruiz, J. *Chem. Commun.* **2004**, 2637-2649.
9) Lim, I. I. S.; Mott, D.; Engelhard, M. H.; Pan, Y.; Kamodia, S.; Luo, J.; Njoki, P. N.; Zhou, S.; Wang, L.; Zhong, C. J. *Anal. Chem.* **2009**, *81*, 689-698.
10) Nishida, N.; Yao, H.; Kimura, K. *Langmuir* **2008**, *24*, 2759-2766.
11) Shemer, G.; Krichevski, O.; Markovich, G.; Molotsky, T.; Lubitz, I.; Kotlyar, A. B. *J. Am. Chem. Soc.* **2006**, *128*, 11006-11007.
12) Wang, Y.; Wang, Q.; Sun, H.; Zhang, W.; Chen, G.; Wang, Y.; Shen, X.; Han, Y.; Lu, X.; Chen, H. *J. Am. Chem. Soc.* **2011**, *133*, 20060-20063.
13) Schaaff, T. G.; Knight, G.; Shafigullin, M. N.; Borkman, R. F.; Whetten, R. L. *J. Phys. Chem. B* **1998**, *102*, 10643-10646.
14) Schaaff, T. G.; Whetten, R. L. *J. Phys. Chem. B* **2000**, *104*, 2630-2641.
15) Zhu, M.; Qian, H.; Meng, X.; Jin, S.; Wu, Z.; Jin, R. *Nano Lett.* **2010**, *11*, 3963-3969.
16) Gautier, C.; Burgi, T. *J. Am. Chem. Soc.* **2006**, *128*, 11079-11087.
17) Kumar, S.; Jin, R. *Nanoscale* **2012**, *4*, 4222-4227.
18) Yao, H.; Fukui, T.; Kimura, K. *J. Phys. Chem. C* **2008**, *112*, 16281-16285.
19) Abdulrahman, N. A.; Fan, Z.; Tonooka, T.; Kelly, S. M.; Gadegaard, N.; Hendry, E.; Govorov, A. O.; Kadodwala, M. *Nano Lett.* **2012**, *12*, 977-983.
20) Garzón, I. L.; Reyes-Nava, J. A.; Rodríguez-Hernández, J.; Sigal, I.; Beltrán, M.; Michaelian, K. *Phys. Rev. B* **2002**, *66*, 073403.
21) Yao, H.; Miki, K.; Nishida, N.; Sasaki, A.; Kimura, K. *J. Am. Chem. Soc.* **2005**, *127*, 15536-15543.

22) Zhu, Z.; Liu, W.; Li, Z.; Han, B.; Zhou, Y.; Gao, Y.; Tang, Z. *ACS Nano* **2012**, *6*, 2326-2332.
23) Dolamic, I.; Knoppe, S.; Dass, A.; Bürgi, T. *Nat. Commun.* **2012**, *3*, 798.
24) Knoppe, S.; Dolamic, I.; Dass, A.; Bürgi, T. *Angew. Chem. Int. Ed.* **2012**, *51*, 7589-7591.
25) Negishi, Y.; Nobusada, K.; Tsukuda, T. *J. Am. Chem. Soc.* **2005**, *127*, 5261-5270.
26) Shichibu, Y.; Negishi, Y.; Tsunoyama, H.; Kanehara, M.; Teranishi, T.; Tsukuda, T. *Small* **2007**, *3*, 835-839.
27) Qian, H.; Zhu, Y.; Jin, R. *J. Am. Chem. Soc.* **2010**, *132*, 4583-4585.
28) Qian, H.; Zhu, Y.; Jin, R. *ACS Nano* **2009**, *3*, 3795-3803.
29) Qian, H.; Eckenhoff, W. T.; Zhu, Y.; Pintauer, T.; Jin, R. *J. Am. Chem. Soc.* **2010**, *132*, 8280-8281.
30) Lopez-Acevedo, O.; Akola, J.; Whetten, R. L.; Gro□nbeck, H.; Ha□kkinen, H. *J. Phys. Chem. C* **2009**, *113*, 5035-5038.

Chapter 4

Core-size and Ligand Dependent Fluorescence Properties of Gold nanoclusters

4.1 Introduction

Gold nanoparticles are amongst the most studied nanostructures due to their tunable electronic structures and material properties.[1] Amongst the unique properties shown by nano-meter sized gold, surface plasmon resonance (SPR) is undoubtedly the most fascinating one. The SPR arises from the collective oscillation of free electron in the continuous band structure and can be precisely tuned by varying the structural parameters such as size, aspect ratio, shape, and the capping ligand.[2] The plasmonic properties of gold has been well documented in the past few decades but very little attention has been given to the luminescence properties of gold nanoparticles. After decades of sustained effort, luminescent gold nanoparticle has emerged as new class of material.[3-5] The recent work in this field has enabled researchers to synthesize different sized luminescent gold nanoparticles with high quantum yield and explore various applications. Although, the luminescence properties of gold nanoparticles have been studied recently, the observation of fluorescence from gold metal dates back to 1969 by the pioneering work of Mooradia.[6] By using a 488 nm laser power, the gold and copper films are excited and photoluminescence was observed at 564 and 620 nm respectively. Since copper and gold have continuous conduction band (sp band) structure, the observed luminescence was attributed to the interband (d-sp) transitions than intraband (within sp band) transition. Scheme 4.1 shows the first proposed mechanism to explain the luminescence form gold and other metal films. The emission in this case is due to the recombination of electrons at the Fermi level to the holes in the upper lying d level. Although the photoluminescence from the metal system, with high density of states and large number of free electrons was quite unusual as compared to the traditional fluorophores, the work still did not get much attention because the quantum yield (QY) was extremely low (10^{-10}). The study of SERS on thin metal film shed some light on the emission properties of metals as a constant emission background was observed in the SERS of metal films. Boyd *et al* from their study on metals films showed that the emission of gold films are in the range of 400-650 nm and

the emission maxima depends upon the excitation wavelength and also on the roughness of the film.[7] The surface roughness enhances the photoluminescence due to the field effect. This study also suggested that the emission from the gold film is due to the radiative recombination of electrons below the Fermi level to the holes in the d-bands.

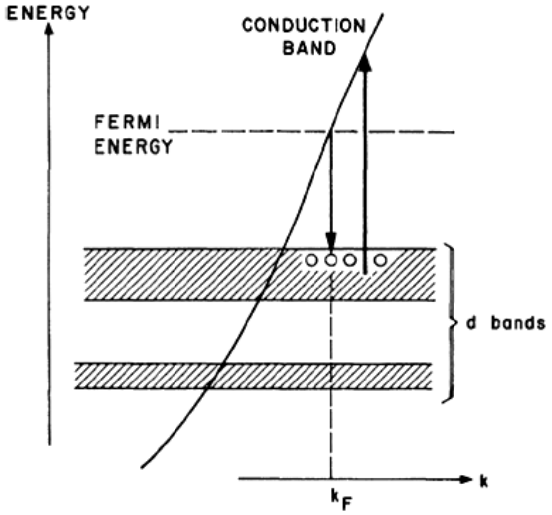

Scheme 4.1 Schematic of band structure of noble metals showing the mechanism of photoluminescence (excitation and recombination transitions). Reproduced with permission from ref. 6. Copyright 1969 @ American Physical Society.

The luminescence was not just observed from the gold films rather small gold nanoparticles also showed luminescence properties. Wilcoxon observed an intense blue fluorescence (QY 10^{-5}) which was a million times higher than the bulk gold (QY 10^{-10}) from Au nanoparticles of size below 5 nm, albeit the source of emission was not clear.[8] Mohammad *et al* observed a luminescence at 560 nm from the Au nanorod with quantum yield ~10^{-5} (million times higher than the bulk gold) and also observed that the QY increases quadratically with the excitation power while the wavelength maxima increases linearly with the length. In case of these small nanoparticles or nanorods, the emission was proposed to follow the same mechanism of interband recombination of the electron and the hole and enhances with the surface plasmon.

Although the local electric-field enhancement was proposed to be the reason for enhancement in the photoluminescence of these nanoparticles described above, several reports of photoluminescence from the small nanoparticles which does not exhibit surface plasmon resonance (SPR) showed that SPR may not be the reason for their high QY emission. Whetten and coworkers reported the near-infra red luminescence from 1.1 and 1.7 nm Au nanoparticles

which did not show SPR. Their QY was found to be ~ (4.4±1.5)×10^{-5}.[9] Murray and coworkers observed luminescence at 700 nm from 1.7 nm Au nanoparticles with a QY of 3×10^{-3}.[10] Similarly Link *et al.* observed an emission at 770 nm by Au_{28} nanoclusters with a QY of 2×10^{-3}. The fluorescence observed in this case was 10^{-7} times higher than Au film. Link *et al.,* further proposed that fluorescence in case of small molecular clusters can come from both the intraband (sp-sp) and interband (d-sp) transitions as shown in scheme 4.2.[11]

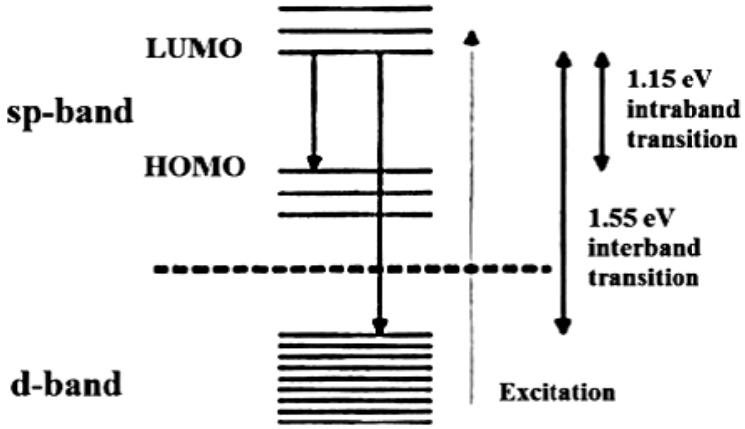

Scheme 4.2 Solid-state model showing the origin of two luminescence bands from Au_{28} clusters. The high-energy band is purposed to be arising from the radiative interband (d-sp) recombination while the low-energy band is thought to arise from the radiative intraband (sp-sp) transition across the HOMO-LUMO gap. Reproduced with permission from ref. 11 with permission. Copyrigth@ 2002 American Chemical Society.

The particle size of the Au nanoparticles governs its electronic structure. As the nanoparticle size becomes smaller and comparable to the electron Fermi wavelength of Au atom (0.5 nm),[12] the band structure shows splitting and it appears as discrete energy level instead of continuous band.[13] At this small scale, the nanoparticles are composed of few atoms and their properties differ greatly from the bulk metal, from their bigger analogs; and they are called nanoclusters or clusters. Harbich *et al* successfully captured Au_2 and Au_3 clusters in argon matrix and observed that these small clusters are quite fluorescent although the quantitative correlation of particle size and emission wavelength was not clear.[14] Zheng *et al.* successfully employed PAMAM dendrimers to synthesize water-soluble Au_8 nanoclusters encapsulated in the dendrimers. These Au_8 clusters showed blue emission at 455 nm and the QY of 4×10^{-1}.[15] This was the first report of such a high QY from any Au nanoparticle system. To further investigate the role of size in the

emission of gold clusters, Zheng *et al.* synthesized Au nanoclusters of different size by varying the ratio of dendrimer, Au salt and the reducing agent. The different size Au clusters obtained were Au_5, Au_8, Au_{13}, Au_{23}, and Au_{31} with their emission maxima ranging from UV to NIR region.[16] For small Au clusters, the dependence of emission energy on the number of gold atoms (N), in each Au clusters can be fit with a scaling relation of $E_f / N^{1/3}$, where E_f is the Fermi energy of bulk gold (5.53 eV). This work concluded that with the increase in number of gold atoms, the excitation and emission maxima shifts to longer wavelength (figure 4.1 A). Also, the emission energy decreases with increase in the number of gold atoms in the clusters (figure 4.1 B).[16]

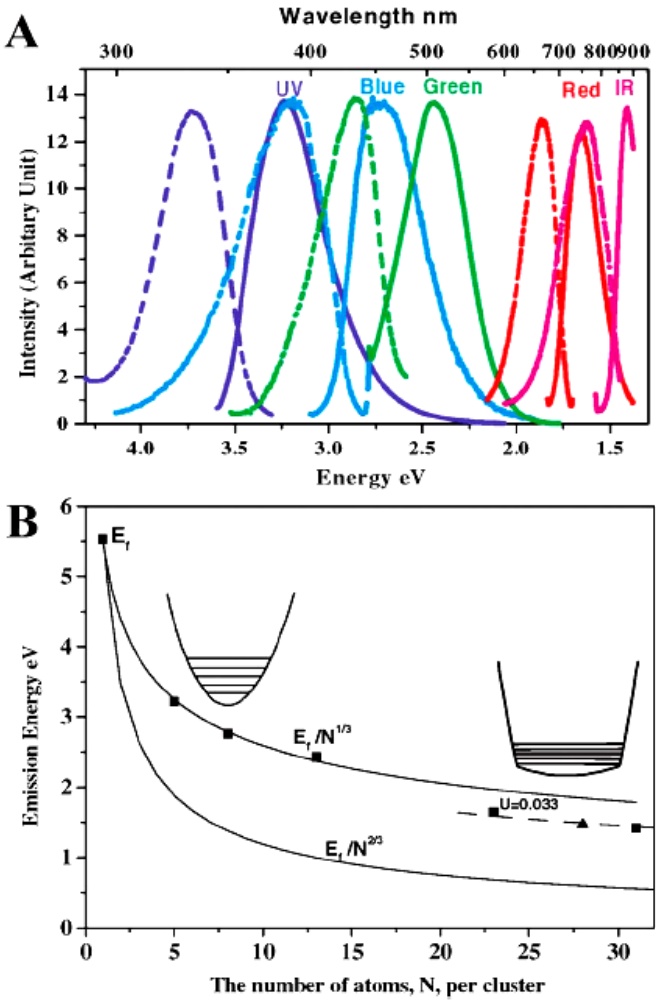

Figure 4.1 (A) Shows the excitation (dashed line) and emission (solid) spectra of gold clusters (As the size of the clusters increases, the excitation and the emission spectra shifts towards red), **(B)** Correlation

of emission energy with the number of gold atoms (N) per clusters. Reproduced with permission from ref. 16. Copyright 2004 American Physical Society.

The study of dendrimer capped Au clusters revealed that the capping ligand has a little influence on the photoluminescence property of the clusters. Therefore, with the same core-size the emission should remain the same by any change of capping ligand. The Au_8 clusters reported by various groups with different capping ligands resulted in the same blue emission.[17-19] This was further observed for Au_3 clusters, where the same emission property was observed for different ligands. Jin *et al.* observed that the Au_3 core capped with dodecanethiol has emission ~ 340 nm,[20] similarly Gonzalez *et al.* reported the Au_2 and Au_3core capped with poly (N-vinylpyrrolidone) with their emission maxima lying at 315 and 335 nm respectively.[21]

As the size of the nanoclusters increases, its emission energy is slightly deviated from the perfect free electron model due to the screening of electron and a small harmonic distortion in the potential energy well.[22] Tsukuda *et al.* reported the series of Au nanoclusters capped with glutathione $Au_{10}(SG)_{10}$, $Au_{15}(SG)_{13}$, $Au_{18}(SG)_{14}$, $Au_{22}(SG)_{16}$, $Au_{22}(SG)_{17}$, $Au_{25}(SG)_{18}$, $Au_{29}(SG)_{20}$, $Au_{33}(SG)_{22}$, and $Au_{39}(SG)_{24}$ and it was observed that the emission of these nanoclusters are not dependent on the clusters size, which was in sharp contrast to the dendrimer capped nanoclusters.[23]

In case of Au_{25} nanoclusters, the crystal determination revealed the presence of Au_{13} icosahedral core with six staple motifs of Au_2S_3 surrounding the core. Theoretical calculation on the electronic structure of Au_{25} showed that the first peak which is the HOMO-LUMO gap at 1.8 eV is due to the sp-sp intraband transition. The second peak at 2.75 eV is the combined effect of sp-sp intarband transition and also the interband d-sp transitions. The third peak at 3.1 eV corresponds to interband d-sp transition. The electronic transition also explains the origin of fluorescence in these clusters. Goodson *et al.* studied the ultrafast relaxation dynamics of Au_{25} and observed two emission peaks ~ 500 and 700 nm.[24] This study suggested that the 500 nm emission peak arises due to the electron hole recombination in the Au_{13} core. These transitions will have a little influence from the capping ligand. The NIR emission at 700 nm can originate from the recombination of holes in the ground core state and electron decay from the core excited state to the S-Au-S-Au-S staple motif as shown in figure 4.2.[24] If we consider the Au_{13} core as an isolated cluster, the short wavelength emission at 500 nm (2.48 eV) was observed to be close to 2.43 eV emission from dendrimer capped Au_{13} clusters. This suggested that surface

ligand has little influence in the core electronic structure. Very recently, Wu *et al.* showed that the ligand governs the luminescence properties of Au_{25} nanoclusters and any change in the ligand changes the fluorescence intensity and the position of their wavelength maxima.[25]

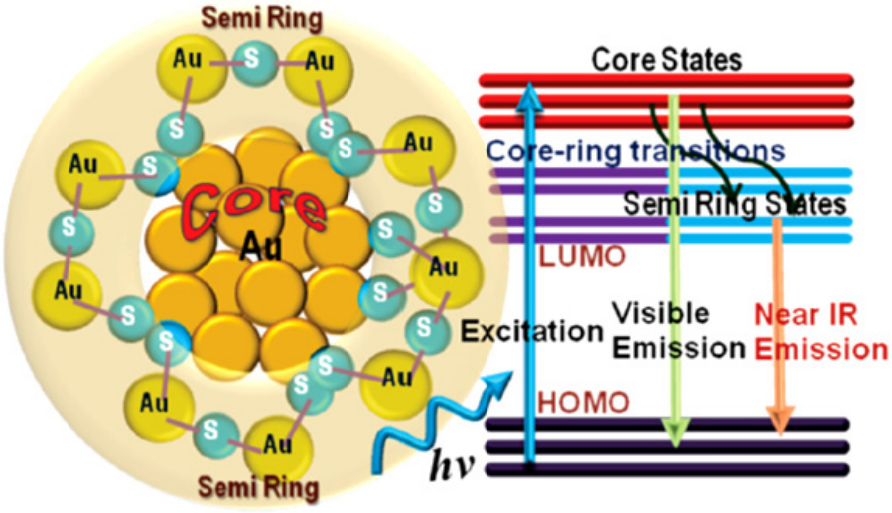

Figure 4.2 Relaxation pathways in Au_{25} clusters. The electrons in the ground states are excited to excited states of the Au_{13} core and then either directly relax back to HOMOs of the core and emit at 500 nm or decay to the semi ring states, followed by relaxing back to the ground states and emitting NIR photons for 700 nm . Reproduced with permission from ref. 24. Copyright @ 2010 American Chemical Society.

Therefore, by changing the capping ligand, the fluorescence intensity and the emission profile changes. This observation was in quite contrast to the all the previous studies on Au clusters. This became the motivation of our work. As predicted by several experiments, the same size cluster was predicted to have the same emission profile, also as the cluster size increases the emission maxima shifted to the higher wavelength. In our work, we studied the fluorescence properties of several Au_{25} nanoclusters capped with different ligands to quantify the effect of ligand on the capping ligand same. This study was to get a better understanding of the fluorescence mechanism of the nanoclusters. Also, our work revealed that the fluorescence is independent of the cluster size. The excitation and emission wavelength was varied to get a complete picture of the radiative decay in these clusters. The ultrafast study of Au_{25} nanoclusters showed two distinct emission peak at 500 and 700 nm respectively which does not appears as a resolved peak in their regular emission studies. Therefore, we decided to study the fluorescence

at cryogenic temperature to resolve the distinct electronic transition in their emission spectra. The life-time decay for several reported Au cluster was studied in the past and it was observed that these few atoms Au clusters have very short leaved emission profile with the lifetime of few nanoseconds. Also, as the excitation wavelength was changed, the lifetime of the nanoclusters showed a dramatic shift and a lifetime of few μs was observed. To understand the decay kinetics of all these clusters in consideration we performed the lifetime study for the clusters. We studied the lifetime with varying time scale to quantify the decay kinetics.

4.2 Experimental

4.2.1 Synthesis of Au nanoclusters

The synthesis of $Au_{25}(Capt)_{18}$, $Au_{25}(SG)_{18}$, $Au_{25}(PET^{*})_{18}$ nanoclusters has been described in chapter 2. $Au_{15}(SG)_{13}$ and $Au_{18}(SG)_{14}$ are also obtained as a separate band while running the etched Au:SG nanoclusters through the gel. These bands are isolated following the protocol for isolating $Au_{25}(SG)_{18}$ nanoclusters as explained in Chapter 2 (experimental section). The synthesis of $Au_{25}(PET)_{18}$ nanoclusters was done similar to the synthesis of $Au_{25}(PET^{*})_{18}$ where the PET ligand was used instead of PET^{*} in the synthesis process.

4.2.2 Characterization

UV-Vis spectra of the Au_{25} clusters were acquired by Hewlett- Packard (HP) Agilent 8453 diode array spectrophotometer at room temperature. Glutathione capped nanoclusters was dissolved in water, while aromatic thiol capped nanoclusters were dissolved in toluene. Fluorescence spectra were recorded on a Fluorolog-3 spectrofluorometer (HORIBA Jobin Yvon). For the convenience of comparison, the excitation wavelength was fixed at 375 and 514 nm (from a Xe arc source) for all the cluster species in emission measurements. The band pass for both the emission and excitation was fixed to 5 nm. Quantum yields (QY) were measured with dilute solutions of clusters (~0.05 OD absorption at 514 nm) using $[Au_{25}(SG)_{18}]^{-}$ as a reference (QY: 2×10^{-3})[26]. Cryogenic measurement was done by using FL-1013 liquid nitrogen dewar assembly compatible with Fluorolog-3 spectrofluorometer. Water-soluble nanoclusters was mixed with ethylene glycol and water in 2:1 ratio and degassed for 15 min in vacuum and then slowly dropped in liquid nitrogen to form glass for the fluorescence measurement. For aromatic thiol capped nanoclusters, 1:1 mixture of toluene and acetonitrile was used as a solvent for forming glass. Fluorescence lifetimes were measured with a time-correlated single photon counting (TCSPC)

technique; a pulsed LED source (376 nm, 1.1 ns) was used to excite the clusters. The emission was monitored at 700 nm. The lifetime measurement was done for different time scale and the amplitude was averaged for all the data.

4.2.3 Quantum yield determination of Au nanoclusters

The quantum yield of $Au_{25}(SG)_{18}$ nanoclusters has been reported by various group and the QY value was found to be 2.0×10^{-3}.[23,26] Therefore, this was considered as a standard for the determination of QY for other Au nanoclusters. To determine the QY, dilute solution of $Au_{25}(Capt)_{18}$, $Au_{15}(SG)_{13}$ and $Au_{18}(SG)_{14}$ nanoclusters was prepared and the optical density of the solution at 514 nm (excitation wavelength) was kept below 0.05. The aqueous solution of nanoclusters was diluted with 200 µl of water every time and the absorbance and emission spectra were recorded. From the resulted emission profile, the area of the fluorescence spectra was calculated. This integrated fluorescence intensity for each dilution was plotted against their absorption value at 514 nm and finally a straight line was fitted for the plot of Integrated fluorescence Intensity Vs absorbance. The gradient and the slope of this straight line was recorded. The same process was repeated for the $Au_{25}(SG)_{18}$ nanoclusters and the gradient and slope was determined for the straight line fit for the integrated fluorescence intensity and absorbance values. The gradient of the standard ($Grad_{ST}$), the test solution ($Grad_X$), and the quantum yield of the standard (Φ_{ST}) was plugged in the equation 4.1 to get the QY of the test solution (Φ_X) i.e. Au nanoclusters. The η_X and η_{ST} are the viscosity of test solution and the standard. In this case, both the solutions are dissolved in water so the viscosity was found to be same for the standard and the test solution.

$$\Phi_X = \Phi_{ST}\left(\frac{Grad_X}{Grad_{ST}}\right)\left(\frac{\eta_X^2}{\eta_{ST}^2}\right)$$

Equation 4.1 Quantum Yield determination of an unknown solution with reference to the standard

For $Au_{25}(Capt)_{18}$ nanoclusters the absorption, emission, and the integrated fluorescence intensity plots have been shown in figure 4.3. The gradient value was obtained from the straight line and finally the QY was calculated by using the equation 4.1. The QY for $Au_{25}(Capt)_{18}$ nanoclusters was found to be 5×10^{-3}. The comparison of fluorescence intensity for the similar concentrations

of $Au_{25}(Capt)_{18}$ and $Au_{25}(SG)_{18}$ in chapter 2 has already shown that $Au_{25}(Capt)_{18}$ nanoclusters has slightly higher fluorescence than $Au_{25}(SG)_{18}$ at room temperature.[27]

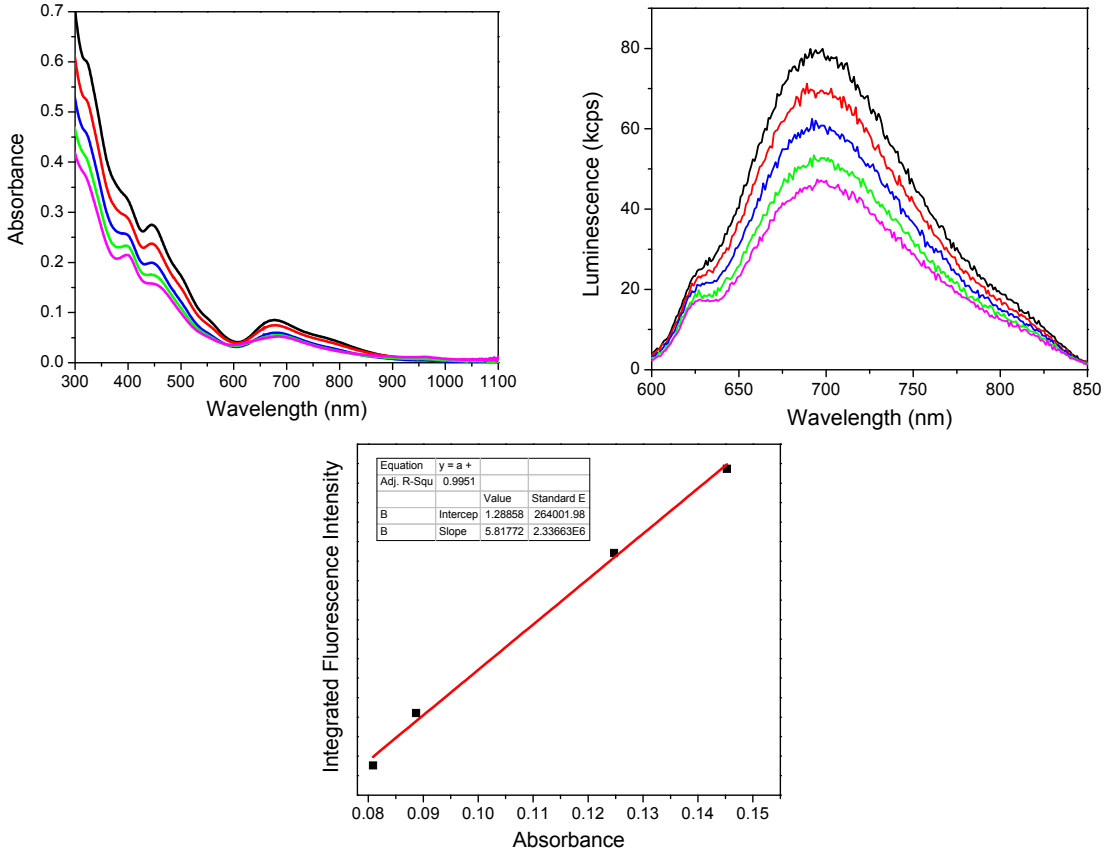

Figure 4.3 Absorption (top left panel) emission (top right panel) and the integrated fluorescence intensity plot (bottom) for $Au_{25}(Capt)_{18}$ nanoclusters at different dilution.

For $Au_{15}(SG)_{13}$ and $Au_{18}(SG)_{14}$ the reported QY was 2×10^{-4} and 4×10^{-3} respectively.[23] In our study of these nanoclusters, we observed a strong emission from these nanoclusters. The emission intensity was ~ 10-15 times higher than the $Au_{25}(SG)_{18}$ nanoclusters so we decided to calculate the QY for these nanoclusters. The low QY observed by Tsukuda *et al.* may be due to the poor separation of these nanoclusters in the gel matrix. In our synthesis and PAGE experiment, we were able to get a baseline separation of these nanoclusters (figure 2.1(B) chapter 2) and so the QY for ultra-pure cluster can be calculated. For $Au_{15}(SG)_{13}$ nanoclusters, the absorbance, fluorescence, and the integrated fluorescence has been shown in figure 4.4. The QY was calculated using equation 4.1 and the observed QY was 3×10^{-2}, which is ~15 times higher than $Au_{25}(SG)_{18}$ nanoclusters.

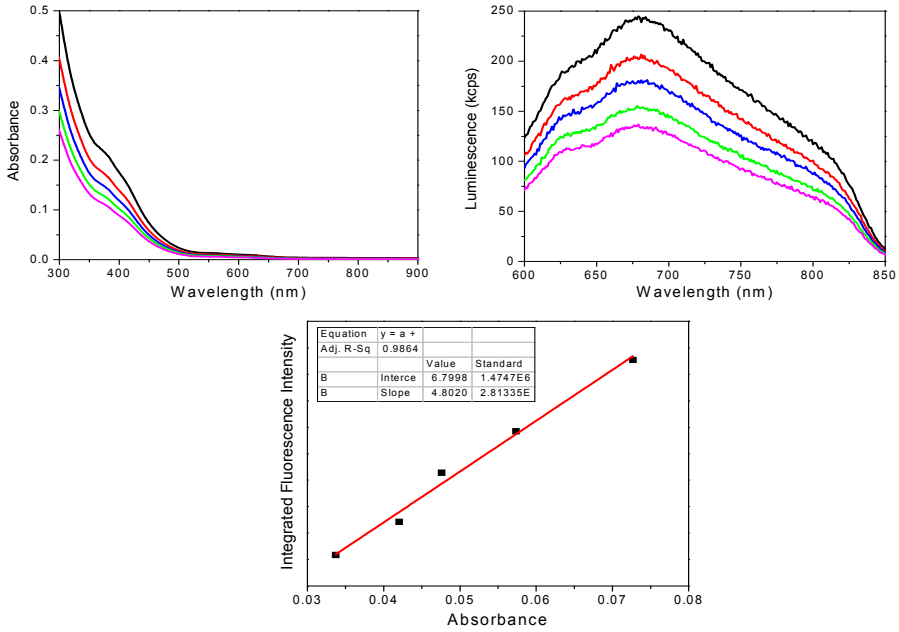

Figure 4.4 Absorption (top left panel) emission (top right panel) and the integrated fluorescence intensity plot (bottom) for $Au_{15}(SG)_{13}$ nanoclusters at different dilution.

Similarly, for $Au_{18}(SG)_{14}$ nanoclusters the calculated QY value was found to be 2×10^{-2}, which is ~10 times higher than $Au_{25}(SG)_{18}$ nanoclusters.

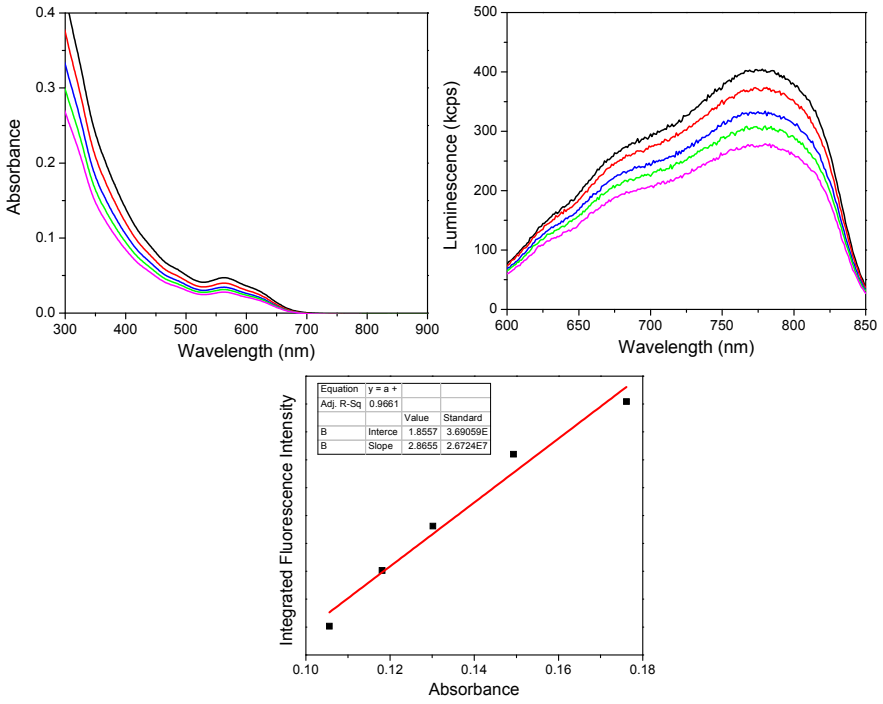

Figure 4.5 Absorption (top left panel) emission (top right panel) and the integrated fluorescence intensity plot (bottom) for $Au_{18}(SG)_{14}$ nanoclusters at different dilution.

4.3 Results and Discussion

4.3.1 Ligand dependent fluorescence properties of Au_{25} nanoclusters

The study of emission properties of Au_3 and and Au_8 nanoclusters clusters capped with different ligands has been shown to have similar emission profile with different capping ligand. However, Wu *et al.* observed distinct emission profile for Au_{25} capped with glutathione and phenyl ethanethiol. This contradiction motivated us to study the effect of capping ligand on the fluorescence properties of Au_{25} nanoclusters. Scheme 4.3 shows the structure of four different ligand employed in this study.

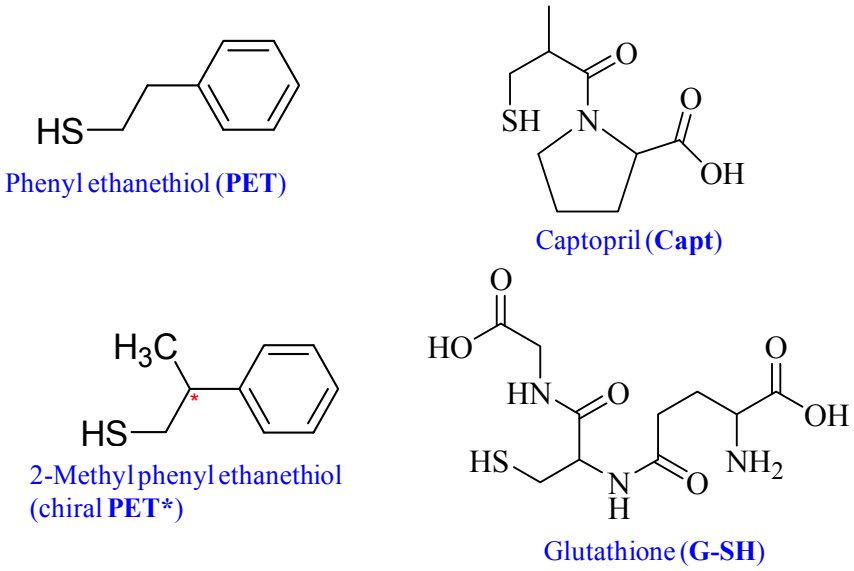

Scheme 4.3 Showing the structure of ligands involved in the fluorescence study

The absorption spectra of Au_{25} capped with PET, PET^*, Capt and GSH has been shown in figure 4.6. The absorption spectra for all these nanoclusters were perfectly overlapping with peaks at 400, 450, and 670 nm. The change of ligand does not show any change in their spectral profile. However, the fluorescence spectra of these Au_{25} nanoclusters capped with a different thiolate ligand shows a very different profile. The emission spectra at 514 nm excitation shows (figure 4.7 left panel) that $Au_{25}(Capt)_{18}$ has highest emission than $Au_{25}(SG)_{18}$, $Au_{25}(PET)_{18}$, $Au_{25}(PET^*)_{18}$ nanoclusters. For $Au_{25}(Capt)_{18}$, and $Au_{25}(SG)_{18}$ the emission profile is similar with emission maxima ~715 nm. The $Au_{25}(PET)_{18}$ has been reported to have its emission maxima in the NIR region ~900 nm, but the cut-off limit (850 nm) of the detector in our measurement,

limits the fluorescence maxima ~825 nm which is not the actual maxima. The emission profile for $Au_{25}(PET^{*})_{18}$ is similar to $Au_{25}(PET)_{18}$ with slightly lower fluorescence intensity.

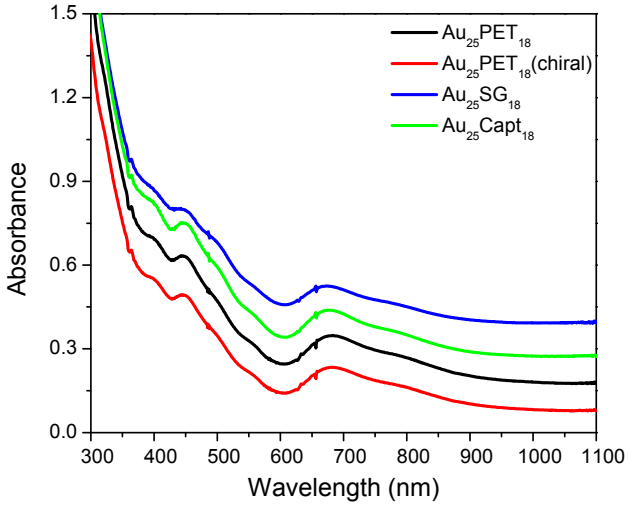

Figure 4.6 Absorption spectra of Au_{25} capped with different ligands. (The spectra has been offset for clarity.)

The emission profile is similar for excitation at 375 and 514 nm excitation, with 375 nm excitation results to enhanced emission intensity for all the nanoclusters (figure 4.7 right panel) This observation is in contrast with the previous study of Au_8 and Au_3 nanoclusters where the change of ligand did not altered the emission profile and the emission maxima.

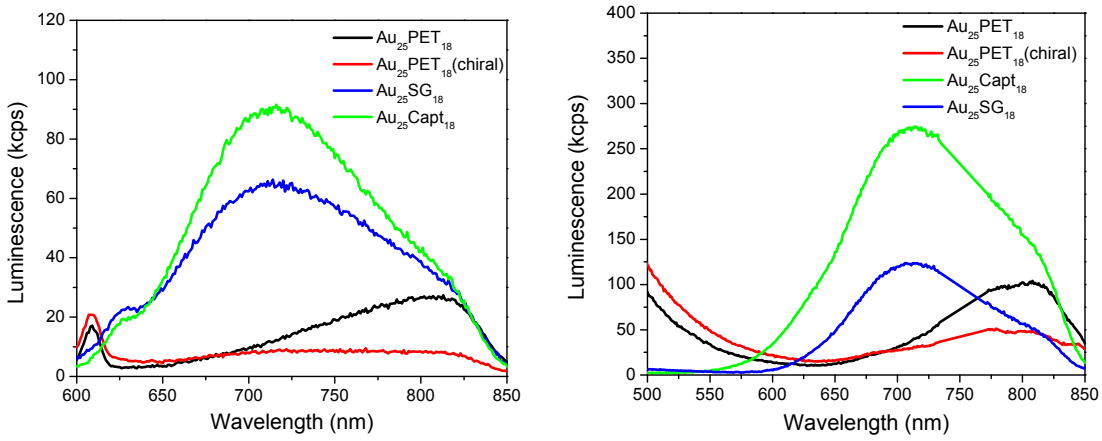

Figure 4.7 Emission spectra of Au_{25} capped with different ligands (left panel 514 nm excitation, right panel 375 nm excitation).

4.3.2 Fluorescence properties of $Au_{25}(PET)_{18}$

For $Au_{25}(PET)_{18}$ nanoclusters, the absorption, emission and excitation spectra is shown in figure 4.8. The excitation spectra at 700 and 800 nm emission was acquired which showed very low intensity with no significant features. The emission spectra at 375 and 514 nm showed similar emission profile with emission maxima ~820 nm. For 375 nm excitation, emission was found to be more intense than 514 nm excitation. The blank region in the emission profile is due to the double wavelength artifact at ~ 750 nm for 375 nm excitation. This artifact has been deleted.

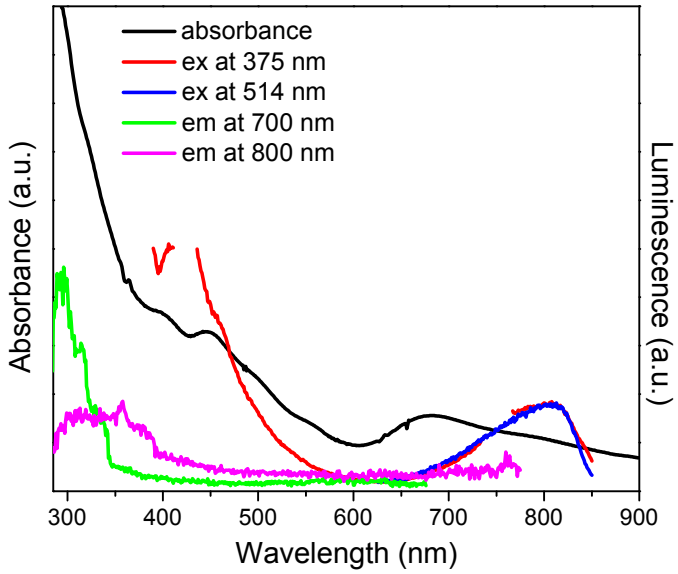

Figure 4.8 Absorption (black), emission (red, blue) and excitation spectra (green, magenta) of $Au_{25}(PET)_{18}$ cluster. The emission spectra (excitation at 375 nm) has been scaled 10 times to fit on the same scale.

The full width at half maxima (FWHM) of the emission profile was ~ 200 nm (not observed in this measurement due to detector limit of 850 nm) and the emission profile showed a shoulder below 500 nm. The ultrafast study of $Au_{25}(PET)_{18}$ nanoclusters have showed two emission emission peak at 500 and 700 nm respectively.[24] The important question is; can these emission peak be resolved in regular emission measurement. To achieve that, we measured the fluorescence at cryogenic temperature (77 K). The nanoclusters were cooled in liquid nitrogen, which led to the formation of glass (solvent was changed to 1:1, toluene: acetonitrile) and then emission measurement were done by maintaining the nanoclusters at 77 K. The emission profile which appeared as a broad peak at room temperature split into two peaks at 575 nm and 725 nm

(for 375 nm excitation). The double wavelength artifact has been deleted. In addition, the emission intensity was enhanced ~50 times (room temperature data has been scaled 10 times in the plot) as shown in figure 4.9 left panel. In case of 514 nm excitation, the emission peak also split into two peaks with both the emission maxima shifted towards red and appeared at 715 and 815 nm. The emission intensity was also enhanced for the cryogenic data (514 nm excitation) with the enhancement of ~25 times as compared to the room temperature data as shown in figure 4.9 (right panel: room temperature data has been scaled 10 times in the plot). Therefore, the emission spectra can split into two peaks at cryogenic temperature, where the electronic contribution from the core and the staple motif can be observed clearly. The peak intensity of 575 nm peak was observed to be more dominant than the peak intensity at 725 nm. We speculate that the higher temperature sensitivity of this peak may be due to the contribution from just the core (metal atoms); while the peak at 725 nm may have a lesser temperature sensitivity as the staple motif is constructed by both the Au atoms and the S atoms.

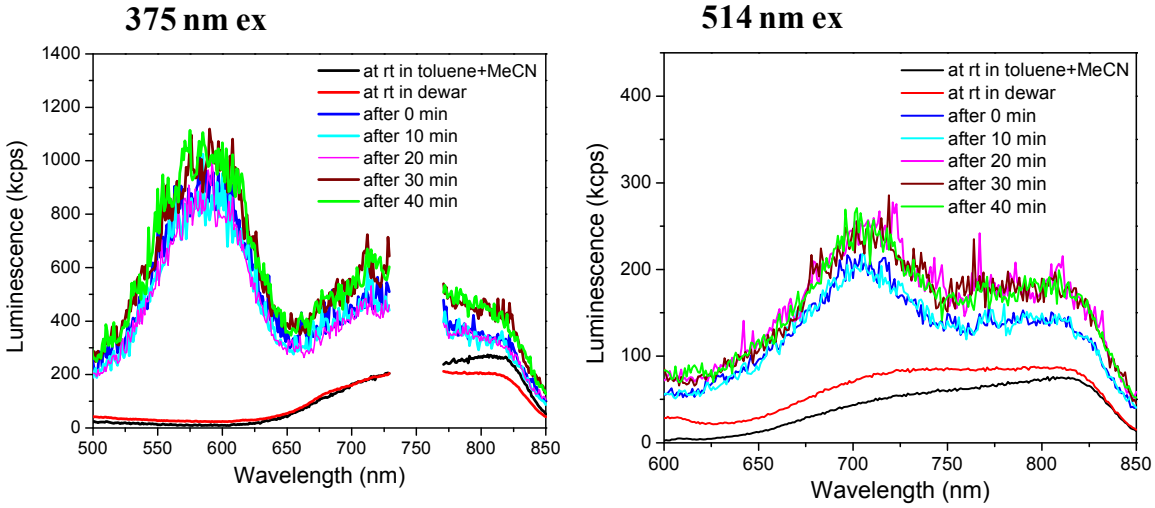

Figure 4.9 Emission spectra of $Au_{25}(PET)_{18}$ at cryogenic temperature (left panel 375 nm excitation, right panel 514 nm excitation). The blank between the spectra in the left panel is due to the double wavelength artifact which has been deleted.

4.3.3 Fluorescence properties of $Au_{25}(PET^{*})_{18}$

The absorption, emission, and excitation spectra of $Au_{25}(PET^{*})_{18}$ nanoclusters is shown in figure 4.10. Although the absorption profile is similar, the emission and the excitation spectra is quite different than $Au_{25}(PET)_{18}$ nanoclusters. The excitation spectra, for 700 and 800 nm emission

showed very low intensity with no significant features. The emission spectra at 375 and 514 nm excitation, showed similar emission profile with emission maxima ~790 nm. For 375 nm excitation, emission was found to be more intense than 514 nm excitation, which is similar to the emission profile of $Au_{25}(PET)_{18}$.

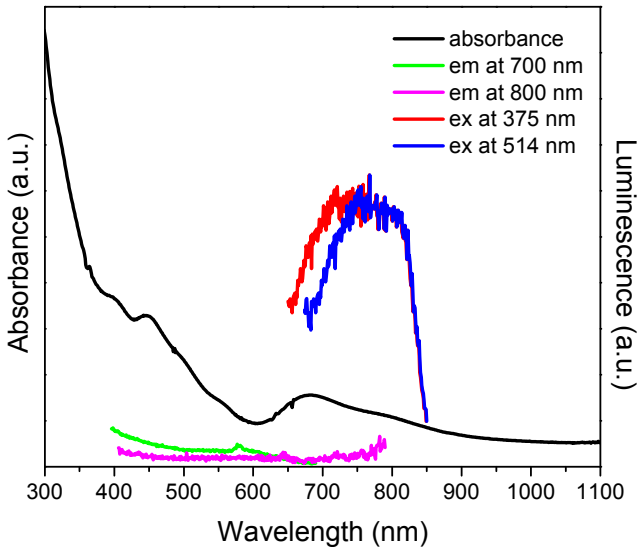

Figure 4.10 Absorption (black), emission (red, blue) and excitation spectra (green, magenta) of $Au_{25}(PET^{*})_{18}$ cluster. The emission spectra (excitation at 375 nm) has been scaled 10 times to fit on the same scale.

The emission was measured at cryogenic temperature and the similar splitting of the emission peak was observed at the low temperature. For 375 nm excitation, the emission peak clearly splitted into two peaks at 580 and 750 nm. The blank space in the 750 nm peak is due to double wavelength artifact, which has been deleted. The emission measured at cryogenic temperature (375 nm excitation) has been enhanced 10 times in comparison to the room temperature data (figure 4.11, left panel).

4.3.4 Fluorescence properties of $Au_{25}(Capt)_{18}$

The absorption, emission, and excitation spectra of $Au_{25}(Capt)_{18}$ nanoclusters is shown in figure 4.12. Although the absorption spectrum is similar to the Au_{25} nanoclusters capped with aromatic ligands, the emission and excitation spectra showed marked difference. The excitation spectra at 700 and 800 nm emission showed multiple with significant intensity with excitation at 700 nm emission being more intense than excitation at 800 nm emission. The emission spectra of $Au_{25}(Capt)_{18}$ nanoclusters shows a much narrower emission peak with the emission maxima at ~

700 nm. The emission spectra showed more intense peak for 375 nm excitation than 514 nm excitation.

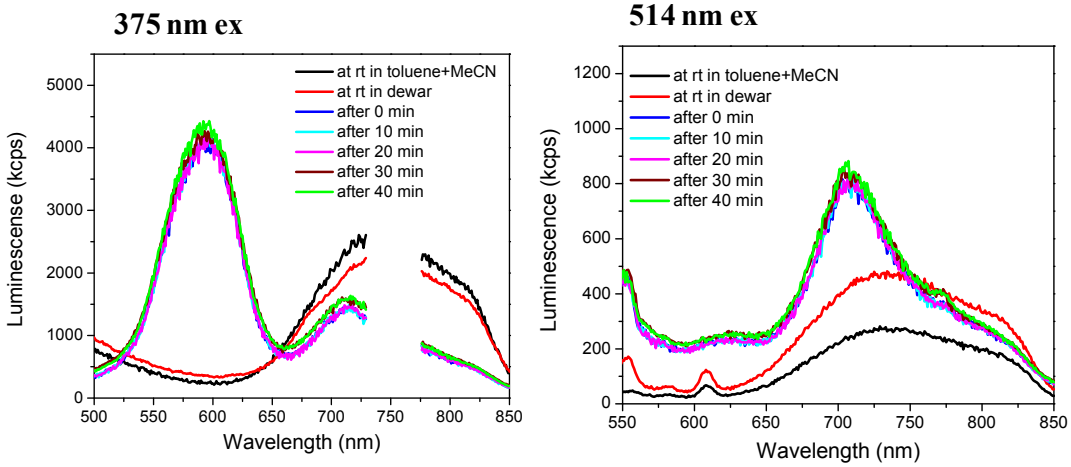

Figure 4.11 Emission spectra of $Au_{25}(PET^{*})_{18}$ at cryogenic temperature (left panel 375 nm excitation, right panel 514 nm excitation). The blank between the spectra in the left panel is due to the double wavelength artifact. The cryogenic data has been scaled 10 times (for 375 nm excitation).

For 514 nm excitation, the broad emission peak at room temperature did not showed a clear splitting pattern, rather a hump around 625 nm and a peak at 710 nm.

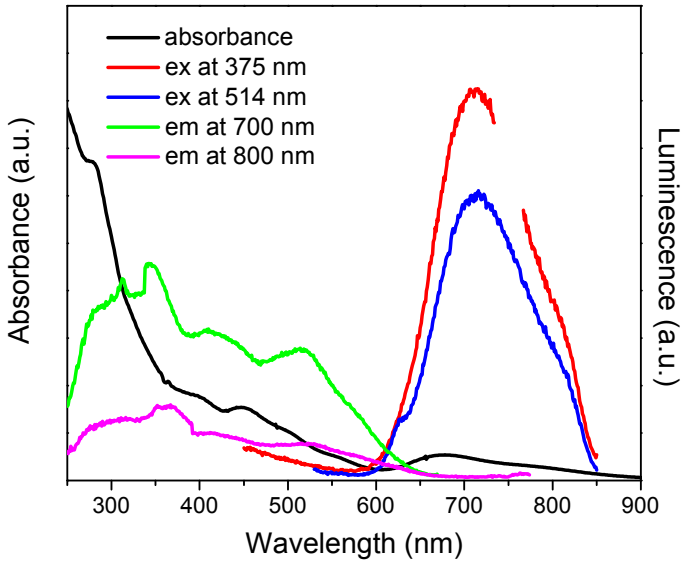

Figure 4.12 Absorption (black), emission (red, blue) and excitation spectra (green, magenta) of $Au_{25}(Capt)_{18}$ cluster. The emission spectra (excitation at 375 nm) has been scaled 5 times to fit on the same scale. The blank space in the red curve is due to the double wavelength artifact, which has been deleted.

The cryogenic measurement of the emission for $Au_{25}(Capt)_{18}$ nanoclusters revealed that 375 nm excitation can be clearly resolved into two emission peak with emission maxima at 570 and 710 nm . The emission peak at 710 nm was more prominent than 550 nm peak which was quite different than the case of $Au_{25}(PET)_{18}$ and $Au_{25}(PET^{*})_{18}$ where the later peak was more prominent. The emission at cryogenic temperature was enhanced 10 time than the emission at room temperature (figure 4.13 left panel).

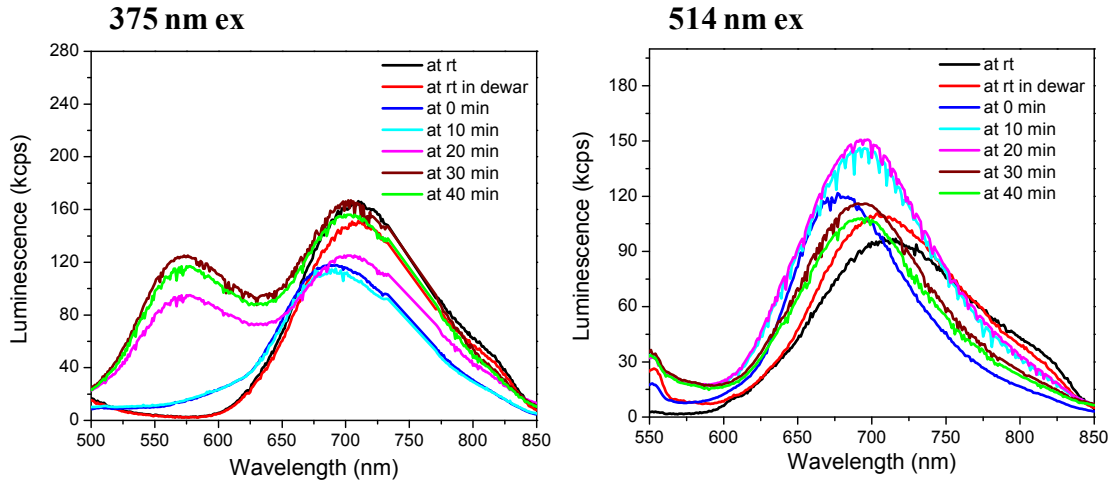

Figure 4.13 Emission spectra of $Au_{25}(Capt)_{18}$ at cryogenic temperature (left panel 375 nm excitation, right panel 514 nm excitation). The cryogenic data has been scaled 10 times (for 375 nm excitation) and 5 times (for 514 nm excitation).

For 514 nm excitation, the emission peak at room temperature did not showed any splitting pattern, except a slight blue shift of the emission peak (at 710 nm), observed for cryogenic measurement. The emission at cryogenic temperature was enhanced by 5 times than the room temperature data (figure 4.13 right panel).

4.3.5 Fluorescence properties of $Au_{25}(SG)_{18}$

The absorption, emission, and excitation spectra of $Au_{25}(SG)_{18}$ nanoclusters is shown in figure 4.14. Although the absorption spectra are similar to the Au_{25} nanoclusters reported above, the emission and excitation spectra showed marked difference. The excitation spectra at 700 and 800 nm emission showed peaks at 270, 350, and 580 nm. The emission spectra of $Au_{25}(SG)_{18}$ nanoclusters shows a much broad emission peak than $Au_{25}(Capt)_{18}$ with the emission maxima at ~ 720 nm. The emission peak showed the FWHM of ~250 nm. The emission spectra showed more intense peak for 375 nm excitation than 514 nm excitation.

The cryogenic measurement of the emission of $Au_{25}(SG)_{18}$ nanoclusters revealed that the emission spectra showed a blue shift with peak partially resolving into two peaks at 610 and 690 nm (for 375 nm excitation) as shown in figure 4.15 left panel. The 575 nm excitation also shifted the peak to lower wavelength with the splitting of peak partially into two shallow peak at 625 and 680 nm. The emission intensity of the lower wavelength peak (610 and 625 nm) in both the excitation was quite different than the case of aromatic thiol capped Au_{25} nanoclusters.

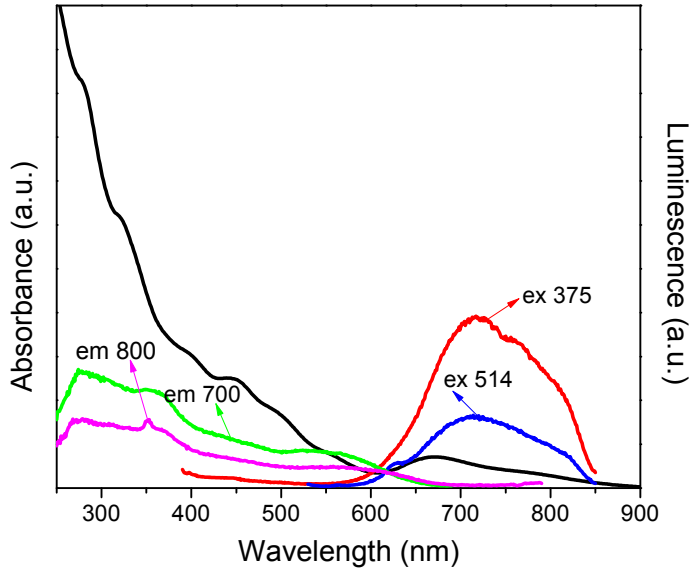

Figure 4.14 Absorption (black), emission (red, blue) and excitation spectra (green, magenta) of $Au_{25}(SG)_{18}$ cluster.

The emission peak in this case was also enhanced for the cryogenic measurement with the 375 nm excitation leading to the enhancement of 10 times than the room temperature measurement while for 514 nm the emission peak was enhanced ~5 times as shown in figure 4.15 right panel.

4.3.6 Fluorescence properties of $Au_{15}(SG)_{13}$

The $Au_{15}(SG)_{13}$ showed an absorbance in the range of 200-510 nm region. The excitation spectra at 630 nm emission showed a peak at 360 nm and a shoulder between 400-500 nm region. The excitation spectra at 800 nm emission showed a peak at 370 nm and two shallow peak at 570 and 620 nm. The emission at 375 nm excitation showed a broad U-shaped peak with much higher intensity and a FWHM of 350 nm. The emission spectra at 514 nm excitation showed a different emission profile than 375 nm excitation, with a peak maxima at ~790 nm. The emission intensity

(for 514 nm excitation) was much lower than 375 nm excitation with a broad peak with FWHM of 250 nm (figure 4.16).

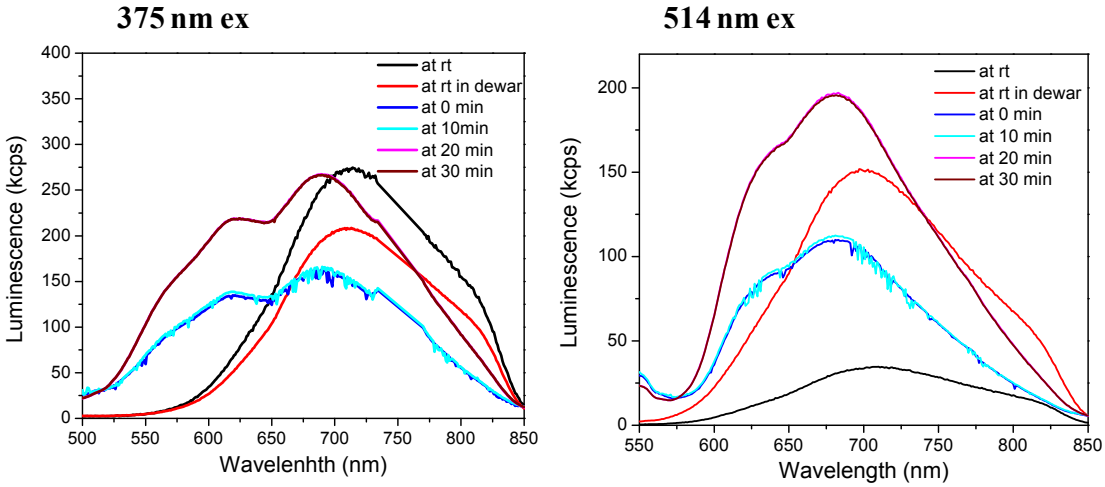

Figure 4.15 Emission spectra of $Au_{25}(SG)_{18}$ at cryogenic temperature (left panel 375 nm excitation, right panel 514 nm excitation). The cryogenic data has been scaled 10 times (for 375 nm excitation).

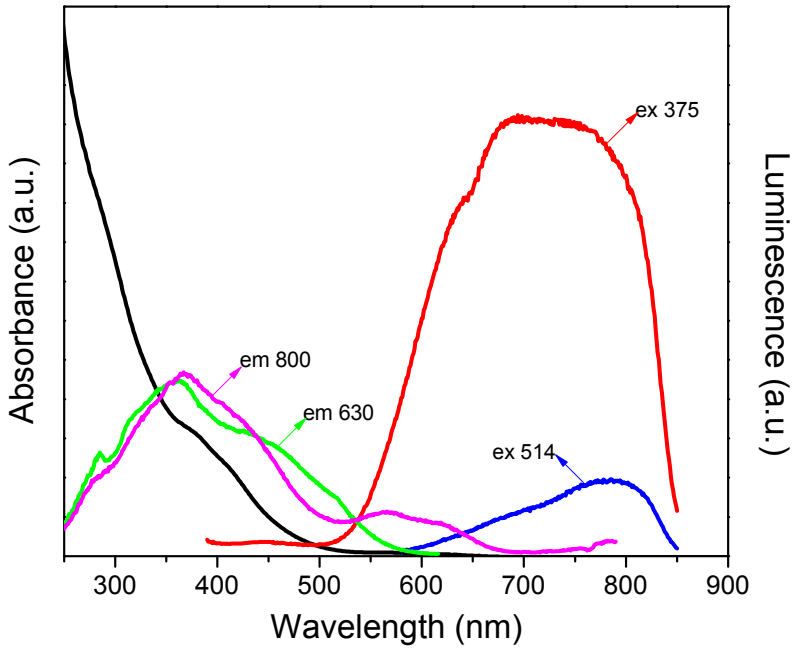

Figure 4.16 Absorption (black), emission (red, blue) and excitation spectra (green, magenta) of $Au_{15}(SG)_{13}$ cluster. The emission spectra (excitation at 375 nm) has been scaled 10 times to fit on the same scale.

The quantum yield calculation revealed that $Au_{15}(SG)_{13}$ clusters have ~15 times higher QY than $Au_{25}(SG)_{18}$ nanoclusters. The cryogenic emission study of Au_{25} nanoclusters with different ligands has revealed that emission intensity enhances significantly at low temperature. Therefore, the $Au_{15}(SG)_{13}$ nanoclusters was supposed to have significantly high emission intensity at cryogenic temperature. The cryogenic emission at 375 nm showed clear splitting of the broad emission peak into two peaks with a narrow peak at 510 nm and a very broad peak starting from 600 nm to 850 nm. The broad peak looked quite flattened, we hypothesize that the high emission intensity was reaching the saturation limit of the detector as the cryogenic data (for 375 nm excitation) was ~ 4×10^6 cps, which is significantly high (figure 4.17 left panel). The 514 nm excitation with lower emission intensity was able to resolve the broad emission peak into two clear peak at 640 and 760 nm.

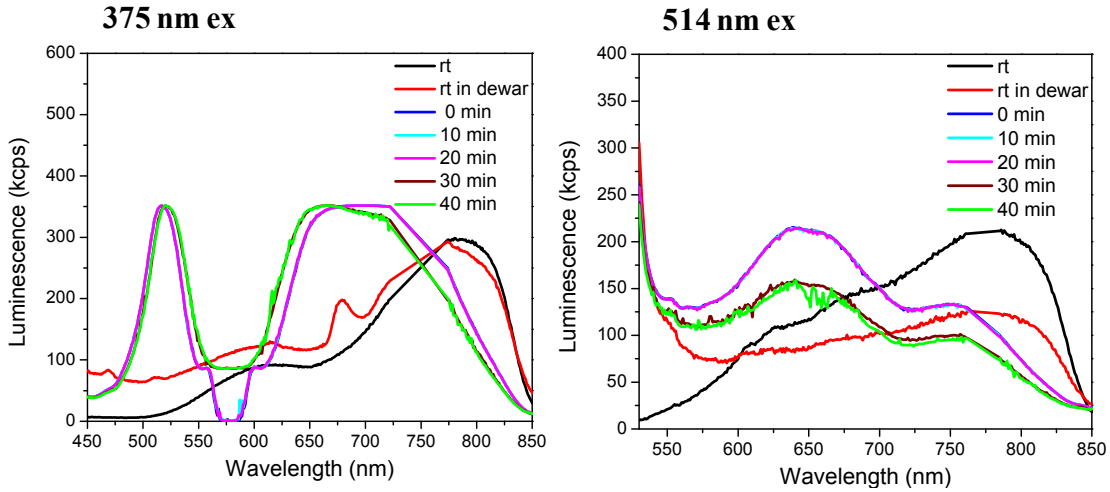

Figure 4.17 Emission spectra of $Au_{15}(SG)_{13}$ at cryogenic temperature (left panel 375 nm excitation, right panel 514 nm excitation). The cryogenic data has been scaled 100 times (for 375 nm excitation) and 50 times (for 514 nm excitation).

4.3.7 Fluorescence properties of $Au_{18}(SG)_{14}$

The absorbance spectra for Au18(SG)14 showed two shallow peak at 550 and 620 nm. The excitation spectra at 780 and 840 nm emissions showed multiple peaks at 360, 450, and two shallow peak at 570 and 620 nm. The emission for 375 nm excitation showed a shoulder at 660 nm and emission maxima at 770 nm. The emission at 514 nm excitation showed a narrow peak with emission maxima at 770 nm.

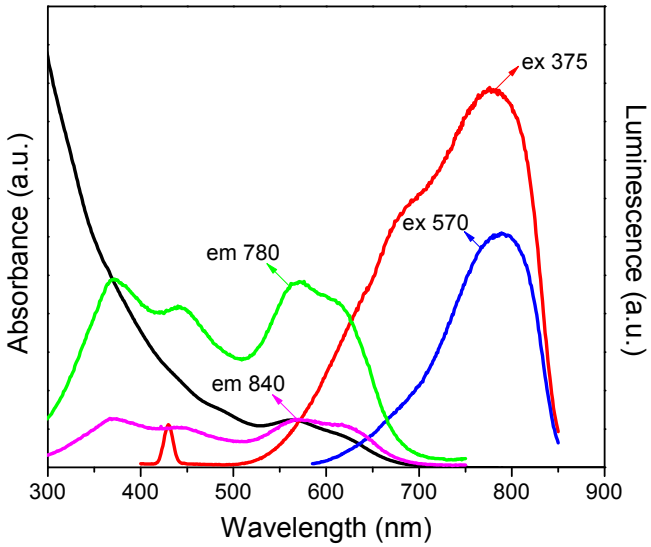

Figure 4.18 Absorption (black), emission (red, blue) and excitation spectra (green, magenta) of $Au_{18}(SG)_{14}$ cluster.

The cryogenic emission study of $Au_{18}(SG)_{14}$ nanoclusters showed a shallow peak at 525 nm with a very broad peak which again could be due to the saturation of the detector due to the very strong emission at cryogenic temperature (150 times more than the room temperature data) figure 4.19 left panel. The low emission at 514 nm excitation was clearly able to resolve the emission peak into two peaks with emission maxima at 650 and 760 nm (figure 4.19 right panel).

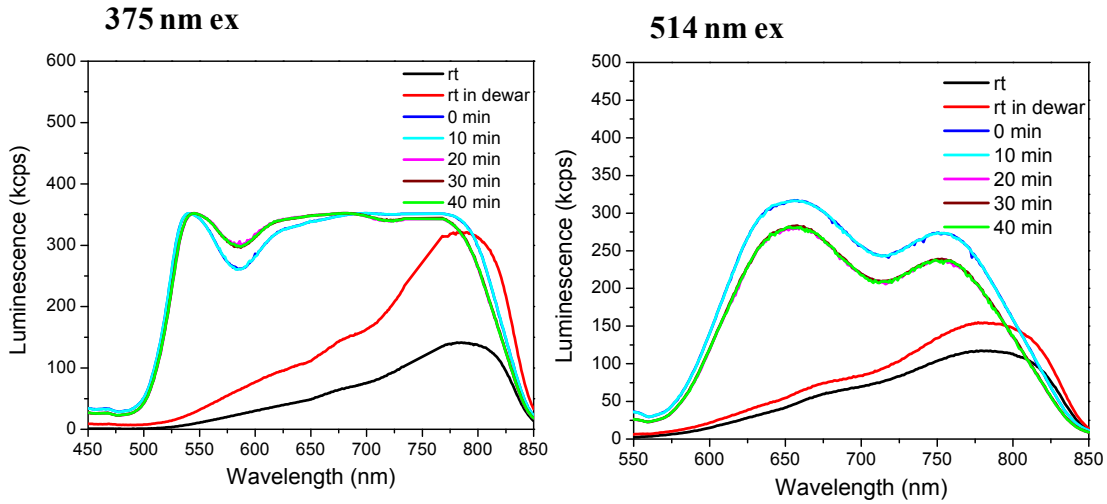

Figure 4.19 Emission spectra of $Au_{15}(SG)_{13}$ at cryogenic temperature (left panel 375 nm excitation, right panel 514 nm excitation). The cryogenic data has been scaled 150 times (for 375 nm excitation) and 50 times (for 514 nm excitation).

4.3.8 Time resolved fluorescence of Au nanoclusters

The time resolved measurement of some of the reported Au_{25} nanoclusters revealed that these nanoclusters have a very short lifetime of few nano second to maximum of hundreds of nano seconds. The synthesis of these series of Au_{25} nanoclusters with different ligands and the different core-size isolated in our work and there steady state fluorescence study motivated us to study their decay kinetics. For the lifetime measurement, the time scale was varied from 200 ns to 10 µs to get the decay-kinetics of these nanoclusters. The lifetime measurement for $Au_{15}(SG)_{13}$ and $Au_{18}(SG)_{14}$ nanoclusters is shown in figure 4.20. The lifetime was measured for 10 µs and then 4-exponential was fitted in the curve. The curve fitting resulted to a perfect fit with the χ^2 value of 1.06 and 1.08 for both the decay curve for $Au_{15}(SG)_{13}$ and $Au_{18}(SG)_{14}$ nanoclusters respectively. The channel was changed (from 1k to 8k) to get more data point to get the better curve fitting and the lifetime value was averaged for all those fitting. The $Au_{15}(SG)_{13}$ nanoclusters showed four lifetime of 19 ns, 110 ns, 440 ns, and 1.7 µs. This was the first observation of such a high lifetime from these small nanoclusters. Similarly for $Au_{18}(SG)_{14}$ nanoclusters the lifetime observed after the 4-exp fit was 10 ns, 140 ns, 470 ns, and 1.6 µs.

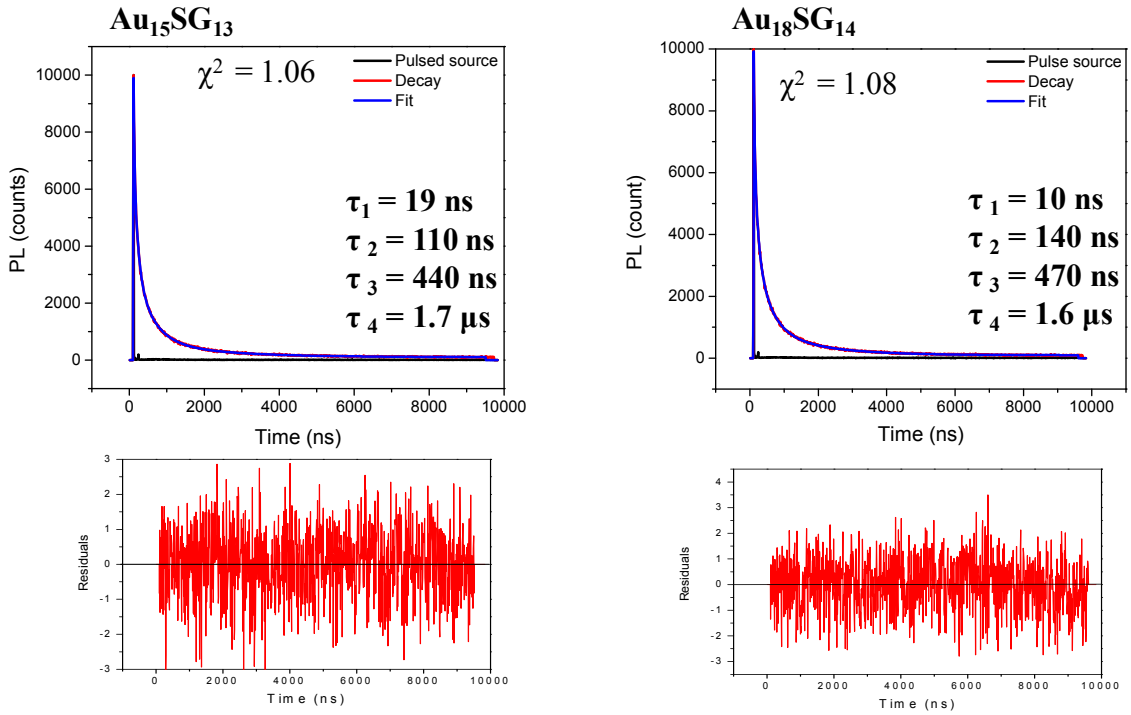

Figure 4.20 Fluorescence decay profile of $Au_{15}SG_{13}$ and $Au_{18}SG_{14}$ nanoclusters (excitation 375 nm, 1.1 nm pulse; emission monitored at 700 nm). The blue curve is the exponential fit to the decay profile; bottom red curve shows the residual of fitting.

For Au_{25} capped with water-soluble ligand (SG and Capt) the time-resolved measurement showed the presence of both the shorter ns lifetime component and the longer lifetime component. For $Au_{25}(Capt)_{18}$ nanoclusters the longer lifetime (μs) component has high amplitude which shows that the $Au_{25}(Capt)_{18}$ cluster relaxation has much longer lifetime than any other reported Au_{25} nanoclusters. The lifetime data is shown in figure 4.21. The 4-exp curve fitting of the decay profile resulted to the perfect fit with a χ^2 value of 0.98 and 1.16 for $Au_{25}(SG)_{18}$ and $Au_{25}(Capt)_{18}$ respectively. For $Au_{25}(SG)_{18}$ the lifetime values observed were 5 ns, 140 ns, 340 ns, and 1.6 μs with shorter lifetime component has dominant amplitude than the longer lifetime. For $Au_{25}(Capt)_{18}$ nanoclusters the lifetime value observed were 15 ns, 95 ns, 390 ns and 1.7 μs as shown in figure 4.21 right panel.

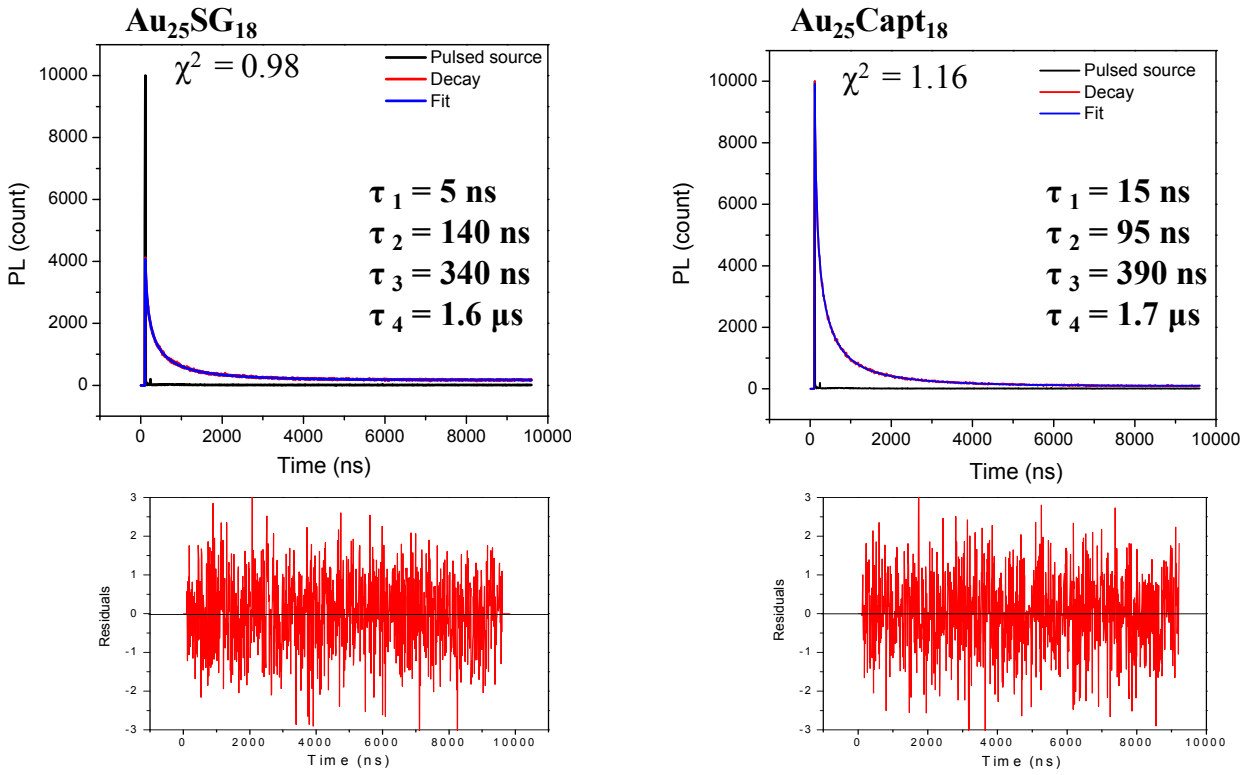

Figure 4.21 Fluorescence decay profile of $Au_{25}SG_{18}$ and $Au_{25}Capt_{18}$ nanoclusters (excitation 375 nm, 1.1 nm pulse; emission monitored at 700 nm). The blue curve is the exponential fit to the decay profile; bottom red curve shows the residual of fitting.

The lifetime measurement for $Au_{25}(PET)_{18}$ clusters has been reported by Wu *et al.*[25] and the lifetime value observed was in the range of few nanosecond to ~100 ns. In our measurement with the change of time scale from 200 ns to 1 μs, we never observed any longer lifetime. Therefore,

our result was consistent with the previous work. For $Au_{25}(PET^*)_{18}$ nanoclusters the lifetime measurement revealed that there is presence of higher lifetime component (340 nm) along with the lower lifetime components of few nanoseconds. The lifetime data for $Au_{25}(PET)_{18}$ and $Au_{25}(PET^*)_{18}$ nanoclusters is shown in figure 4.22 with the 3-exponential and 4-exponential fit to the decay curve with the χ^2 value of 1.31 and 1.26 respectively. The $Au_{25}(PET)_{18}$ showed the lifetime value of 7 ns, 85 ns, and 130 ns while the $Au_{25}(PET^*)_{18}$ nanoclusters showed the lifetime value of 8 ns, 50 ns, 99 ns, and 340 ns. The decay profile, prompt, fit to the curve, and the residual of fitting is shown in figure 4.22.

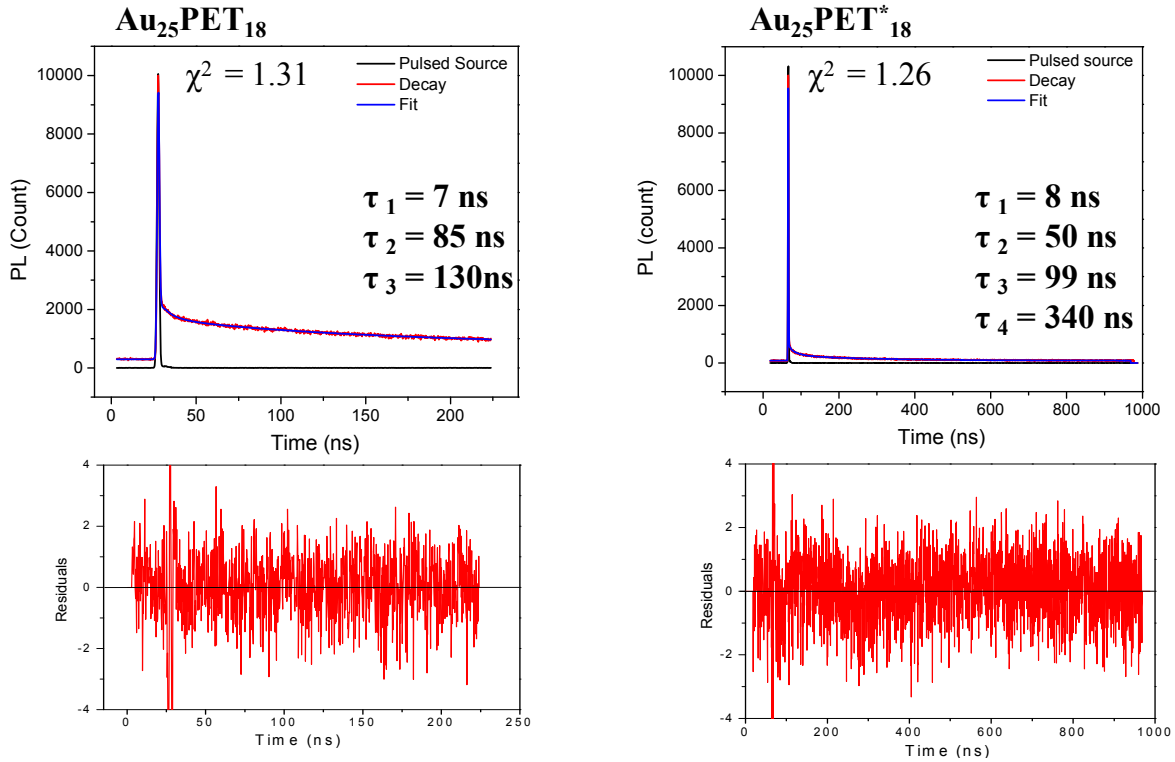

Figure 4.22 Fluorescence decay profile of $Au_{25}PET_{18}$ and $Au_{25}PET^*_{18}$ nanoclusters (excitation 375 nm, 1.1 nm pulse; emission monitored at 700 nm). The blue curve is the exponential fit to the decay profile; bottom red curve shows the residual of fitting.

4.4 Summary

The steady state study of the fluorescence properties of Au nanoclusters capped with different ligands and different core size revealed that even by the change of ligand the fluorescence properties changes dramatically. This observation was in quite contrast to the previous study of

the fluorescence properties of Au nanoclusters with few atoms. Also, our experiments revealed that the core size of the nanoclusters could not define the emission range which clearly contradicts the earlier studies. Previous studies claimed that emission maxima shift to higher wavelength by the increase of core-size. The lifetime measurement of the Au nanoclusters capped with different ligands (Au_{25}) and with varying core size revealed the ligand dependence on the decay kinetics of these nanoclusters. Theoretical studies of Au_{25} nanoclusters have revealed that the core-shell structure of the Au_{25} nanoclusters explains the shorter and the longer lifetime values. The shorter lifetime of few nanoseconds to ~ 100 ns is due to the relaxation inside the core, while longer lifetime of hundreds of nanosecond to μs is due to the relaxation from the staple motif (Shell). The structure of Au_{15} and Au_{18} nanoclusters is unknown but theoretical studies have revealed that both these clusters should have core-shell structure in order to get the appropriate geometric and electronic shell closing. This explains the longer lifetime component observed in both the nanoclusters. Therefore, the electronic effect of the ligand, which contributes to the relaxation dynamics of these nanoclusters from the staple motif to the core, is responsible for the longer lifetime (μs). The study of the decay kinetics at other excitation wavelength will shed more light into their decay kinetics.

4.5 References

1) Kreibig, U.; Vollmer, M. *Springer Series Mate* **1995**, *25*.
2) Ashcroft, N. W.; Mermin, N. D. *Solid State Physics*, Holt, Rinehart and Winston, New York, **1976**
3) Zheng, J.; Nicovich, P. R.; Dickson, R. M. *Annu. Rev. Phys. Chem.* **2007**, *58*, 409-431.
4) Shang, L.; Dong, S.; Nienhaus, G. U. *Nano Today* **2011**, *6*, 401-418.
5) Díez, I.; Ras, R. H. *Nanoscale* **2011**, *3*, 1963-1970.
6) Mooradian, A. *Phys. Rev. Lett.* **1969**, *22*, 185-187.
7) Boyd, G.; Yu, Z.; Shen, Y. *Phys. Rev. B* **1986**, *33*, 7923-7936.
8) Wilcoxon, J.; Martin, J.; Parsapour, F.; Wiedenman, B.; Kelley, D. *J. Chem. Phys.* **1998**, *108*, 9137.
9) Bigioni, T.; Whetten, R.; Dag, Ö. *J. Phys. Chem. B* **2000**, *104*, 6983-6986.
10) Huang, T.; Murray, R. W. *J. Phys. Chem. B* **2001**, *105*, 12498-12502.
11) Link, S.; Beeby, A.; FitzGerald, S.; El-Sayed, M. A.; Schaaff, T. G.; Whetten, R. L. *J. Phys. Chem. B* **2002**, *106*, 3410-3415.
12) Schaaff, T. G.; Knight, G.; Shafigullin, M. N.; Borkman, R. F.; Whetten, R. L. *J. Phys. Chem. B* **1998**, *102*, 10643-10646.
13) Sanchez, A.; Abbet, S.; Heiz, U.; Schneider, W.-D.; Häkkinen, H.; Barnett, R.; Landman, U. *J. Phys. Chem. A* **1999**, *103*, 9573-9578.
14) Fedrigo, S.; Harbich, W.; Buttet, J. *J. Chem. Phys.* **1993**, *99*, 5712-5717.
15) Zheng, J.; Petty, J. T.; Dickson, R. M. *J. Am. Chem. Soc.* **2003**, *125*, 7780-7781.
16) Zheng, J.; Zhang, C.; Dickson, R. M. *Phys. Rev. Lett.* **2004**, *93*, 077402.
17) Duan, H.; Nie, S. *J. Am. Chem. Soc.* **2007**, *129*, 2412-2413.
18) Xavier, P. L.; Chaudhari, K.; Verma, P. K.; Pal, S. K.; Pradeep, T. *Nanoscale* 2010, *2*, 2769-2776.
19) Zhou, R.; Shi, M.; Chen, X.; Wang, M.; Chen, H. *Chem - Eur. J.* **2009**, *15*, 4944-4951.
20) Jin, R.; Egusa, S.; Scherer, N. F. *J. Am. Chem. Soc.* **2004**, *126*, 9900-9901.
21) Santiago González, B.; Rodríguez, M. a. J.; Blanco, C.; Rivas, J.; López-Quintela, M. A.; Martinho, J. M. G. *Nano Lett.* **2010**, *10*, 4217-4221.
22) Clemenger, K. *Phys. Rev. B* **1985**, *32*, 1359-1362.
23) Negishi, Y.; Nobusada, K.; Tsukuda, T. *J. Am. Chem. Soc.* **2005**, *127*, 5261-5270.
24) Devadas, M. S.; Kim, J.; Sinn, E.; Lee, D.; Goodson III, T.; Ramakrishna, G. *J. Phys. Chem. C* **2010**, *114*, 22417-22423.
25) Wu, Z.; Jin, R. *Nano lett.* **2010**, *10*, 2568-2573.
26) Muhammed, M. A. H.; Shaw, A. K.; Pal, S. K.; Pradeep, T. *J. Phys. Chem. C* **2008**, *112*, 14324-14330.

27) Kumar, S.; Jin, R. *Nanoscale* **2012**, *4*, 4222-4227.

Chapter 5

Ongoing Projects and Future Directions

5.1 Bridging the gap between nanoclusters and nanocrystals

The recent development in the field of noble metals nanoclusters has revealed different sized nanoclusters ranging from sub-nanometer to the region where plasmonic properties becomes dominant.[1-3] Researchers have reported a series of nanoclusters of gold and silver with few atoms to several hundred atoms.[4-12] However, the exact size and number of atoms where the transition from molecular behavior to plasmonic behavior occurs still remains unknown. Using silver-thiolate as a model system, we aim to determine the exact size and atom count Ag_n where the transition from quantum to classical behavior occurs. For this purpose, we have recently synthesized a series of Ag nanoclusters capped with captopril as shown in scheme 5.1.

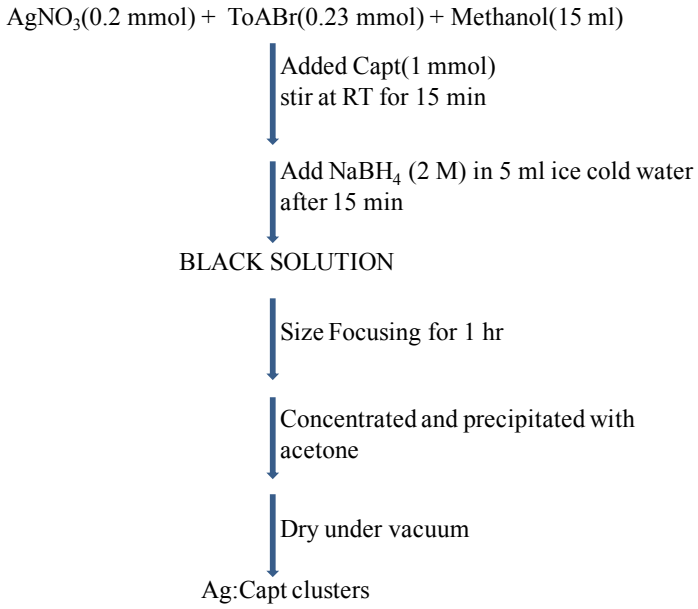

Scheme 5.1 Synthesis of Ag:Capt nanoclusters

The as-synthesized clusters were subjected to PAGE separation, which resulted in separation of these nanoclusters in seven distinct bands, with smaller size nanoclusters travelling farthest. These nanoclusters are isolated from the gel by the method described in chapter 2. Figure 5.1 shows the gel image and the optical absorption spectra of the gel-isolated nanoclusters. The SPR peak of silver nanoparticles (size >2 nm) lies ~ 430 nm. As the size of the nanoparticles increase,

the plasmon peak becomes broadens and the peak shifts towards red. In this case, we observed that despite the size of band 1 being smallest, the peak is quite broad with FWHM of 300 nm. As the size of the nanoclusters increases, the absorption peak becomes narrow and the peak shows a blue shift. This is clear distinction from the bigger nanoparticles or nanocrystals.

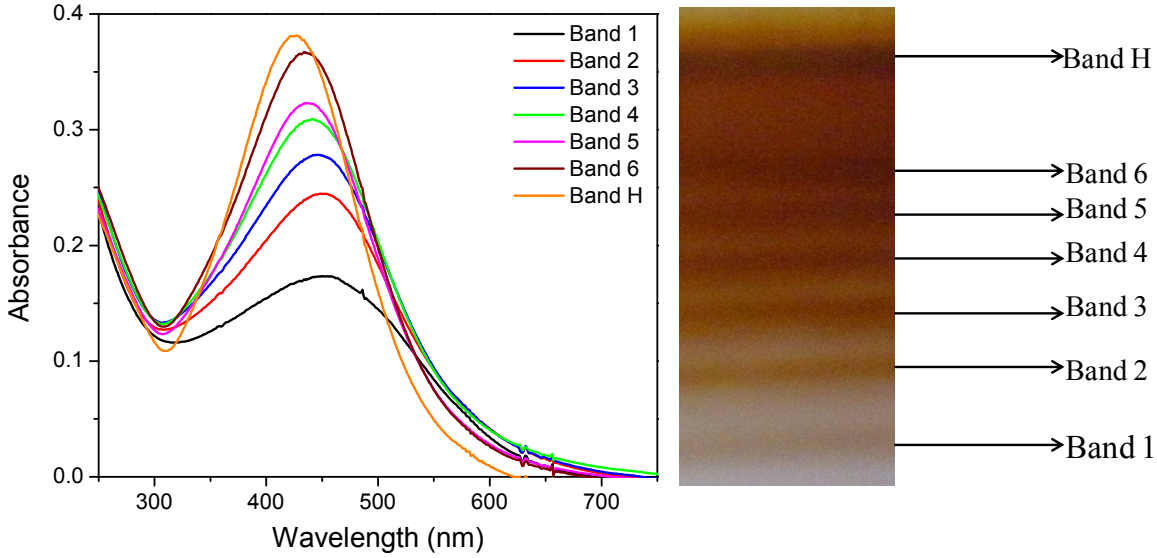

Figure 5.1 Absorbance spectra of the gel-isolated Ag:Capt nanoclusters (left panel), and PAGE image of the separated nanoclusters (right panel). Band H refers to the highest band among all isolated bands.

5.1.1 Mass determination of Ag:Capt clusters

To determine the exact number of atoms in the nanoclusters, we need to get the precise mass-spectrometric determination of the nanoclusters. For this purpose, MALDI-mass spectrometry was used. The nanoclusters were dissolved in water and then combined with matrix (2,4-dihydroxy benzoic acid (DHB)) in 1:1 ratio and then 4-5 µl of this mixture was deposited on the MALDI plate to co-crystallize the nanoclusters with the matrix. The nanoclusters were then analyzed by MALDI-mass spectrometry. The MALDI-MS spectrum of the bands 1-6 is shown in Figure 5.2. The MALDI mass spectrum showed a clear progression of size with increasing mass as we move from band 1-6. For some spectrum the progressive peaks were observed in periodic order. These peaks correspond to the recombination of the nanoclusters in the presence of laser power as dimer, trimer, so on. The mass analysis revealed that band 1 should have ~ 250-300 Ag atoms, while band 6 can have up to 700-800 silver atoms. As our calculation in chapter 1 has revealed that for ~ 480 atoms of gold, the plasmonic properties becomes dominant and visible.

Since Ag has the same bulk lattice constant and ~ similar size than Au, we speculate that band 4 or band 5 would be the mass at which plasmonic property will be dominant and the transition from molecular behavior to plasmonic behavior will occur. Although, the MALDI spectrum gives an estimate of their mass-range, the precise mass i.e. the exact number of silver and the captopril ligand in the cluster composition can only be determined by ESI-MS. The investigations using ESI-MS is still ongoing.

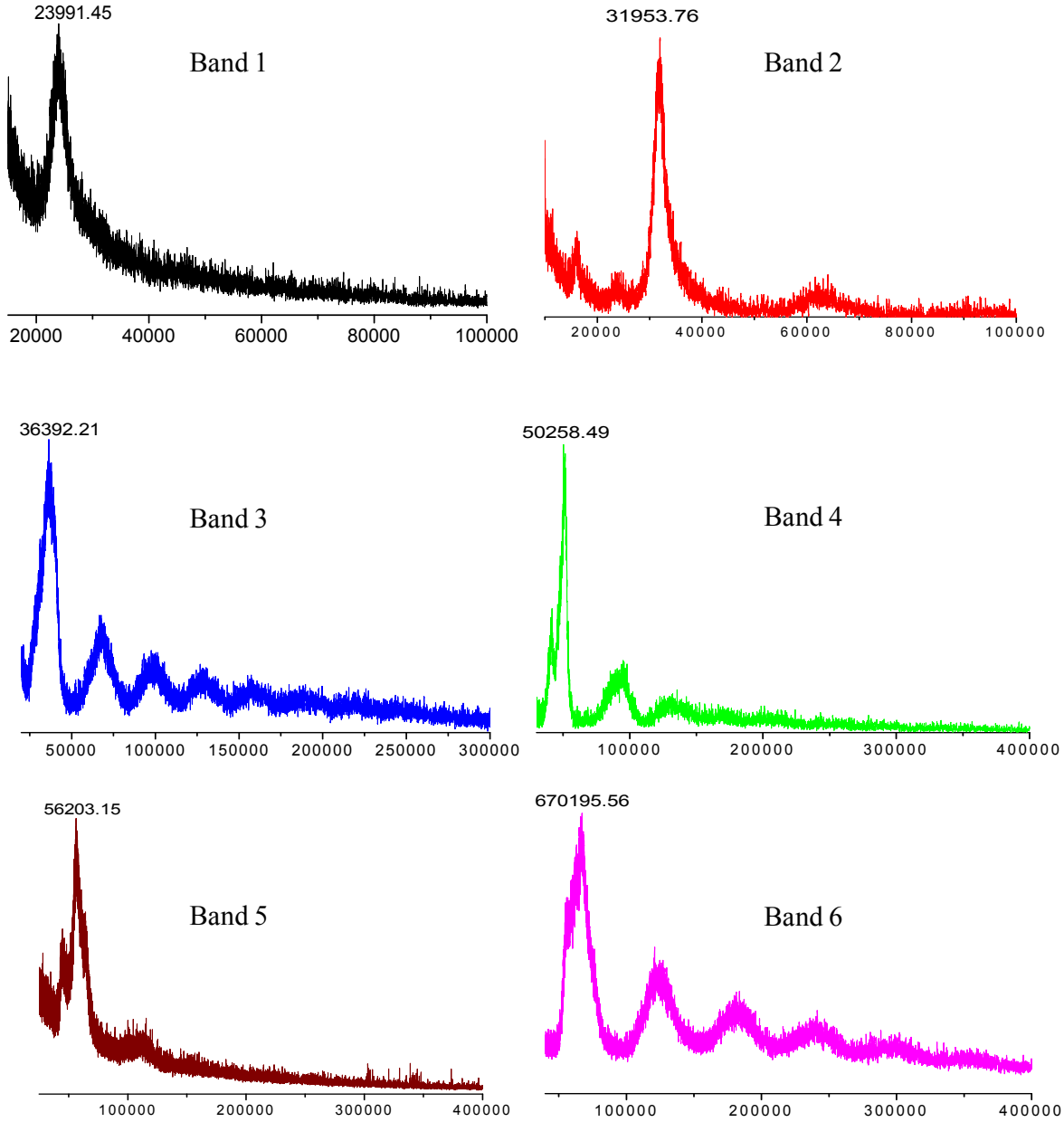

Figure 5.2 MALDI- mass spectrum of band 1-6. The progression of peaks in the spectra is due to the combination of the clusters.

5.1.2 Size estimation of Ag:Capt clusters

The size of the nanoclusters can be evaluated by TEM. The small size of these nanoclusters and lower Z contrast of the Ag in comparison to the Au makes it relatively more challenging. The other issue associated with TEM image is that these small nanoclusters tend to aggregate in the presence of high voltage electron beam. Hence, the exact size estimation becomes a challenge. To address this issue, we decided to do the powder X-ray diffraction (*p*-XRD) of these nanoclusters. The plasmonic nanoparticles shows fcc arrangement and as the size decreases, the *p*-XRD peak of the nanoparticles becomes broader. The *p*-XRD data combined with the TEM will give the exact estimation of the nanocluster size. Figure 5.3 shows the TEM image of biggest size Ag:capt nanoclusters (Band H). The TEM image shows that most of the nanoclusters are in the the size range of ~ 2 nm with few of them aggregated by the electron beam to show slightly bigger sizes. The high-resolution TEM (HR-TEM) image of these nanoclusters would be quite informative, as it will give the idea of lattice plains and the closed packing in the Ag nanoclusters. The HR-TEM of these nanoclusters is still under progress.

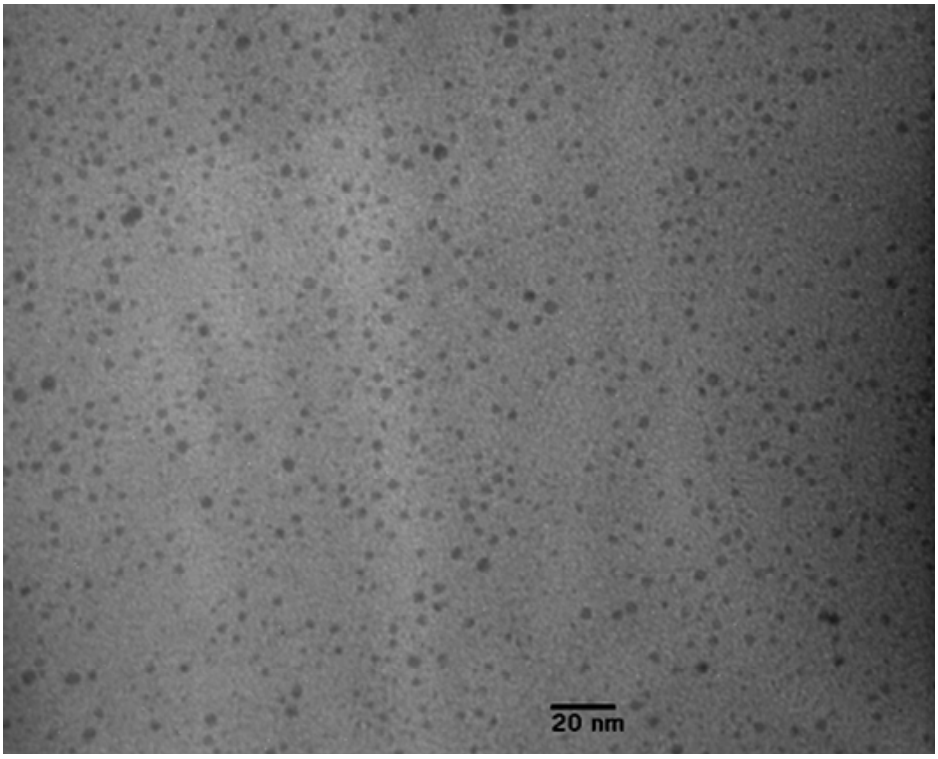

Figure 5.3 TEM image of band H

The *p*-XRD of Band H is shown in figure 5.4 left panel. The peak at 2θ values of 37.5, 64, and 76 correspond to the fcc pattern of silver. The broad peak signifies the smaller size of these nanoclusters. The *p*-XRD of Band 6 is shown in figure 5.4 right panel. The further broadening of the fcc peak can be clearly seen in case of band 6. However, the peak position in band 6 was found to be consistent with band H and the fcc arrangement of silver. The *p*-XRD of the lower bands is still in progress. As the size distribution of the synthesis is focused towards bigger particles, the yield of the lower bands is considerably low, this makes the *p*-XRD measurement quite challenging, as at least few mg (20-50 mg) of the sample is required.

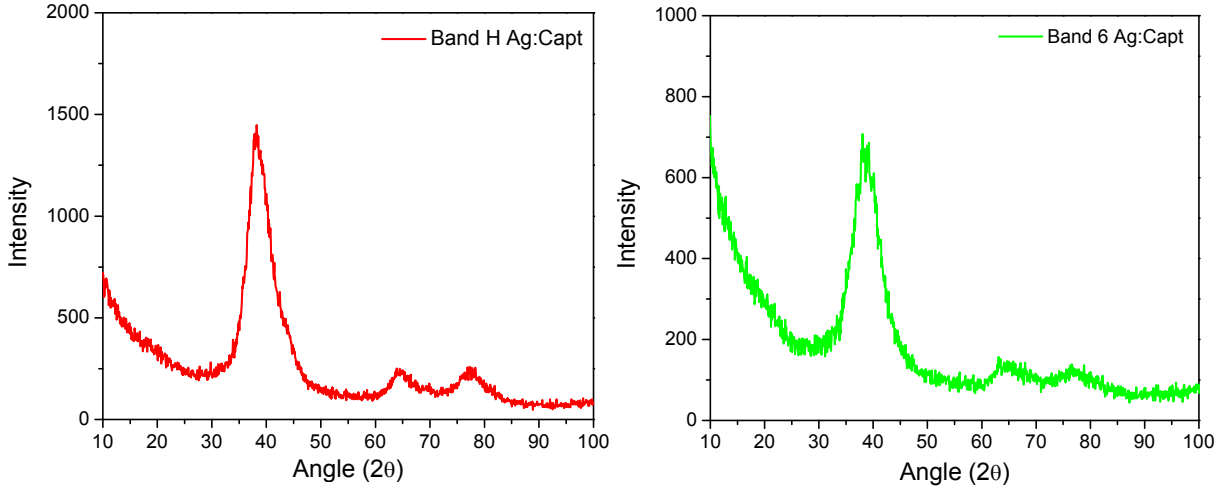

Figure 5.4 p-XRD pattern of band H (left panel) and band 6 (right panel). The peak positions correspond to the fcc lattice arrangement of silver.

5.1.3 Optical properties of Ag:Capt clusters

The absorption spectra of these Ag:Capt nanoclusters closely resemble to the plasmonic Ag nanoparticles. This can be misleading as the sizes of some of these nanoclusters are < 2 nm. To prove that these nanoclusters are non-plasmonic, and the plasmonic properties appear at a certain size, the fluorescence lifetime of these nanoclusters clusters can be calculated. For plasmonic nanoparticles, the decay-lifetime is in the range of nanoseconds to picoseconds, so the lifetime measurement will reveal that at what band size the plasmonic property dominates the molecular properties. The emission spectra (excitation wavelength 300 nm) of these nanoclusters are shown in figure 5.5. The emission peak broadens as the size of these nanoclusters increase. The lifetime measurement is still under progress.

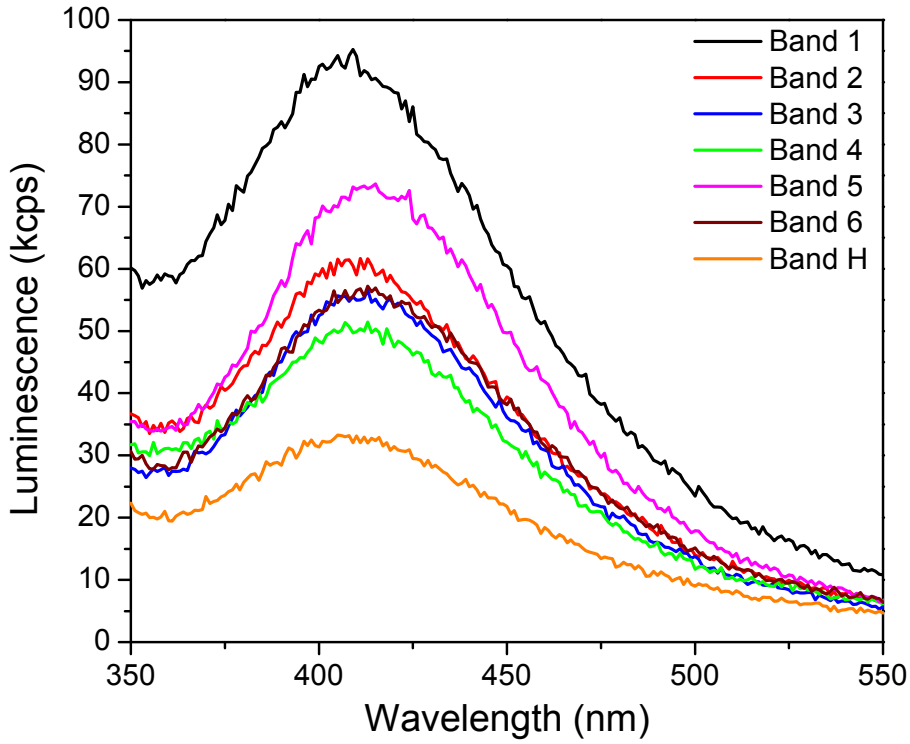

Figure 5.5 Emission spectra of the Ag:Capt nanoclusters. The excitation wavelength is 300 nm.

5.2 Singlet Oxygen Production by Water-Soluble $Au_{25}(Capt)_{18}^-$ clusters

5.2.1 Introduction

Photodynamic therapy (PDT) is a relatively new method for cancer treatment, where tumor cells are destroyed by light-induced, local production of a reactive oxygen species (ROS) such as singlet oxygen ($^1O_2$) and superoxide($O_2^{\cdot -}$) via photosensitizers.[13-19] It is considered that singlet oxygen is the primary cytotoxic agent responsible for PDT. The development of singlet oxygen photosensitizers to produce highly reactive oxygen species is a key step for effective PDT. In recent years, an increasing number of researchers have considered the possibility of nanomaterials as singlet oxygen photosensitizers such as semiconductor quantum dots (QDs), fullerene C_{60}, metal nanoparticles, and QDs conjugated with aromatic photosensitizers. Unfortunately, most photosensitizers have some major drawbacks, including poor water solubility, toxicity, instability, and ineffective excitation wavelengths for the tissue penetration.[20-26]

Recently, significant progress has been made in the synthesis of atomically precise thiolate-protected gold nanoclusters (denoted as $Au_n(SR)_m$, where SR refers to thiolate ligand), such as $Au_{25}(SR)_{18}$, $Au_{38}(SR)_{24}$, $Au_{102}(SR)_{44,}$ and $Au_{144}(SR)_{60}$.[1,27,28] The photoluminescent properties of $Au_n(SR)_m$ render such nanoclusters as promising imaging and sensing agents. However, till now there have been no reports on the exploitation of $Au_n(SR)_m$ nanoclusters as potential photosensitizers toward PDT. Herein we demonstrate that singlet oxygen can be produced through the direct photosensitization by $Au_{25}(Capt)_{18}^-$clusters (Capt = captopril) without the presence of any organic photosensitizers. The experimental evidence includes (1) sensitive probe for singlet oxygen, namely, diaminobenzidine (DAB), (2) quenching of singlet oxygen production by histidine as the efficient scavenger for singlet oxygen, and (3) enhancement of singlet oxygen production in D_2O.

5.2.2 Detection of singlet oxygen by chemical probe detection

Water-soluble DAB(2,4-diamino benzidine) was employed as a singlet oxygen probe in this study.[25-27] For the DAB method, a 10 mM stock solution of DAB in DMF was prepared, and then added to 1 mL aqueous solution (H_2O or D_2O) of $Au_{25}(Capt)_{18}^-$, to give final concentrations of $Au_{25}(Capt)_{18}^-$ and DAB of 30–40 μM and 500 μM, respectively. The solution was purged with air for approximately 10 min immediately prior to measurement. The solutions were then irradiated with a light-emitting diode (LED) at a power of 50 mW (532 nm, Green laser). The adsorption spectra were recorded after different periods of light irradiation. To see the effect of dissolved oxygen, pure N_2 gas was bubbled through the D_2O solution of $Au_{25}(Capt)_{18}^-$ and DAB for 1 h. The solution was then irradiated with light for 10 min in a N_2-filled glove bag.

5.2. 3. Results and Discussion

Chemical trapping detection methods were adopted for assessing the generation of singlet oxygen by $Au_{25}(Capt)_{18}^-$. Depending on the particular trapping species, the chemical trapping of singlet oxygen can be monitored by changes in fluorescence, absorption, or electron spin resonance (EPR). In the present study, DAB was employed to examine the ability of $Au_{25}(Capt)_{18}^-$ to generate singlet oxygen in aqueous media. Although the exact mechanism by which the oxidation of DAB occurs is not clear, it is known that singlet oxygen can directly react with DAB to form a DAB polymer as the oxidation product. The reaction with singlet oxygen can be monitored by the changes in absorption spectra in the UV-visible region. DAB has been

demonstrated to have high selectivity towards singlet oxygen, and does not show any noticeable response towards hydroxyl radicals or superoxide.

Figure 5.6 shows the absorption spectra of DAB in a D_2O solution of $Au_{25}(Capt)_{18}^-$. D_2O was employed as the solvent because of the longer lifetime of singlet oxygen (20–58 μs) in comparison to H_2O (~2 μs),[29,30] leading to a greater probability of interaction with DAB. The detection experiment was conducted for 2 h, with three different regimes used: (I) 0–60 min, under darkness (Fig 5.6 a), (II) 60–90 min, irradiation at 532 nm (Fig 5.6 b), and (III) 90–120 min, irradiation at 532 nm in the presence of histidine (Fig 5.6 c). The spectrum shown in Fig 5.6 (a) was acquired after the solution was purged with air, sealed with a cap, and then kept in darkness under an air atmosphere for 60 min.

Under darkness, there was no change in the absorption spectra of DAB in the presence of $Au_{25}(Capt)_{18}^-$ (Fig 5.6 a). This indicates that the trapping species was not oxidized in the air atmosphere, and therefore, there was no photoexcited $Au_{25}(Capt)_{18}^-$ present. However, during the 532 nm light irradiation, the absorbance below 650 nm can be seen to dramatically increase over time due to DAB oxidation (Fig 5.6 b). This result indicates that the photoexcited $Au_{25}(Capt)_{18}^-$ was able to generate singlet oxygen. On the other hand, in the absence of $Au_{25}(Capt)_{18}^-$, there was no evident change in the absorbance spectrum of DAB with light irradiation (Fig 5.6 d), confirming that the combination of $Au_{25}(Capt)_{18}^-$ and light irradiation was responsible for the changes. If the singlet oxygen generated by the $Au_{25}(Capt)_{18}^-$ causes the oxidation of DAB, the change in the rate of DAB absorbance would depend on the concentration of oxygen dissolved in the D_2O. Removal of such oxygen by N_2 purging resulted in significantly smaller changes in the absorbance spectrum. It should be noted that there was still a slight change in the absorbance of DAB, even in the N_2 atmosphere, indicating that there was a small contribution from a photocatalytic effect of $Au_{25}(Capt)_{18}^-$ without the involvement of oxygen.

In order to further confirm the generation of singlet oxygen on the photoexcitation of $Au_{25}(Capt)_{18}^-$, a scavenger method was employed to inhibit the generation of singlet oxygen. It has been well established that histidine is a specific scavenger that can effectively inhibit the generation of singlet oxygen.[31,32] Figure 5.6 (c) shows the absorption spectra of a DAB-containing solution of $Au_{25}(Capt)_{18}^-$ in D_2O in the presence of histidine, with almost no change evident on increasing irradiation time. It is clear that the histidine effectively inhibited the

oxidation of the DAB, supporting the hypothesis that the activated oxygen species generated by the $Au_{25}(Capt)_{18}^-$ is in fact singlet oxygen.

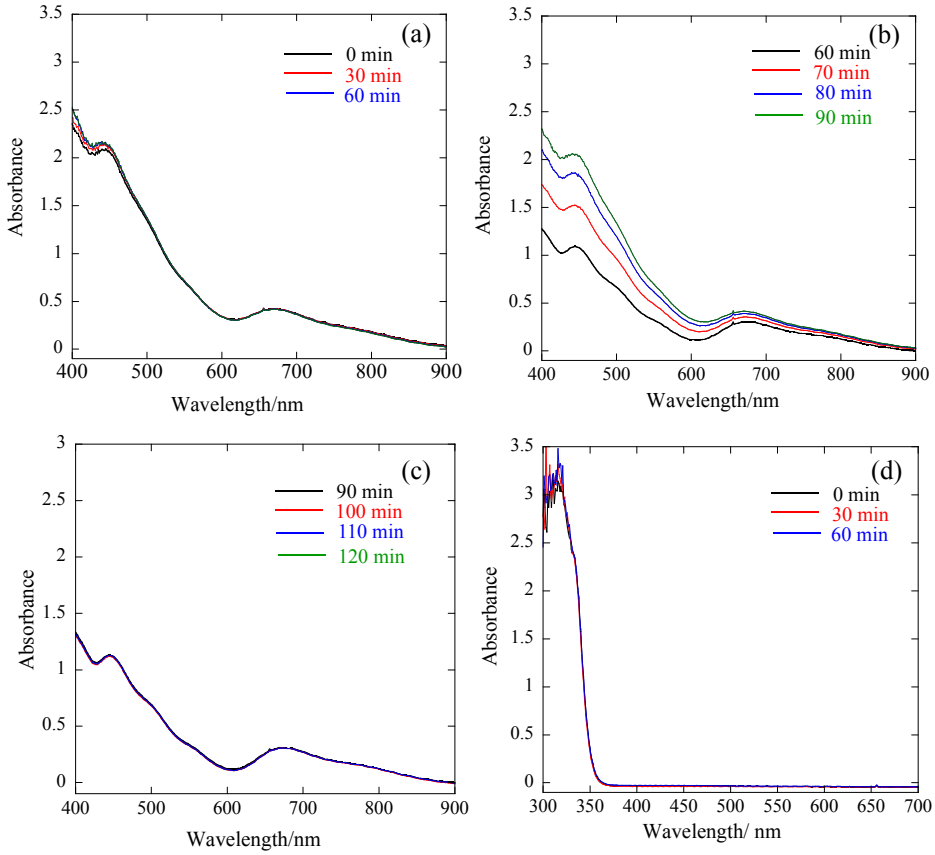

Figure 5.6 Absorption spectra of a DAB-containing solution of $Au_{25}(Capt)_{18}^-$ in D_2O. (a) 0–60 min, under darkness, (b) 60–90 min, light irradiation at 532 nm (50 mW), and (c) 90–120 min, light irradiation at 532 nm (50 mW) in the presence of histidine (20 mM). (d) Absorption spectra of DAB in a D_2O solution in the absence of $Au_{25}(Capt)_{18}^-$, irradiation at 532 nm (50 mW) for 60 min. $[Au_{25}]$ = 30 μM, [DAB] = 500 μM.

The changes in absorbance at 445 nm of DAB-containing solutions of $Au_{25}(Capt)_{18}^-$ are shown in Figure 5.7. It can be seen that in region I, where there is no light irradiation, there is no change in DAB absorbance. In region II, there is an increase in absorbance evident on irradiation at 532 nm due to the generation of singlet oxygen by $Au_{25}(Capt)_{18}^-$. Finally, in region III, there is almost no change in absorbance of DAB because of the inhibition of singlet oxygen by the histidine scavenger. In addition, the use of H_2O in place of D_2O reduced the interaction between DAB and singlet oxygen because of the shorter lifetime in H_2O. This observation was further

evidence of the generation of singlet oxygen by $Au_{25}(Capt)_{18}^{-}$. From the above results, it can be concluded that singlet oxygen is produced via direct photosensitization by $Au_{25}(Capt)_{18}^{-}$ in aqueous media.

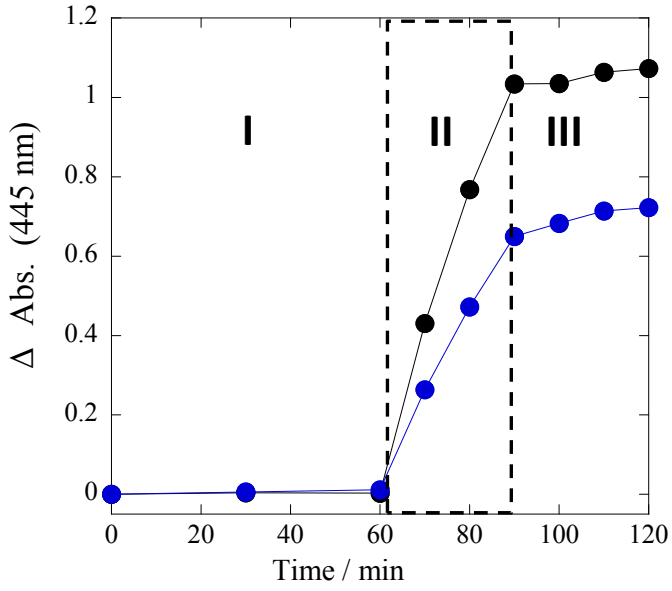

Figure 5.7 Changes in absorbance at 445 nm of a DAB-containing solution of $Au_{25}(Capt)_{18}^{-}$ in D_2O (black) and H_2O (blue). Region I: Darkness; Region II: Light irradiation; Region III: Addition of histidine scavenger.

Therefore, we have demonstrated that singlet oxygen can be produced through the direct photosensitization of $Au_{25}(Capt)_{18}^{-}$ clusters without using organic photosensitizers under visible/ near-IR irradiation. Singlet oxygen was successfully detected using a singlet oxygen probe. Enhancement of singlet oxygen production in D_2O compared to that in H_2O was observed, and quenching of production was shown to occur on bubbling N_2 gas through the solution. The efficiency of singlet oxygen generation by other Au nanoclusters will be studied. Mechanistic insights in the singlet oxygen generation will be developed. Owing to the unique properties of singlet oxygen, this study has far reaching implications, not only for PDT but also in broader fields of interest like medicine, organic synthesis, and polymer chemistry.

5.3 Quenching behaviors of Gold Nanoclusters

An interesting property of metal nanoparticles (NPs) is their ability to affect the fluorescence properties of different molecules.[33-36] Several studies over the years have shown that different

nanoparticles can either quench or enhance the fluorescence of different dye molecules. These effects depend on several factors such as the identity of the metal and the dye, the distance between them and the relative orientation between the dye and the nanoparticles.[37,38] Although nanoparticles of larger size (>2nm) have been extensively studied for their effects on fluorescence properties of dye molecules, much less studies have been done to smaller nanoparticles (<2nm) and also nanoclusters. Recently, comparison between the fluorescence quenching efficiencies of 4nm AuNP, 2nm AuNP and glutathione coated Au_{25} nanocluster by Chowdhury *et al* revealed striking difference between the fluorescence quenching properties of these three different particles.[39] For this study, several bis-intercalator dyes bound to 30mer duplex DNA was used as a fluorescence source (Figure 5.8 A). It was observed in this study that the 4nm AuNP was one order of magnitude more effective in quenching compared to the 2nm AuNP and Au_{25} nanocluster. Also, the 4nm AuNP showed significantly higher quenching of fluorescence when the dye has emission band overlapping the plasmonic band of the AuNP (Figure 5.8 B). However the 2nm AuNP showed an almost monotonic decrease in the quenching efficiency with decrease in the emission wavelength of the dye which can be explained by the NSET theory proposed by Strouse *et al* (Figure 5.8 C).[40-42] But the quenching efficiencies of the Au_{25} nanoclusters did not show any trend which could be related with either NSET theory or effect of spectral overlap (Figure 5.8 D). The Au_{25}NC showed highest quenching for YOYO-1/DNA complex and LOLO-1/DNA complex which have emission spectra separated from the discrete electronic transition band of the nanocluster.

From the initial study, it was quite clear that understanding the quenching behavior of the AuNCs require a new model different from larger nanoparticles. Since we have robust methods to synthesize atomically precise nanoclusters, we wanted to study the effect of different size of Au nanoclusters on the quenching efficiencies. We choose to use POPO-1, YOYO-1, YOYO-3 and TOTO-3 bound to double stranded DNA for these experiments. We have used five different nanoclusters namely, $Au_{15}SG_{13}$, $Au_{18}SG_{14}$, $Au_{25}SG_{18}$, $Au_{25}Capt_{18}$ and $Au_{38}SG_{24}$ for this study. For the quenching experiment 100 nM duplex DNA was annealed by heating to 95 $^{\circ}$C for 10 min followed by slow cooling to room temperature. Then 7 equivalent of the bis-intercalator dye was added to the solution and incubated overnight at room temperature. This was followed by the addition of various amounts of AuNCs, the resultant mixture was incubated for 30 min. After 30

min, the emission of the complex reached a stable value without any further change and then their emission spectra was recorded.

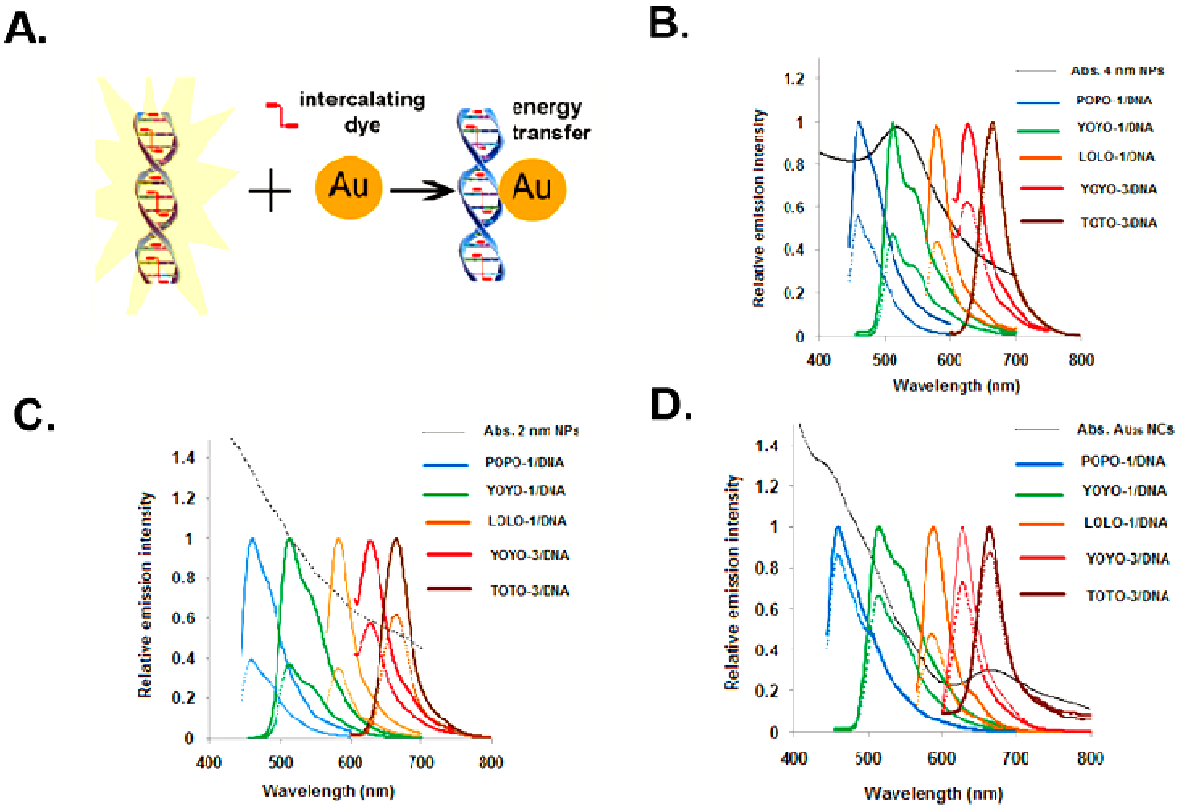

Figure 5.8 (A) The bis-intercalator dyes when complexed with DNA increases its fluorescence by large amount. (B) Absorption spectra of the 4nm AuNP and emission spectra of the different bis-intercalator dye complexed with duplex DNA. The YOYO-1 and LOLO-1 dyes have highest spectral overlap with the plasmon band of the AuNP show highest quenching. (C) Absorption spectra of the 2nm AuNP and the emission spectra of the different bis-intercalator dye complexed with duplex DNA. The quenching efficiency of this AuNP decreases with increase in the emission wavelength of the dye. (D) Absorption spectra of the Au_{25}NC and the emission spectra of the different bis-intercalator dye complexed with duplex DNA. The trend in the fluorescence quenching cannot be explained by either spectral overlap or NSET theory. Reproduced with permission from ref. 39. Copyright 2011 American Chemical Society.

The quenching efficiencies of the differents AuNCs was calculated using the Stern-Volmer plot which used the change in relative intensities of the DNA-dye complex with varying concentration of the AuNCs. The Stern-Volmer constants of the different AuNCs along with the 4nm AuNP are shown in Table 5.1. As discussed previously, all the AuNCs shows quenching efficiencies, which are an order of magnitude lower than that of the 4nm AuNP. The smallest

nanocluster $Au_{15}SG_{13}$ does not show any quenching for any of the intercalator dyes. The reason for not showing any quenching could be either electronic properties of the NC or it is also possible that due to the smallest size, it does not bind to the DNA duplex very effectively. Interestingly all the other nanoclusters showed highest quenching efficiencies for YOYO-1 dye/DNA complex. Also, the quenching efficiencies of the AuNCs for complexes emitting in the wavelength region >600nm was negligible. Although these experiments did not show any correlation between the size of the AuNCs and their quenching efficiencies, surprisingly one particular wavelength region (500-600nm) was more efficiently quenched compared to other wavelength regions. Although we do not have any particular explanation for this behavior, it could be due to some electronic properties of the AuNCs which are common to all the four different AuNCs used in this study.

Table 5.1 Collisional quenching constants of various dyes by different AuNCs

	1:7 POPO-1 dye/30 bp dsDNA	1:7 YOYO-1 dye/30 bp dsDNA	1:7 YOYO-3 dye/30 bp dsDNA	1:7 TOTO-3 dye/30 bp dsDNA
$Au_{25}(SG)_{18}$	.001	.014	.004	.005
$Au_{18}(SG)_{14}$	No quenching	.01	No quenching	No quenching
$Au_{15}(SG)_{13}$	No quenching	No quenching	No quenching	No quenching
$Au_{38}(SG)_{24}$	.005	.012	No quenching	No quenching
$Au_{25}(Capt)_{18}$	No quenching	.01	No quenching	No quenching
4nm Au np	.06	.2	.04	.01

Although the quenching behavior of the AuNCs could not be explained by any known theory, the binding behavior of the AuNCs to the duplex DNA could also be an important factor. Because both the duplex DNA and the AuNPs are negatively charged, it is not very well understood what is the binding mode between the DNA and AuNCs. Therefore, to eliminate the ambiguity of binding mode of the diierent AuNCs with the DNA duplex, we decided to perform similar quenching experiment with positively charged quantum dots (QDots). Due to the positive charge of the quantum dots, the interaction between AuNCs and the QDots are completely electrostatic. Therefore, it eliminates the problem of different binding mode of the AuNCs and the duplex DNA. Again, we choose to use four different quantum dots with absorption maxima at 450 nm, 525 nm, 600 nm and 665 nm spreading from the blue to red region of the visible spectrum (Figure 5.9).

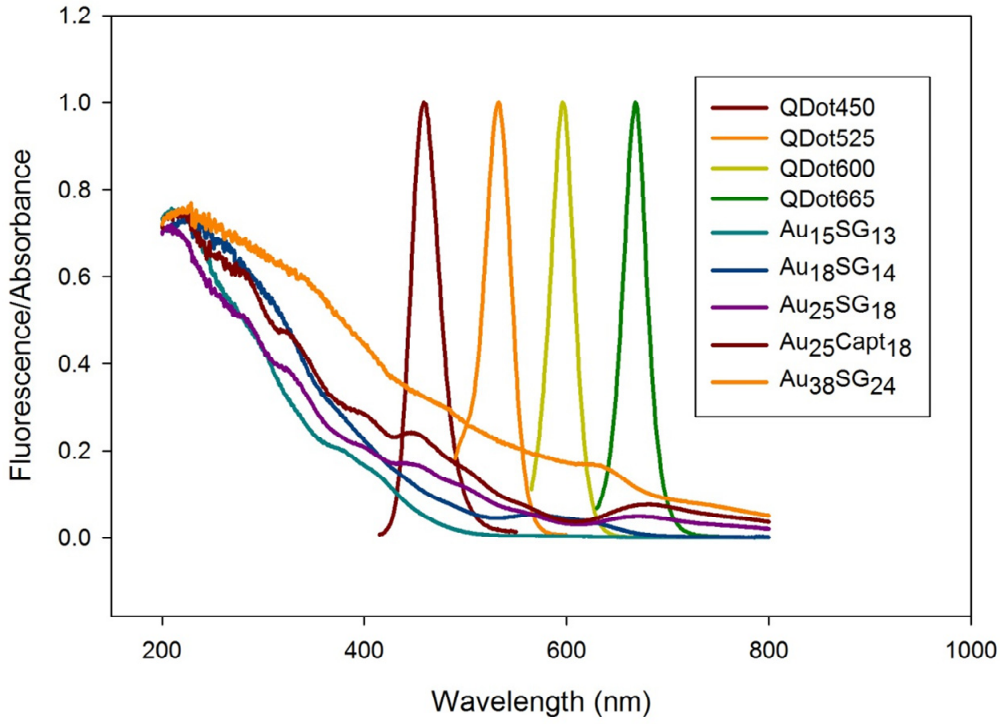

Figure 5.9 The emission spectra of the different QDots and the absorption spectra of the different AuNCs.

We have done some preliminary experiments for quenching of these QDots fluorescence with the AuNCs. One interesting observation was that similar to the DNA-dye complex, Au_{15} cluster does not show any quenching of the QDot fluorescence.

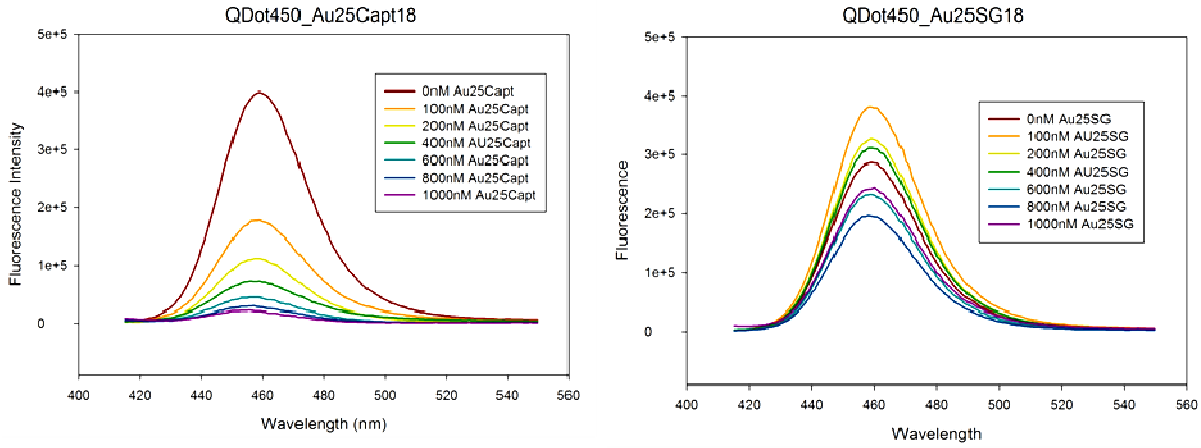

Figure 5.10 Fluorescence quenching of the QDot 450 by (A) $Au_{25}(Capt)_{18}$, and (B) $Au_{25}(SG)_{18}$ nanoclusters. The $Au_{25}(Capt)_{18}$ cluster quenches the fluorescence of the QDot 450 very effectively, whereas the $Au_{25}(SG)_{18}$ cluster is less effective in quenching.

However, the quenching of the QDot fluorescence by the other AuNCs were different. Again, the quenching efficiencies of the AuNCs were much lower compared to that of the 4 nM AuNP. The $Au_{25}(Capt)_{18}$ cluster very effectively quenched the QDot 450, whereas other clusters except $Au_{18}(SG)_{14}$ showed moderate quenching (Figure 5.10).

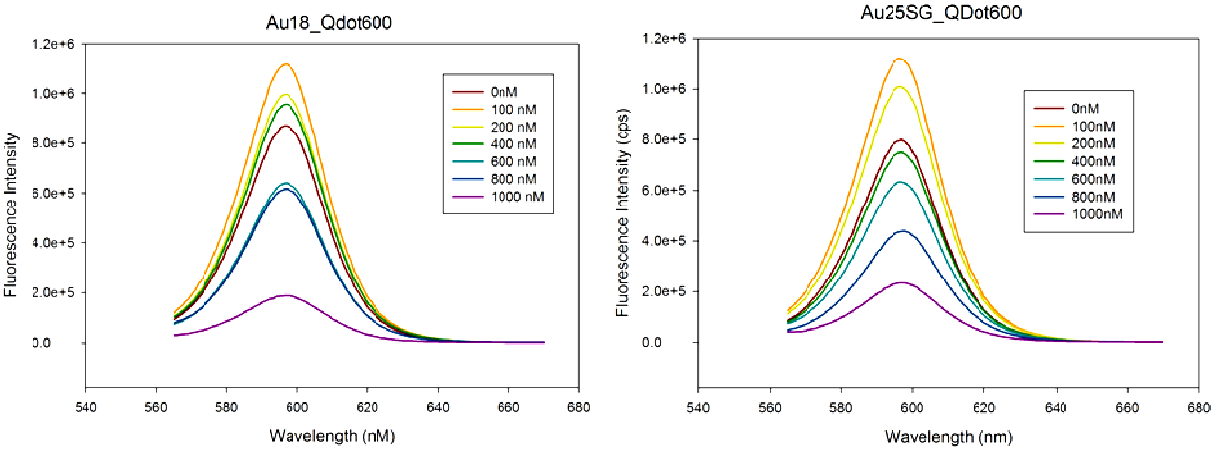

Figure 5.11 (A) Quenching of the QDot 600 fluorescence by Au_{18} nanocluster. (B) Concentration dependence of $Au_{25}(SG)_{18}$ nanoclusters on the fluorescence quenching of QDot 600.

Another important observation was that the $Au_{18}(SG)_{14}$ nanocluster showed quenching only for the QDot 600 which has emission spectral overlap with the absorption spectra of the nanocluster (Figure 5.11 A). This might indicate some process that is related to FRET. Another interesting

phenomenon was observed in case of some nanoclusters, initially with the addition of smaller amount of the AuNCs the fluorescence of the QDots increased rather than decreasing reaching a maximum (Figure 5.10 B, and Figure 5.11 A and B). Then upon addition of more AuNCs the fluorescence gradually decreased, although AuNPs are known to increase the fluorescence of dyes either by decreasing the radiative rate or increasing the absorbance or both. This unusual concentration dependence is quite puzzling. We are currently trying to characterize this quenching process by using fluorescence lifetime measurements and the different concentration regions of the AuNCs and QDots.

5.4 References

1) Jin, R. *Nanoscale* **2010**, *2*, 343-362.
2) Jin, R.; Zhu, Y.; Qian, H. *Chem- Eur. J.* **2011**, *17*, 6584-6593.
3) Qian, H.; Zhu, Y.; Jin, R. *P. Natl. A. Sci.* **2012**, *109*, 696-700.
4) Negishi, Y.; Nobusada, K.; Tsukuda, T. *J. Am. Chem. Soc.* **2005**, *127*, 5261-5270.
5) Jadzinsky, P. D.; Calero, G.; Ackerson, C. J.; Bushnell, D. A.; Kornberg, R. D. *Science* **2007**, *318*, 430-433.
6) Zhu, M.; Lanni, E.; Garg, N.; Bier, M. E.; Jin, R. *J. Am. Chem. Soc.* **2008**, *130*, 1138-1139.
7) Zhu, M.; Qian, H.; Jin, R. *J. Am. Chem. Soc.* **2009**, *131*, 7220-7221.
8) Qian, H.; Jin, R. *Nano Lett.* **2009**, *9*, 4083-4087.
9) Qian, H.; Zhu, Y.; Jin, R. *ACS Nano* **2009**, *3*, 3795-3803.
10) Qian, H.; Zhu, Y.; Jin, R. *J. Am. Chem. Soc.* **2010**, *132*, 4583-4585.
11) Qian, H.; Jin, R. *Chem. Commun.* **2011**, *47*, 11462-11464.
12) Kumar, S.; Bolan, M. D.; Bigioni, T. P. *J. Am. Chem. Soc.* **2010**, *132*, 13141-13143.
13) DeRosa, M. C.; Crutchley, R. J. *Coordin. Chem. Rev.* **2002**, *233*, 351-371.
14) Schweitzer, C.; Schmidt, R. *Chem. Rev.* **2003**, *103*, 1685-1758.
15) Wang, S.; Gao, R.; Zhou, F.; Selke, M. *J. Mat. Chem.* **2004**, *14*, 487-493.
16) Lovell, J. F.; Liu, T.; Chen, J.; Zheng, G. *Chem. Rev.* **2010**, *110*, 2839-2857.
17) Ogilby, P. R. *Chem. Soc. Rev.* **2010**, *39*, 3181-3209.
18) Huang, Y.-Y.; Sharma, S. K.; Dai, T.; Chung, H.; Yaroslavsky, A.; Garcia-Diaz, M.; Chang, J.; Chiang, L. Y.; Hamblin, M. R. *Nanotech. Rev.* **2012**, *1*, 111-146.
19) Bakalova, R.; Ohba, H.; Zhelev, Z.; Ishikawa, M.; Baba, Y. *Nat. Biotech.* **2004**, *22*, 1360-1361.
20) Samia, A. C.; Chen, X.; Burda, C. *J. Am. Chem. Soc.* **2003**, *125*, 15736-15737.
21) Ma, J.; Chen, J.-Y.; Idowu, M.; Nyokong, T. *J. Phys. Chem. B* **2008**, *112*, 4465-4469.
22) Bakalova, R.; Ohba, H.; Zhelev, Z.; Nagase, T.; Jose, R.; Ishikawa, M.; Baba, Y. *Nano Lett.* **2004**, *4*, 1567-1573.
23) Kovalev, D.; Fujii, M. *Adv. Mater.* **2005**, *17*, 2531-2544.
24) Markovic, Z.; Trajkovic, V. *Biomaterials* **2008**, *29*, 3561-3573.
25) Vankayala, R.; Sagadevan, A.; Vijayaraghavan, P.; Kuo, C. L.; Hwang, K. C. *Angew. Chem. Int. Ed.* **2011**, *50*, 10640-10644.

26) Zhou, L.; Wei, S.; Ge, X.; Zhou, J.; Yu, B.; Shen, J. *J. Phys. Chem. B* **2012**, *116*, 12744-12749.
27) Parker, J. F.; Fields-Zinna, C. A.; Murray, R. W. *Acc. Chem. Res.* **2010**, *43*, 1289-1296.
28) Tsukuda, T. *B Chem. Soc. Jpn.* **2012**, *85*, 151-168.
29) Merkel, P. B.; Kearns, D. R. *J. Am. Chem. Soc.* **1972**, *94*, 7244-7253.
30) Regen, S. L.; Kimura, Y. *J. Am. Chem. Soc.* **1982**, *104*, 2064-2065.
31) Nilsson, R.; Merkel, P.; Kearns, D. *Photochem. Photobiol.* **1972**, *16*, 109-116.
32) Zhang, Y.; He, J.; Wang, P.-N.; Chen, J.-Y.; Lu, Z.-J.; Lu, D.-R.; Guo, J.; Wang, C.-C.; Yang, W.-L. *J. Am. Chem. Soc.* **2006**, *128*, 13396-13401.
33) Chen, F.-C.; Wu, J.-L.; Lee, C.-L.; Hong, Y.; Kuo, C.-H.; Huang, M. H. *Appl. Phys. Lett.* **2009**, *95*, 013305.
34) Gueroui, Z.; Libchaber, A. *Phys. Rev. Lett.* **2004**, *93*, 166108.
35) Nikoobakht, B.; Burda, C.; Braun, M.; Hun, M.; El-Sayed, M. A. *Photochem. Photobiol.* **2002**, *75*, 591-597.
36) Tam, F.; Goodrich, G. P.; Johnson, B. R.; Halas, N. J. *Nano Lett.* **2007**, *7*, 496-501.
37) Lakowicz, J. R. *Anal. Biochem.* **2005**, *337*, 171.
38) Malicka, J.; Gryczynski, I.; Fang, J.; Kusba, J.; Lakowicz, J. R. *Anal. Biochem.* **2003**, *315*, 160-169.
39) Chowdhury, S.; Wu, Z.; Jaquins-Gerstl, A.; Liu, S.; Dembska, A.; Armitage, B. A.; Jin, R.; Peteanu, L. A. *J. Phys. Chem. C* **2011**, *115*, 20105-20112.
40) Jennings, T.; Schlatterer, J.; Singh, M.; Greenbaum, N.; Strouse, G. *Nano Lett.* **2006**, *6*, 1318-1324.
41) Jennings, T.; Singh, M.; Strouse, G. *J. Am. Chem. Soc.* **2006**, *128*, 5462-5467.
42) Singh, M. P.; Strouse, G. F. *J. Am. Chem. Soc.* **2010**, *132*, 9383-9391.